

Jonathan Schilling

## **Experimental MHD Equilibrium Analysis of Magnetic Configurations in the Wendelstein 7-X Stellarator**

**IPP 2018-20**  
**August 2018**



# Experimental MHD Equilibrium Analysis of Magnetic Configurations in the Wendelstein 7-X Stellarator

Master-Thesis

Submitted for the Degree  
Master of Science in Physics

Kiel University  
Faculty of Mathematics and Natural Sciences - Department of Physics

Max-Planck-Institute for Plasma Physics

Submitted 18<sup>th</sup> June 2018 by Jonathan Schilling  
Born on 10<sup>th</sup> February 1992 in Hamburg, Germany



# Acknowledgements

The work presented in this thesis would not have been possible without the help of many people, of which I would like to name a few explicitly in the following.

First and foremost, I would like to thank my advisor Henning Thomsen for his constant support during the times of getting in touch with the details of Magneto-Hydrodynamics, who was always available for whatever questions and never lost his calm voice and patience over my habit of stretching deadlines up to the very last second.

Thomas Klinger is the person who brought me to W7-X, and I am especially thankful to him for giving me a warm welcome at IPP and in the city of Greifswald. The broad range of activities, ranging from car mechanics over to shared cooking activities, subtly spiced up with discussions on plasma physics and the other great questions of life, were always a great pleasure to take part in.

I would like to thank Prof. Wolf for accepting the task to be the second supervisor for this thesis and thankfully acknowledge the opportunity to discuss a brief overview of my findings for clarification and classification.

Numerous colleagues from IPP and nuclear fusion research centers all over the world took great part in making these results happen. I especially would like to thank the members of the MHD group, namely Kian Rahbarnia, Christian Brandt, Tamara Andreeva and Ulrich Neuner for their helpful critique and constant feedback. Joachim Geiger, Sam Lazerson, John Schmitt, Gavin Weir, Novimir Pablant and Yuriy Turkin provided very helpful and deeply necessary information on the theoretical and numerical aspects needed for successful equilibrium reconstructions. I would like to thank Andreas Holtz for his input on boosting the performance of the ArchiveDB access used in the pre-evaluation of the magnetic diagnostics data.

Special thanks go to Timo, Gavin and Adrian for taking me to the numerous activities outside IPP, which always provided a superb balance towards the work that always needs to be done.

I would like to thank my parents for supporting me throughout my studies, so that I was able to concentrate on the contents and did not have to worry too much about all the rest.

Last but not least, I would like to thank the “EUROfusion consortium” for the received support, i.e. for the “FuseNet“ funding of my participation fee for the IPP Summer University 2016.



1<sup>st</sup> Supervisor

Prof. Dr. Thomas Klinger  
Max-Planck-Institute for Plasma Physics  
Wendelsteinstr. 1  
17491 Greifswald

2<sup>nd</sup> Supervisor

Prof. Dr. Sebastian Wolf  
Christian-Albrechts-Universität zu Kiel  
Leibnizstraße 11-19  
24118 Kiel

Advisor

Dr. Henning Thomsen  
Max-Planck-Institute for Plasma Physics  
Wendelsteinstr. 1  
17491 Greifswald



# Declaration

I hereby certify that this thesis is entirely my own work, unless otherwise stated.

No sources or aids other than those mentioned have been used.

Parts that are in letter or spirit taken from other sources, including secondary literature, are labelled accordingly, mentioning the original source. Consequently, the author gives his permission to publish this thesis or parts of it quoting the source.

In case of doubt, please contact the author via e-mail to [jonathan.schilling@ipp.mpg.de](mailto:jonathan.schilling@ipp.mpg.de)

---

Location, Date

---

Jonathan Schilling



# Contents

<b>1. Introduction</b>	<b>3</b>
<b>2. Background</b>	<b>5</b>
2.1. Magnetic Configuration . . . . .	6
2.2. Magnetohydrodynamic Equilibrium . . . . .	10
2.3. Equilibrium Reconstruction . . . . .	16
2.4. Equilibrium Reconstruction Results . . . . .	17
<b>3. Methods</b>	<b>19</b>
3.1. Measurement Setup . . . . .	20
3.1.1. Equilibrium Magnetic Diagnostics . . . . .	20
3.1.2. Data Acquisition . . . . .	22
3.1.3. Pre-evaluation . . . . .	23
3.1.4. Access to Pre-evaluated Data: Data Sources . . . . .	26
3.2. Numerics . . . . .	26
3.2.1. The Variational Moments Equilibrium Code (VMEC) . . . . .	26
3.2.2. Magnetic Field and Vector Potential of Filamentary Wire Segments	29
3.2.3. Magnetics Response Prediction . . . . .	31
3.3. Integrated Modeling Approach . . . . .	37
3.3.1. Bayesian Data Analysis in the Minerva Framework . . . . .	37
3.3.2. Magnetic Diagnostics Calibration Experiments . . . . .	39
3.3.3. Prediction Model for VMEC and Magnetic Diagnostics . . . . .	43
<b>4. Results</b>	<b>47</b>
4.1. Numerical Verification and Validation . . . . .	48
4.1.1. Magnetic Field and Vector Potential of Filamentary Wire Segments	48
4.1.2. Magnetic Diagnostics Calibration Experiments . . . . .	50
4.1.3. Current Density from VMEC . . . . .	55
4.1.4. Response Matrix Verification . . . . .	57
4.1.5. Magnetic Diagnostics Prediction in Comparison With Other Codes .	58
4.2. Plasma Reconstructions . . . . .	61
4.2.1. Reference Experiment Program . . . . .	61
4.2.2. Scan of the Free Parameters . . . . .	62
4.2.3. Maximum Posterior Inversion . . . . .	63
4.2.4. Results of Reconstruction . . . . .	65
<b>5. Discussion</b>	<b>69</b>
5.1. Datasource for Magnetic Diagnostics . . . . .	70
5.2. VMEC . . . . .	70
5.3. Magnetic Field and Vector Potential of Filamentary Wire Segments . . . . .	71
5.4. Magnetic Diagnostics Response Prediction . . . . .	72
5.5. The Minerva Framework . . . . .	73
5.6. Magnetic Diagnostics Calibration Experiments . . . . .	74
5.7. Reconstruction Results . . . . .	74
<b>6. Summary</b>	<b>77</b>

<b>References</b>	<b>79</b>
<b>A. Numerical Details</b>	<b>83</b>
<b>B. Explanation of Graph Nodes</b>	<b>87</b>





## 1. Introduction

Wendelstein 7-X (W7-X) is a large superconducting stellarator device, used to study high-temperature plasmas to reach for the goal of using nuclear fusion as an energy resource. There exist several difficulties associated with creation of reactor-relevant high-temperature plasmas, which are characterized by high density, high temperature and long confinement times for fast particles. First, thermal insulation towards the confining structure has to be excellent in order to reach the required temperatures on the order of 10 keV ( $\approx 100$  million  $^{\circ}\text{C}$ ). Second, contact between the plasma and the containment wall must be strictly prohibited. This is required due to the low heat capacity of the plasma, leading to immediate cooldown once wall contact is established. The approach used in the field of magnetically confined nuclear fusion research to address these two requirements, is to use a strong magnetic field to guide the hot plasma particles, which are bound to a gyro motion around the magnetic field lines by the Lorentz force. To generate the confinement magnetic field, superconducting coils have been installed at W7-X. This paves the way to demonstrate steady-state operation capabilities of the device, an important aspect in view of the requirements for a future nuclear fusion power plant. A cut-open view of W7-X is depicted in Fig. 1.

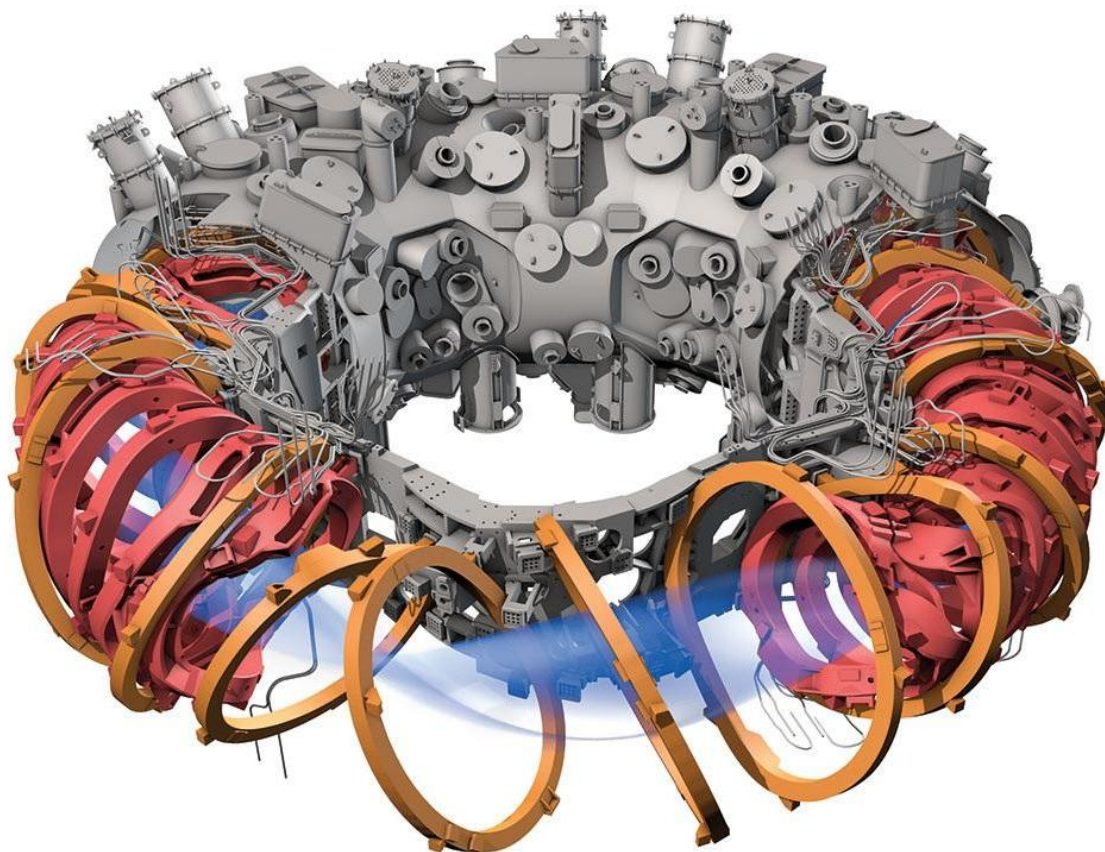


Fig. 1: Wendelstein 7-X: Coil system, portholes, central support ring, vacuum (plasma) vessel, last closed flux surface and part of the cryostat. Figure reproduced from [1].

The magnetized plasma inside the device features its own collective behaviour, leading to its own electrical currents  $\mathbf{j}$ , which in turn modify the confinement magnetic field<sup>1</sup>  $\mathbf{B}$ . These currents are necessary to sustain the force balance between the pressure gradient  $\nabla p$  due to high density and temperature in the plasma core region and the Lorentz force  $\mathbf{j} \times \mathbf{B}$ , leading to the magnetohydrodynamic (MHD) force balance equation:

$$\nabla p = \mathbf{j} \times \mathbf{B} \quad .$$

This simple-looking equation is surprisingly hard to solve for the given geometry, because both  $\mathbf{j}$  and  $\mathbf{B}$  are fully three-dimensional vector-valued quantities and the solution has to match the complicated confinement magnetic field geometry self-consistently. Dedicated numerical tools to solve the MHD force balance have been developed over the last decades and were tested thoroughly. In fact, the magnetic field geometry of W7-X is the result from a dedicated optimization procedure aimed at obtaining the best confinement magnetic field compatible with a set of seven selected optimization criteria [2, 3]:

1. high quality of vacuum magnetic flux surfaces
2. good finite- $\langle\beta\rangle$  equilibrium properties
3. good MHD stability properties
4. small neoclassical transport in the  $1/\nu$  regime
5. small bootstrap current in the long-mean-free-path regime
6. good collisionless  $\alpha$ -particle confinement
7. good modular coil feasibility

This thesis addresses the second optimization criterion, namely the MHD equilibrium properties of plasmas in W7-X. A combination of aforementioned first-principle equilibrium codes and experimental observations from the second operational phase OP1.2a of W7-X is used to reconstruct a plasma equilibrium compatible with the measurements.

- In the first section, I will introduce the physical foundations used to describe magnetohydrodynamic equilibria in toroidal magnetic confinement devices.
- The next section focuses on the measurement setup used to obtain information on the magnetic field and current density structure in W7-X plasmas and introduces modeling assumptions and numerical tools used to analyze the obtained experimental data.
- This is followed by a section on the results obtained during this work, where the employed modeling tools were checked for accuracy and self-consistency of the predictions and exemplary equilibrium reconstructions for a reference experiment in W7-X are presented.
- These results are discussed in the next chapter.
- A summary of the work closes this thesis.

---

<sup>1</sup>Usually, the magnetic field is denoted by  $\mathbf{H}$  and the magnetic flux density  $\mathbf{B}$  is then given by  $\mathbf{B} = \mu_0 \mu_r \mathbf{H}$ , where  $\mu_0$  is the vacuum magnetic permeability and  $\mu_r$  is the relative permeability, taking material properties into account. In the field of plasma physics, these two terms are frequently used synonymously due to the vanishing magnetic susceptibility  $|\chi| \ll 1$  of the plasma, leading to  $\mu_r = 1 + \chi \approx 1$ . Then, magnetic field and magnetic flux density only differ by the scaling factor  $\mu_0 = 4\pi \cdot 10^{-7} \text{ V s A}^{-1} \text{ m}^{-1}$ .

## 2. Background

In this section, the physical principles and conventions will be introduced, which are relevant for the later parts of this work.

The toroidal coordinate system as used throughout this work is shown in Fig. 2. A torus is characterized by the *major radius*  $R_0$  and the *minor radius*  $a$ . The *main axis* is co-aligned with the  $z$  axis and the *minor axis* follows the path of a circle with radius  $R_0$  in the  $(R, \varphi)$  plane. The *toroidal* direction  $\varphi$  goes the “long way” around the torus, i.e. for constant  $R$  and  $Z$ , the toroidal angle  $\varphi$  varies from 0 to  $2\pi$ . The *poloidal* direction  $\theta$  goes the “short way” around the torus, i.e. for constant  $\rho$  and  $\varphi$ , the poloidal angle  $\theta$  varies from 0 to  $2\pi$ . The *radial* direction  $\rho$  references the  $\varphi = \text{const.}$  cross section, if not otherwise stated, and denotes the distance from the minor axis of the torus to a given location.

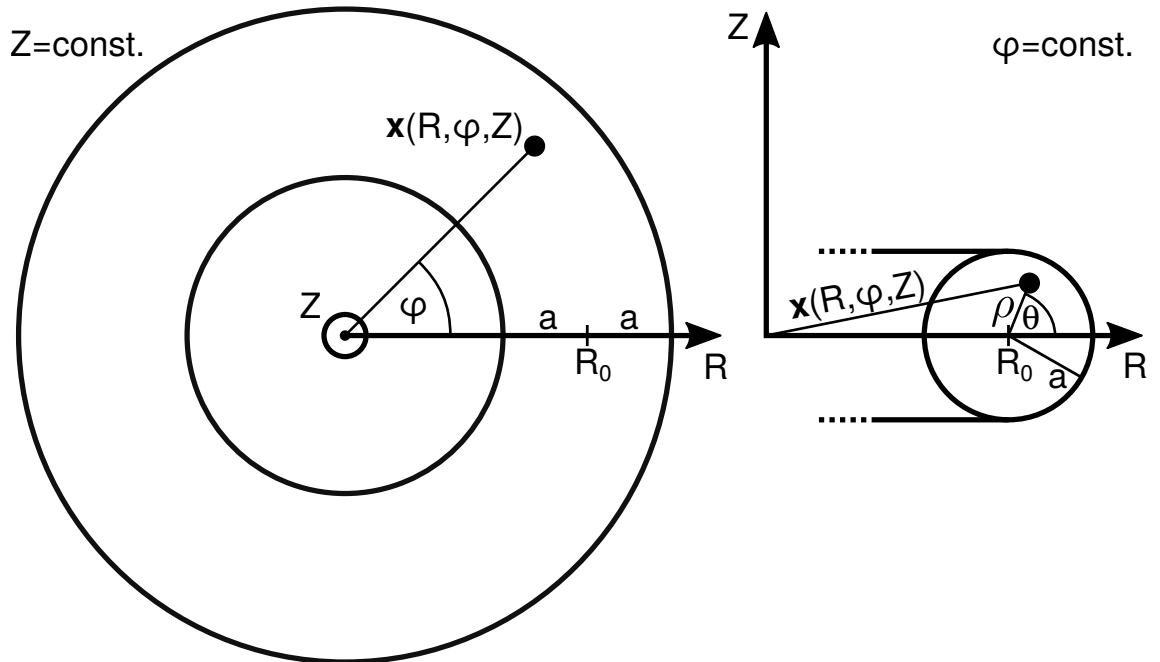


Fig. 2: Toroidal geometry in a cylindrical coordinate system. A position vector  $\mathbf{x}(R, \varphi, Z)$  is either identified by cylindrical coordinates  $(R, \varphi, Z)$  or by toroidal coordinates  $(\rho, \varphi, \theta)$  for a given major radius  $R_0$ . The minor radius  $a$  is the radius of the cross section in the  $\varphi = \text{const.}$  plane.

## 2.1. Magnetic Configuration

Charged particles in a magnetized plasma are bound to the magnetic field lines in a gyro motion [4]. They can drift along the magnetic field lines. This behaviour is described by the term *guiding center drift*. The geometrical details of a magnetic field are called a *magnetic configuration*. In a toroidal magnetic configuration, where the magnetic field lines are bent into the shape of a torus and thus can close on themselves, particles are confined. If the toroidal magnetic field is generated by external coils, the coil windings are closer to each other on the inboard side than on the outboard side of the torus. This leads to a gradient in the magnetic field strength, where the magnetic field is stronger on the inboard side than on the outboard side (cf. Fig. 6). In the microscopic picture, a  $\nabla|\mathbf{B}|$  drift (where  $\mathbf{B}$  denotes the magnetic flux density) leads to a vertical separation of the negatively charged electrons and the positively charged ions. This vertical charge separation leads to formation of a vertical electric field, which in turn gives rise to a net outward directed drift for both positively and negatively charged species due to an  $\mathbf{E} \times \mathbf{B}$  drift (where  $\mathbf{E}$  denotes the electric field due to the vertically separated charges).

This net outward-directed flow of particles can be counteracted by twisting the magnetic field lines, leading to particle orbits, which connect regions of lower magnetic field strength to regions of higher magnetic field strength and thus lead to an equalization of the particle drifts. A twist of the magnetic field lines is accomplished by adding a poloidal magnetic field component. This can be generated in two ways. Either, a net toroidal current is induced in the plasma by means of a transformer (such a device being called a *Tokamak*) or the external coil system is specifically designed to introduce a well-tailored poloidal magnetic field component, which is known as a *stellarator*.

For a particle in the plasma, the ratio of poloidal circumferences to toroidal circumferences averaged over many orbits around the machine is denoted by the symbol  $\iota$  and called the *rotational transform*<sup>2</sup>. For irrational values of  $\iota$ , a magnetic field line ergodically covers a toroidally shaped surface, which is called a *flux surface* [5]. Flux surfaces form a set of nested tori, where the innermost (singular) flux surface is a line called the *magnetic axis*. The rotational transform varies in the radial direction, where the local rate of change in  $\iota$  with the radial coordinate  $\rho$  is called *magnetic shear* and is denoted by  $\theta_V$  [6]:

$$\theta_V = \frac{\rho^2 d\iota/d\rho}{2\pi R_0} . \quad (1)$$

As the  $\iota$  profile passes through low-order rational values, magnetic field lines close on themselves after a few poloidal and toroidal orbits. This leads to self-amplification of small perturbations in the field line geometry and *magnetic islands* open up [7]. A magnetic island can have its own magnetic axis and sufficiently large islands even have their own confinement properties [8]. The geometry of the magnetic field lines in the regions in between magnetic islands and “good” flux surfaces is generally chaotic. A pressure gradient along the magnetic field lines vanishes in the equilibrium state and pressure can only build up perpendicular to the flux surfaces. Radial particle transport is enhanced in the magnetic island regions, as particles can travel along the circumference of an island very fast. In the context of magnetically confined nuclear fusion, these radial transport channels are an unwanted feature in the plasma core region, since they degrade plasma confinement. However, magnetic islands at the plasma edge can be tailored to provide a defined geometry for particle exhaust from the plasma edge region to an *island divertor* [9].

<sup>2</sup>Other symbols for the rotational transform include  $\iota/(2\pi)$  and  $\epsilon$  [5].

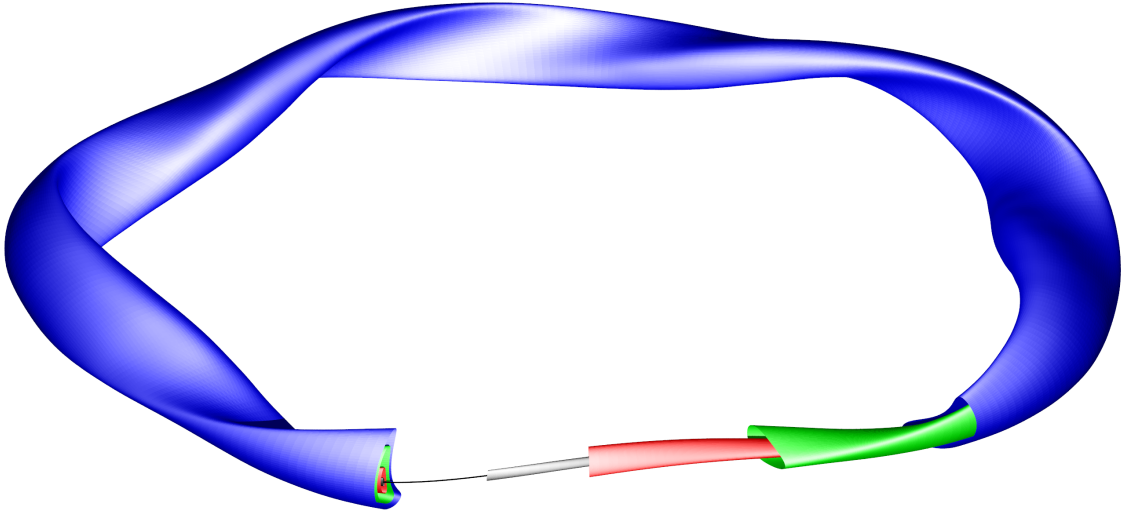


Fig. 3: Nested flux surfaces of the high-mirror magnetic configuration KJM001 of W7-X are shown in grey, red, green and blue. The black line indicates the magnetic axis.

The *last closed flux surface* (LCFS) is the last (in the radial direction) flux surface, on which the magnetic field lines are closed and do not end on the plasma vessel wall. Thus, it defines the confined plasma volume.

In W7-X, the main coil system creating the confinement magnetic field consists of 70 coils, of which 50 are non-planar coils and 20 are planar coils (see Fig. 5). Only the non-planar coils carry current in the standard magnetic configuration of W7-X, which was designed to use an island divertor for plasma exhaust. It therefore relies on a specific value of  $\iota \approx 5/5$  at the LCFS for correct divertor operation.

In total there exist seven different types of coils, i.e. five non-planar and two planar coil types. An arrangement of these seven coils constitutes a *half-module* of the coil system of W7-X. By placing two half-modules back to back in the toroidal direction, a *module* is assembled. Thus, a total of fourteen coils makes a module and five modules form the complete magnet system of W7-X. Each coil of the same type is wired in series with the other coils of the same type and this allows to energize the whole coil system by seven power supplies. By knowledge of the seven coil currents, the complete magnetic configuration is determined, given the geometry of the magnet system is known precisely.

The coil system of W7-X features a five-fold symmetry in the toroidal direction, i.e. the magnetic field consists of five *field periods* and this is denoted by the number of field periods  $n_{\text{fp}} = 5$ . A net plasma current, e.g. the bootstrap current (see below), could lead to a shift of the rotational transform profile. This would lead to a shift in the position of the magnetic islands at the plasma edge, possibly damaging the divertor elements by imposing heat fluxes to areas, which were not considered to handle these in the design. Thus, for enhanced experimental flexibility, the planar coils have been added to permit a correctional shift of the rotational transform profile. Example flux surfaces from Wendelstein 7-X are depicted in Fig. 3.

Vacuum flux surface measurements can be used in a stellarator to map out the flux surfaces of the magnetic field using an electron beam and a fluorescent rod, which is swept through the plasma vessel cross section. The electron beam is injected along the magnetic field lines, with the electrons following a gyro motion around the magnetic field

lines, and eventually hits the fluorescent rod, generating a visible light spot. Since the rod is observed by a camera, long-time exposure and image processing permits to map out complete vacuum flux surfaces and thus determine the magnetic field structure to high precision [10].

Especially errors in the magnetic field show up nicely in these flux surface measurements, e.g. by formation of additional internal vacuum magnetic islands. To cope with  $(n, m) = (1, 2)$  field errors (where  $n$  and  $m$  denote the toroidal and poloidal mode numbers<sup>3</sup>), *trim coils* have been added to the magnet design of W7-X. These coils are large copper windings, which are attached to the outer vessel of W7-X and generate magnetic fields radially inward directed towards the major torus axis. Five trim coils are distributed among the five modules of the machine, and since each trim coil is powered by its own power supply, it is possible to generate magnetic fields which are not toroidally symmetric, i.e. balance out non-toroidally symmetric error fields.

A frequent visualisation strategy for flux surfaces is to plot Pointcaré maps of the magnetic field lines, i.e. cross sections through the nested flux surfaces. An example of this for the flux surface geometry shown in Fig. 3 is shown in Fig. 4.

---

<sup>3</sup>In toroidal magnetic confinement devices, the magnetic field geometry is periodic in toroidal and poloidal directions. A two-dimensional Fourier decomposition in the poloidal and toroidal angles is often times used to characterize symmetry properties of a given quantity, e.g. error field terms.

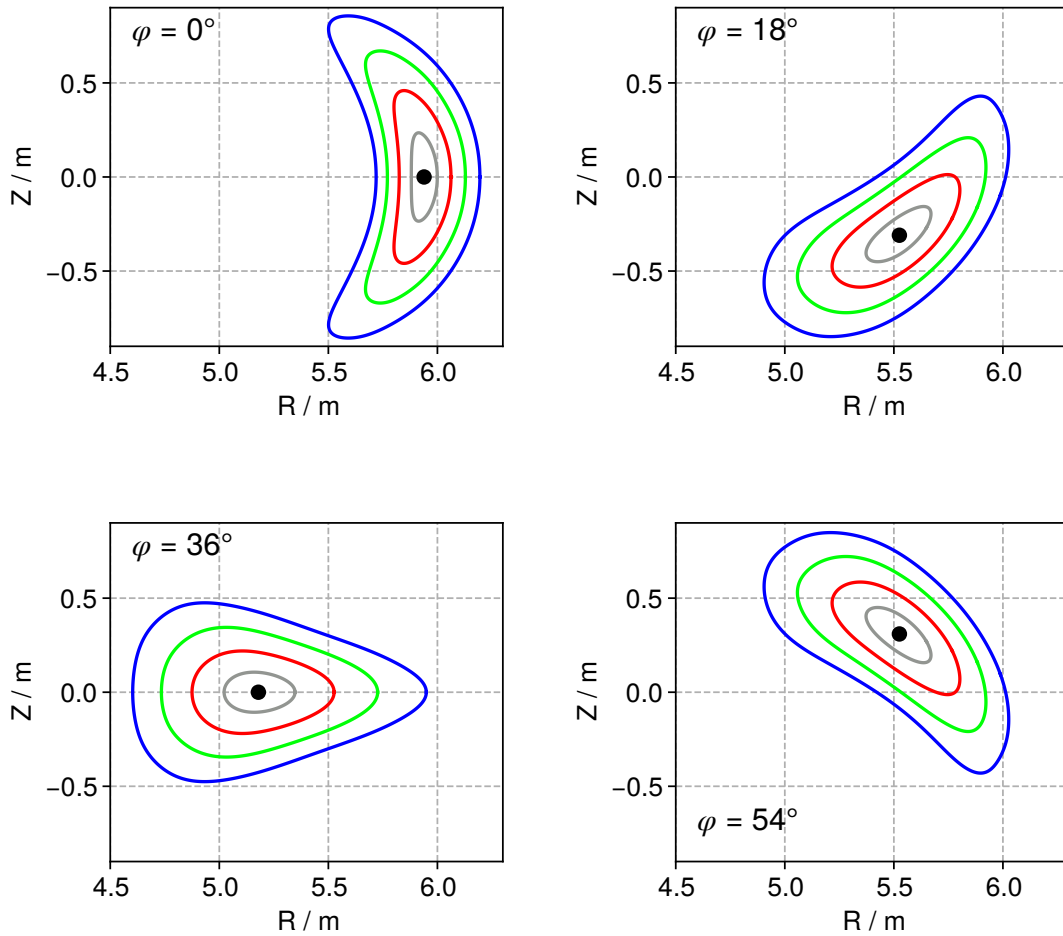


Fig. 4: Flux surfaces in W7-X for four position within one half-module. From top left to bottom right, the toroidal positions are  $(0, 1/4, 1/2, 3/4) \cdot 72^\circ$ . The top left cross section plane is called the *bean-shaped* plane and the bottom left one is called *triangular-shaped* plane. This is a two-dimensional view of the flux surfaces shown in Fig. 3. The black dot in the center corresponds to the magnetic axis.

## 2.2. Magnetohydrodynamic Equilibrium

In the two-fluid picture of a plasma, electrons and ions are each described by a density  $n_e$  and  $n_i$ , respectively and a temperature  $T_e$  and  $T_i$ , respectively with subscripts e for electrons and i for ions. By the ideal gas law, pressures  $p_e$  and  $p_i$ , respectively can be related to that state of electrons and ions:

$$p_e = n_e k_B T_e \quad (2)$$

$$p_i = n_i k_B T_i \quad (3)$$

with the Boltzmann constant  $k_B$ . Generally, electrons and ions are not in thermal equilibrium, i.e.  $T_e \neq T_i$ . The current density  $\mathbf{j}$  of electrons and ions is given from their charge flux:

$$\mathbf{j}_e = q_e n_e \mathbf{u}_e \quad (4)$$

$$\mathbf{j}_i = q_i n_i \mathbf{u}_i \quad (5)$$

with the charges  $q_e$  and  $q_i$  of electrons and ions, respectively and their flow velocities  $\mathbf{u}_e$  and  $\mathbf{u}_i$ , respectively. The magnetohydrodynamic one-fluid picture merges the electrons and ions into a combined plasma fluid with total pressure  $p = p_e + p_i$  and a total current density  $\mathbf{j} = \mathbf{j}_e + \mathbf{j}_i$ .

In the plasma, the inward-directed pressure gradient  $\nabla p$ , that forms due to the rising temperature and density in the core of the plasma, is balanced on each flux surface by the Lorentz force  $\mathbf{j} \times \mathbf{B}$ . This is the MHD *force balance equation*:

$$\nabla p = \mathbf{j} \times \mathbf{B} \quad (6)$$

The approach in this master thesis employs the ideal MHD plasma model, which is characterized by vanishing plasma resistivity and results in the assumption of nested flux surfaces throughout the whole plasma volume.

It follows from Eq. (6) that a pressure gradient  $\nabla p$  must be perpendicular to the magnetic field by taking the dot product with the magnetic flux density  $\mathbf{B}$ :

$$\mathbf{B} \cdot \nabla p = \mathbf{B} \cdot (\mathbf{j} \times \mathbf{B}) \quad (7)$$

$$\Leftrightarrow \mathbf{B} \cdot \nabla p = 0 \quad , \quad (8)$$

since  $\mathbf{j} \times \mathbf{B} \perp \mathbf{B}$ . The current density  $\mathbf{j}$  is split into components parallel ( $\parallel$ ) and perpendicular ( $\perp$ ) to the local magnetic flux density vector:

$$\mathbf{j} = \mathbf{j}_{\parallel} + \mathbf{j}_{\perp} \quad (9)$$

Inserting this into the force balance equation (6) yields a constraint on the current density  $\mathbf{j}$ :

$$\begin{aligned} \nabla p &= \mathbf{j} \times \mathbf{B} \\ &= (\mathbf{j}_{\parallel} + \mathbf{j}_{\perp}) \times \mathbf{B} \\ &= \mathbf{j}_{\parallel} \times \mathbf{B} + \mathbf{j}_{\perp} \times \mathbf{B} \\ \nabla p &= \mathbf{j}_{\perp} \times \mathbf{B} \quad , \end{aligned} \quad (10)$$

since  $\mathbf{j}_{\parallel} \times \mathbf{B} = 0$ . In particular, one can see that the force balance between the kinetic pressure force and the Lorentz force is fulfilled only by a current density directed perpendicular to the magnetic field. Since this results in a diamagnetic behaviour of the plasma,

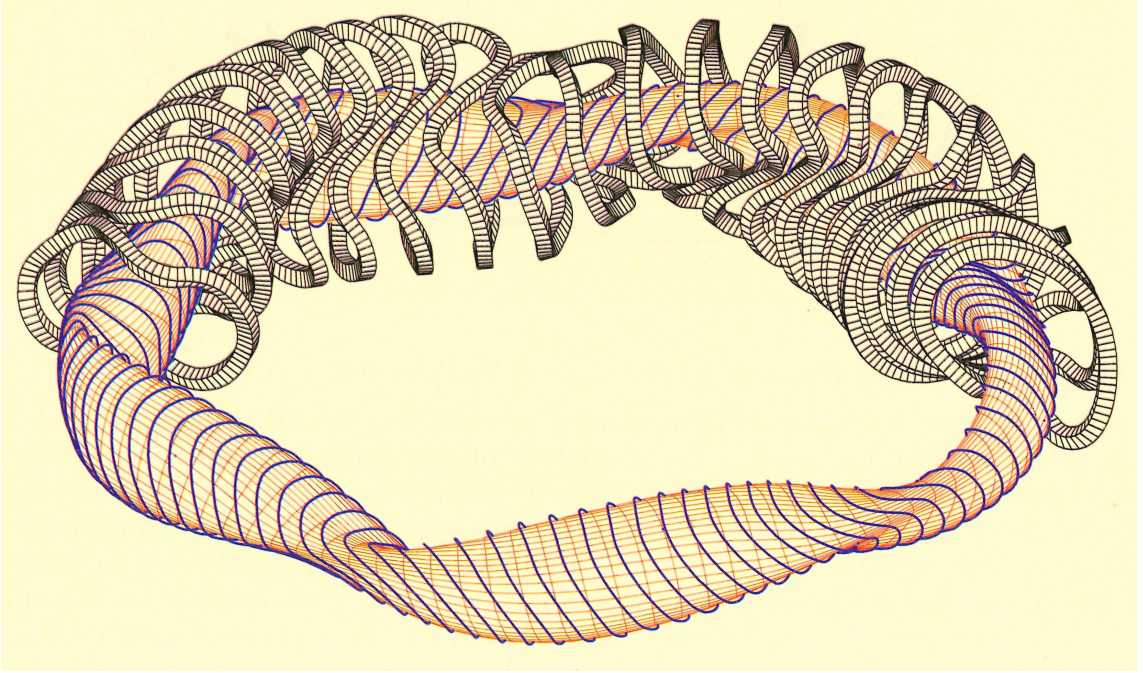


Fig. 5: Part of the optimized coil geometry of Wendelstein 7-X and the last closed flux surface (LCFS). Light orange lines on the LCFS mark a uniform grid on quasi-magnetic coordinates and thick blue lines mark current density field lines. Figure reproduced from [11].

i.e. increasing the pressure leads to a rise of the current which counteracts  $\mathbf{B}$ ,  $\mathbf{j}_\perp$  is also called *diamagnetic current density*. Fig. 5 gives an overview over the current density field lines on the LCFS in W7-X.

The diamagnetic behavior is illustrated in Fig. 6 for a volume-averaged normalized plasma pressure  $\langle\beta\rangle \approx 5\%$  with

$$\langle\beta\rangle = \left\langle \frac{p}{B^2/(2\mu_0)} \right\rangle . \quad (11)$$

The diamagnetic behaviour of the plasma with finite pressure leads to a lowered magnetic field strength in the core plasma region. Since the total charge in the plasma is conserved, the current density  $\mathbf{j}$  must be divergence free:

$$\begin{aligned} \nabla \cdot \mathbf{j} &= 0 \\ \Leftrightarrow \nabla \cdot \mathbf{j}_\parallel + \nabla \cdot \mathbf{j}_\perp &= 0 \\ \Leftrightarrow \nabla \cdot \mathbf{j}_\perp &= -\nabla \cdot \mathbf{j}_\parallel . \end{aligned} \quad (12)$$

The current density vector is tangential to the flux surfaces, since:

$$\nabla p \cdot \mathbf{j} = (\mathbf{j} \times \mathbf{B}) \cdot \mathbf{j} = 0 . \quad (13)$$

Neglecting external sources for a net toroidal current, there are two main contributions to the toroidal current in a stellarator. The first part is the so-called Pfirsch-Schlüter (PS) current [12], which arises to close the current paths of the diamagnetic current density according to Eq. (12). An exemplary cross-section plot of the Pfirsch-Schlüter current

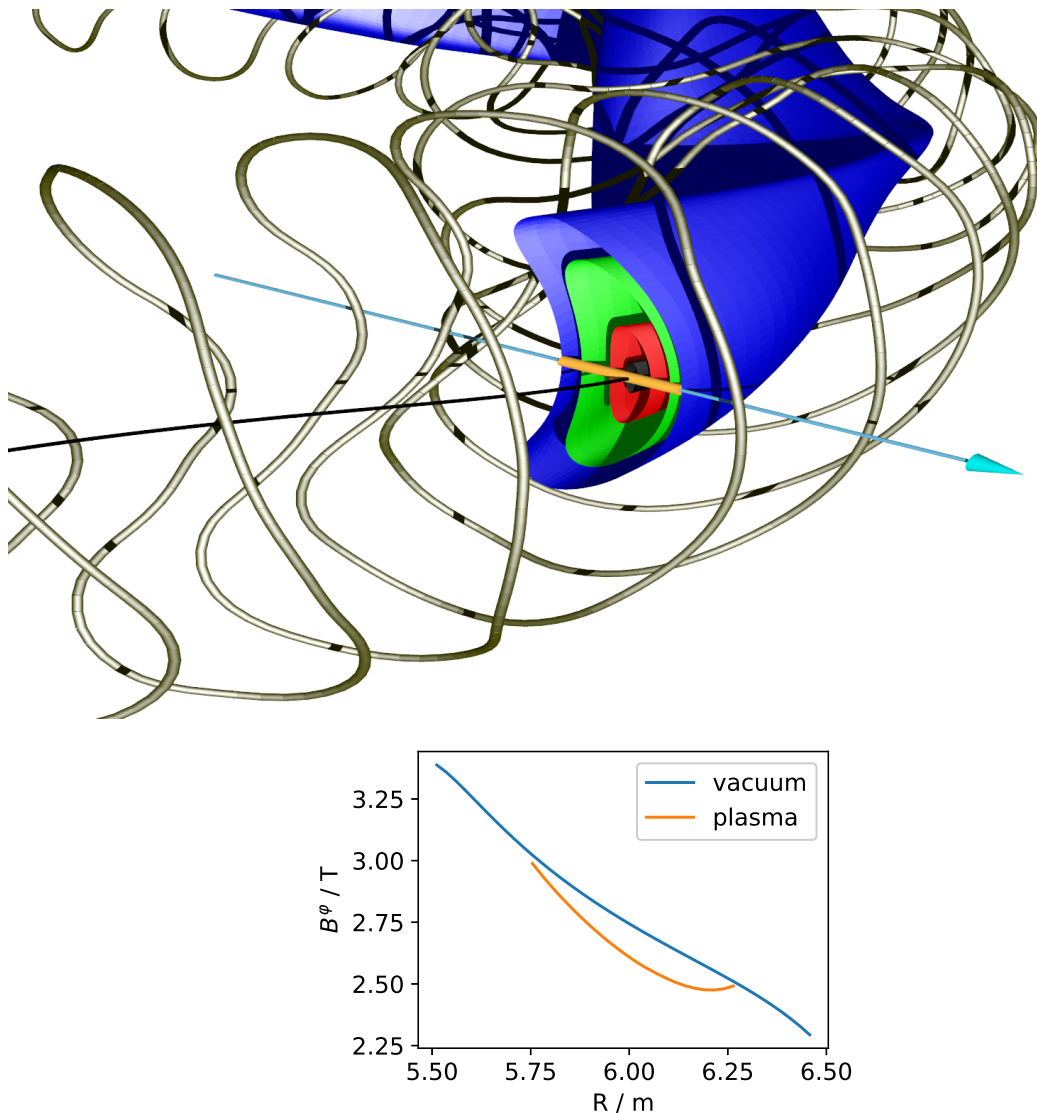


Fig. 6: In the upper half of the figure, guiding lines of the non-planar magnetic field coils and flux surfaces of the standard magnetic configuration EIM of W7-X are shown. The light blue arrow indicates a path along which the magnetic field in toroidal direction  $B^\varphi$  was sampled for both the vacuum case (i.e. no plasma present, light blue) and the case with plasma (shown in orange). The black line in the center of the plasma represents the magnetic axis.

density for a W7-X equilibrium with  $\langle\beta\rangle \approx 5\%$  is shown in Fig. 7. The second part is the *bootstrap current* resulting from *neoclassical transport*. Generally, confinement of particles in toroidal magnetic fields is limited by radially outward directed particle transport, e.g. by collisions. In the picture of classical transport, it is assumed that the toroidal geometry can be approximated by a cylindrical plasma column. Coulomb collisions between charged particles in the plasma lead to a radial displacement on the order of the Larmor radius  $r_L$ :

$$r_L = \frac{mv_\perp}{|q|B} \quad (14)$$

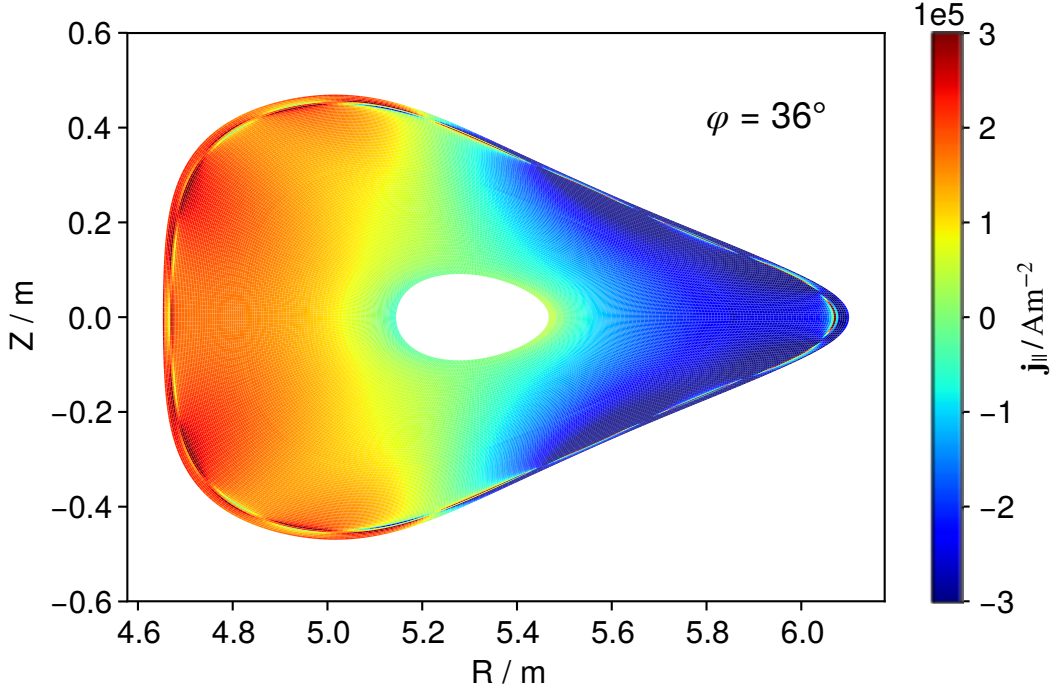


Fig. 7: Parallel current density from a net current free VMEC (see Sec. 3.2.1) calculation for the W7-X high-mirror magnetic configuration KJM001 and  $\langle\beta\rangle \approx 5\%$ . The dipole-shaped Pfirsch-Schlüter current pattern is clearly visible. Numerical artifacts close to the LCFS originate from the radial derivatives of the covariant magnetic field components used to compute the current density (see Sec. 3.2.1) and are not physical.

with the particle mass  $m$ , its velocity component  $v_{\perp}$  perpendicular to the magnetic field lines, its charge  $q$  and the local magnetic flux density  $B$ . The resulting predictions for the confinement time of a charged particle in the plasma are underestimating measured values by several orders of magnitude.

This gap between experiment and prediction is narrowed by the picture of neoclassical transport, which takes the toroidal geometry into account. The first adiabatic invariant is the magnetic moment  $\mu$  of a particle, as it performs the gyro motion around a magnetic field line:

$$\mu = \frac{mv_{\perp}^2}{|q|B} \quad . \quad (15)$$

Let a velocity  $\mathbf{v} = v_{\parallel}\hat{\mathbf{e}}_{\parallel} + v_{\perp}\hat{\mathbf{e}}_{\perp}$  with unit vectors  $\hat{\mathbf{e}}_{\parallel}$  and  $\hat{\mathbf{e}}_{\perp}$  parallel and perpendicular to the local magnetic flux density vector, respectively, be given for a certain particle on the outboard side of the torus, traveling along the magnetic field lines. As the particle approaches the inboard torus side due to the rotational transform, its magnetic moment is conserved and parallel velocity is decreasing for an increase of the perpendicular velocity component, leading to faster gyration. If the initial particle speed at the outboard side was high enough, the particle can overcome the higher magnetic field region on the inboard side of the torus and it is called a *passing* particle.

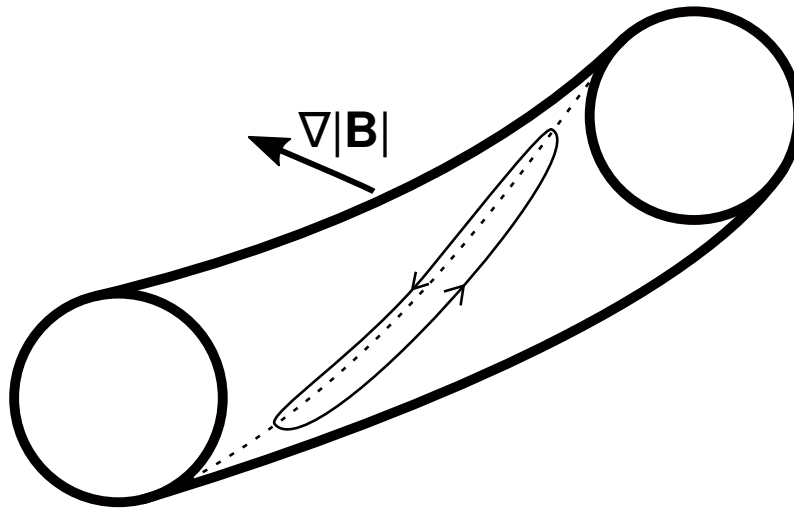


Fig. 8: Three-dimensional sketch of a banana orbit on a toroidal section of a torus. The inward-directed arrow indicates the direction of the magnetic flux density gradient. The dashed line symbolizes a twisted magnetic field line. A banana orbit of a trapped particle is sketched out as a thin solid line with arrows representing the local direction of movement.

Otherwise, the particle is reflected at the location on its trajectory, where the parallel velocity is used up for the gain in gyro frequency to conserve its magnetic moment. After traveling back on the outboard side of the torus, it again approaches the inboard side, where it is reflected again and so forth. Hence, such a particle is called to be *trapped*. As the projection of the resulting trajectory into a  $\varphi = \text{const.}$  plane resembles the shape of a banana, these trapped particle orbits are given the name *banana orbits*. A sketched banana orbit is shown in Fig. 8. The projection of banana orbits into a  $\varphi = \text{const.}$  plane is shown in Fig. 9. In the left panel, a single banana orbit (1) as projected into the  $\varphi = \text{const.}$  plane is shown along with the orbit of a corresponding passing particle. Note that upward and downward movement occur at different radii, separated by the *banana width*  $w_B$ . A second banana orbit (2) of a particle on a flux surface closer to the magnetic axis is added in the right panel. At the location denoted by P, particles on banana orbits (1) are moving downwards and particles on banana orbits (2) are moving upwards. As the plasma density is generally higher towards the center, more particles perform banana orbits there. This is indicated by the slightly thicker line of banana orbit (2). The banana orbits typically have a large toroidal extent, as can be seen in Fig. 8. This results in the net toroidal *bootstrap current* at location P, because the particle flow contributions from banana orbits closer to the magnetic axis than P are not completely balanced by particles on banana orbits outside of P.

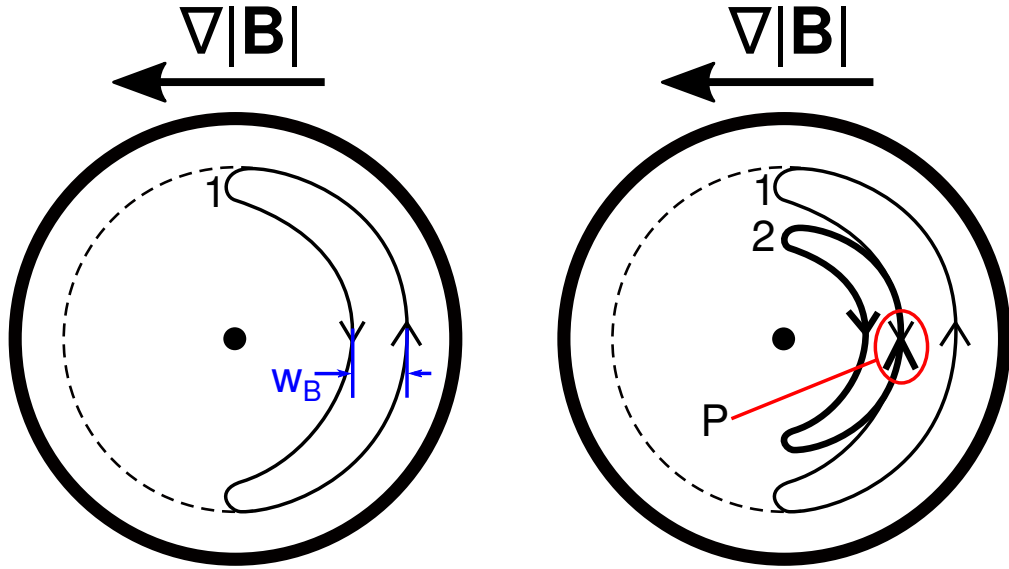


Fig. 9: Banana orbits in a  $\varphi = \text{const.}$  plane. The arrows on top indicate the direction of the magnetic flux density gradient towards the major axis of the torus. The thick circle is the plasma boundary. Banana orbits are depicted by thin solid lines 1 and 2 with banana width  $w_B$ . The dashed lines resemble the shape of a passing particle originating from the same flux surface as the particle on banana orbit 1. The dot in the center of the cross section indicates the location of the magnetic axis. Point P illustrates the origin of the bootstrap current from an imbalance of banana orbit densities for different radii.

An effect present in high- $\langle\beta\rangle$  plasmas is called the *Shafranov shift* [7]. The vertical magnetic field due to large Pfirsch-Schlüter currents acts on the flux surfaces and “pushes” them outwards. For theoretical predictions, this can be visualized by comparing Pointcare plots of the flux surface geometry for equilibrium calculations at both low and high values for  $\beta$  [13]. Assuming constancy of pressure and temperature on flux surfaces, tomographic reconstructions from line-integrated X-ray measurements can be used to experimentally infer the flux surface shape and thus measure the Shafranov shift [7].

As outlined in Ref. [14], magnetic coordinates in which the magnetic field lines are represented as straight lines can be found by numerical field-line following and simultaneous recording of quantities to express the coordinates in, e.g. the  $R$  and  $Z$  coordinates of the current position on the magnetic field line and the magnetic field strength  $|\mathbf{B}|$ . Further information on this can be found in the literature [14, 15].

The coordinates are then represented by two-dimensional Fourier series in the poloidal and toroidal angles  $\theta$  and  $\varphi$  as follows:

$$R(s, \theta, \varphi) = \text{Re} \left( \sum_{m,n} R_{m,n}(s) e^{i(m\theta - nn_{\text{fp}}\varphi)} \right) \quad (16)$$

$$Z(s, \theta, \varphi) = \text{Re} \left( \sum_{m,n} Z_{m,n}(s) e^{i(m\theta - nn_{\text{fp}}\varphi)} \right) \quad (17)$$

with the poloidal mode numbers  $m$ , the toroidal mode numbers  $n$  and complex-valued Fourier amplitudes  $R_{m,n}$  and  $Z_{m,n}$ .

This formulation using complex numbers is usually split into real and imaginary parts:

$$R(s, \theta, \varphi) = \sum_{m,n} \left( R_{mn}^{\cos}(s) \cos(m\theta - nn_{\text{fp}}\varphi) + R_{mn}^{\sin}(s) \sin(m\theta - nn_{\text{fp}}\varphi) \right) \quad (18)$$

$$Z(s, \theta, \varphi) = \sum_{m,n} \left( Z_{mn}^{\cos}(s) \cos(m\theta - nn_{\text{fp}}\varphi) + Z_{mn}^{\sin}(s) \sin(m\theta - nn_{\text{fp}}\varphi) \right). \quad (19)$$

The summation  $m, n$  is described in the following. Since the cosine function features even symmetry, i.e.  $\cos(x) = \cos(-x)$ , the Fourier amplitudes for  $m = 0$  and  $n < 0$  have to be identical to the Fourier amplitudes for  $m = 0$  and  $n > 0$  for equal  $|n|$ . The sine function features odd symmetry, i.e.  $\sin(x) = -\sin(-x)$ , and therefore the Fourier amplitudes for  $m = 0$  and  $n < 0$  have to be identical to  $(-1)$  times the Fourier amplitudes for  $m = 0$  and  $n > 0$  for equal  $|n|$ . Thus, the Fourier amplitudes for  $m = 0$  and  $n < 0$  do not need to be specified and the corresponding combinations of  $m$  and  $n$  are left out of the summation. Upper limits on the mode number summations set the accuracy that can be reached by using the finite Fourier series representation and need to be chosen as necessary for a given geometry. For an example of the resulting mode number combinations, see Appendix A.

### 2.3. Equilibrium Reconstruction

In the field of equilibrium reconstruction, the task is to compute a MHD equilibrium, which matches the experimental plasma conditions as close as possible. This is assessed by computing predictions for the measured signals of the diagnostics included in the reconstruction process and comparing those with the actual measurement values.

The confinement magnetic field is determined by the main field coil geometry and the electrical currents through these coils. Free parameters used to modify the equilibrium calculation include, but are not limited to, the toroidal magnetic flux  $\Phi_{\text{edge}}$  enclosed within the LCFS, the radial profile of enclosed current or rotational transform and the radial profile of pressure or mass density. Given these input parameters, a MHD equilibrium can be computed. The predictions for the measured signals are calculated considering the geometry of a diagnostic. Measured raw data might need to be transformed into a format directly comparable to physical quantities from the prediction. This is the *forward problem* [16].

The *reverse problem* is defined by the task to find a set of parameter values which produces well matching predictions for the measured signals within the allowed parameter space. This optimization problem needs a measure to judge the “matching quality” of the predictions to the measured signals, which could be a  $\chi^2$  sum for a least-squares minimization routine [17] or the posterior probability distribution in a Bayesian approach [18].

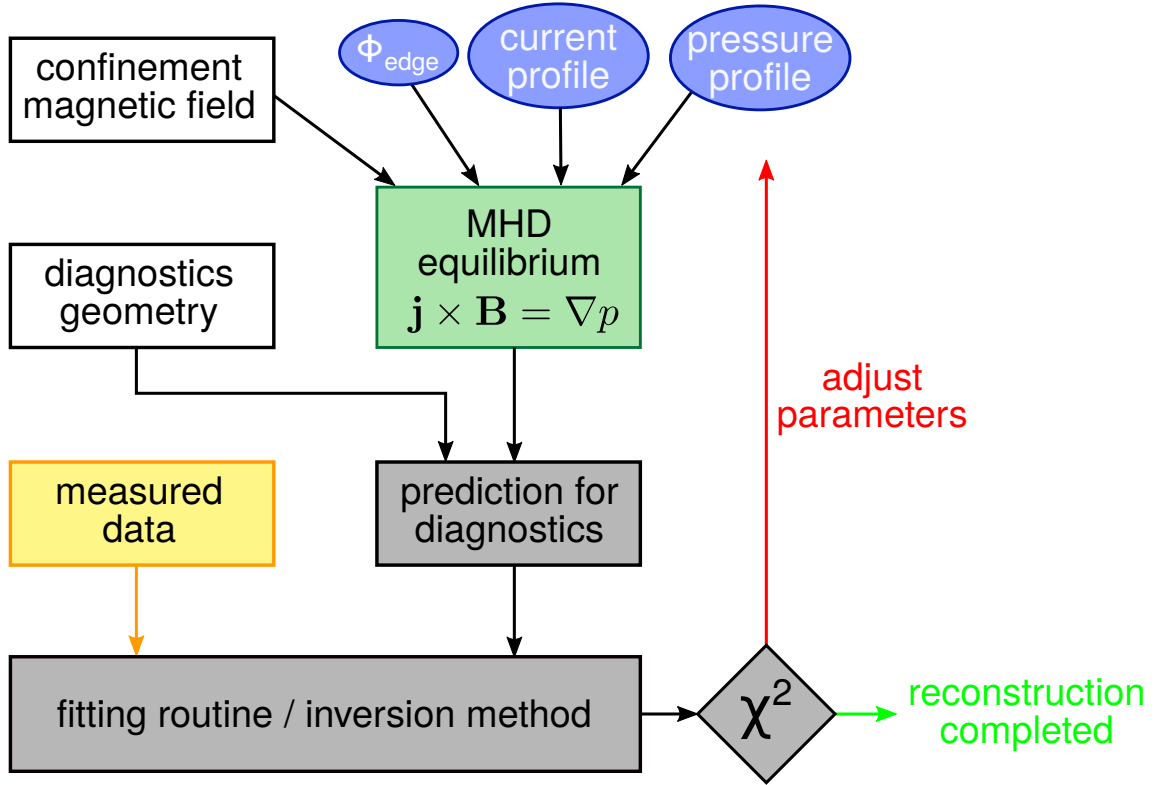


Fig. 10: Flowchart of a MHD equilibrium reconstruction procedure. Free parameters are shown in light blue, the MHD equilibrium solver in green, measured data in yellow, constants in boxes with white background and computational steps in grey. Based on the results from the inversion method, the free parameters are modified (red path) or the reconstruction is considered to be completed (light green path).

## 2.4. Equilibrium Reconstruction Results

Equilibrium reconstruction results are valuable for many further analysis steps that build upon the equilibrium calculation result. The reconstructed equilibrium itself also can be useful to infer parameters, like the current density distribution inside the plasma throughout the machine, which are not directly accessible by diagnostics.

The mapping of the geometry of one diagnostic, e.g. a Hydrogen pellet injection trajectory for plasma core fuelling [7], can be projected into the plane of view of a different diagnostic, e.g. the Thomson scattering diagnostic [19] line-of-sight to study the radial transport of the injected Hydrogen pellet [20].

This particular geometry is shown in Fig. 11 for W7-X. Transport calculations to predict the flow of particles in the plasma depend on the details of the employed equilibrium calculation, since particle transport trajectories are located on the flux surfaces. The equilibrium is analyzed with respect to MHD instabilities in the field of MHD stability analysis [21]. Naturally, the instability predictions vary as well with the equilibrium and thus, predictive power is enhanced strongly by analysing equilibria which resemble the experimental plasma conditions as close as possible.

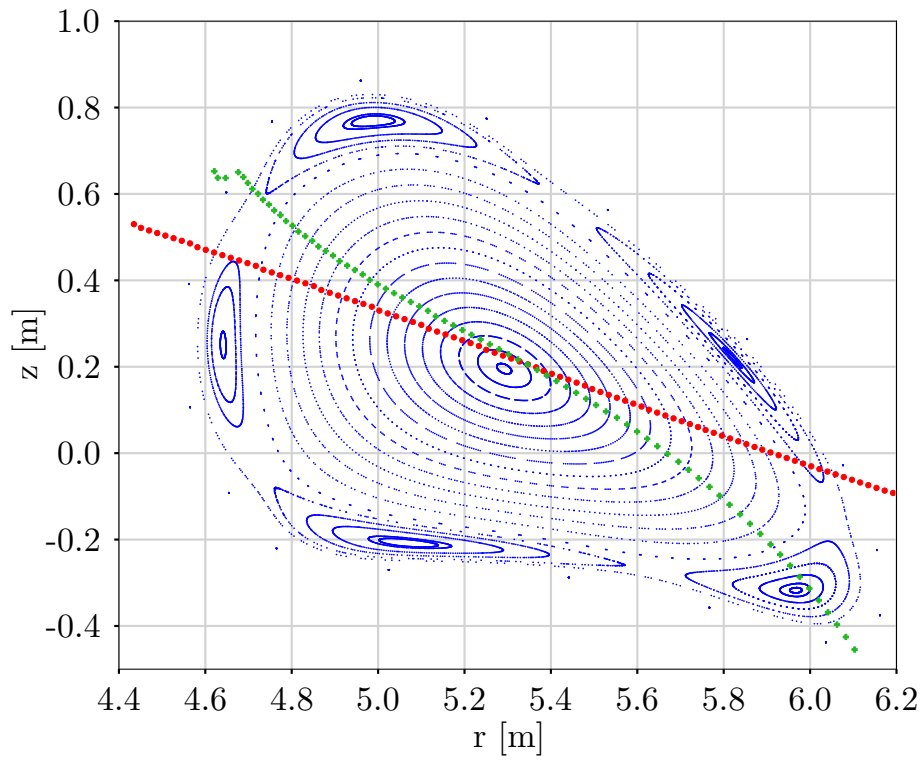


Fig. 11: Pointcaré plot of the flux surface geometry of the standard magnetic configuration EIM (blue) in the toroidal plane of the Thomson scattering diagnostic at  $\varphi = 171^\circ$  (line of sight in red). The trajectory of an injected hydrogen pellet as mapped to the toroidal plane of the Thomson scattering system is shown in green. Figure reproduced from [20].

### 3. Methods

In this chapter, the measurement setup of the magnetic diagnostics used for this work is presented. The numerical implementation of the models introduced so far are examined in detail, since the speed of modeling and accuracy of the results are heavily dependant on the details of the implementation. The employed normalized coordinates are introduced. Computation of the contravariant current density components  $j^i$  as well as transformation to cylindrical components is laid out. An accurate description of the magnetic flux density  $\mathbf{B}$  and the magnetic vector potential  $\mathbf{A}$  for filamentary wire segments was implemented and is presented here. The section closes with a description of the integrated modeling approach employed for matching experimental data with theoretical predictions.

### 3.1. Measurement Setup

Here, the magnetic diagnostics installed at W7-X are introduced. Grouped by their measurement principle, they can be distinguished into fluxloops and Rogowski coils. Fluxloops measure magnetic flux through their spatial cross section. By applying simple modeling assumptions, an estimate for the stored energy in the plasma can be obtained from a special type of fluxloop, called a diamagnetic loop, which encircles the cross section of the plasma. Rogowski coils measure the plasma current. An overview over the magnetic diagnostics installed at W7-X is shown in Fig. 12.

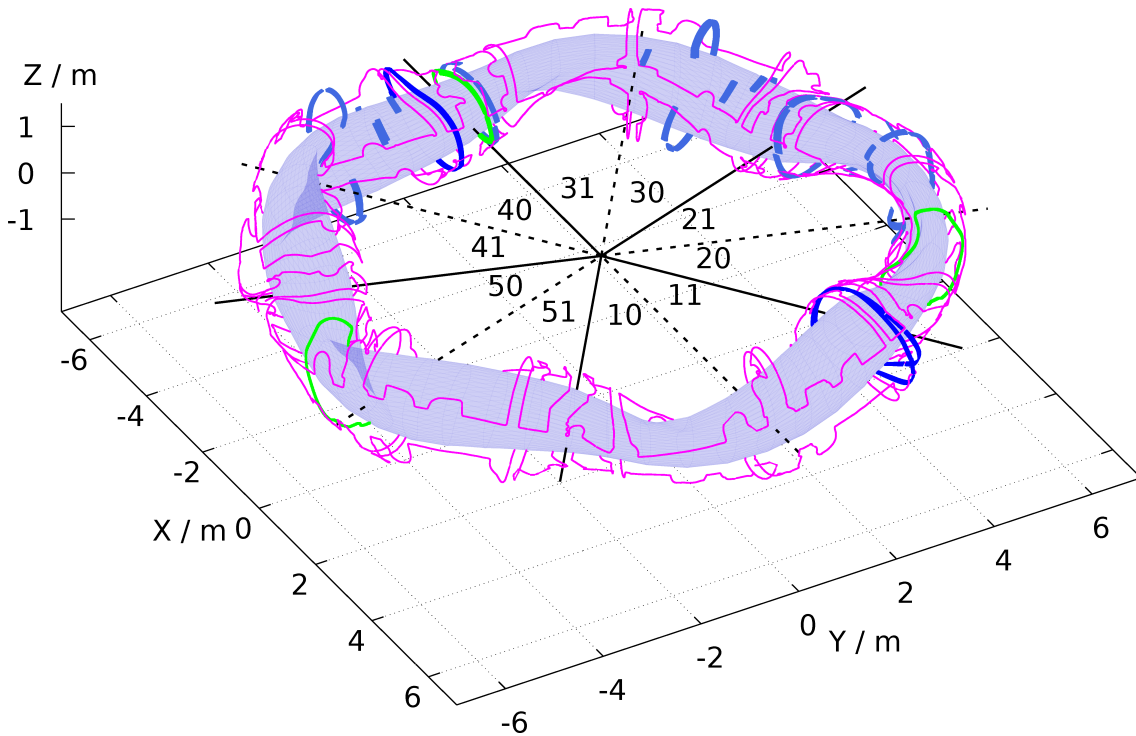


Fig. 12: The equilibrium magnetic diagnostics of W7-X consist of diamagnetic loops and compensation loops (green), closed Rogowski coils (dark blue), segmented Rogowski coils (light blue) and saddle coils (pink). The LCFS of the standard magnetic configuration EIM is shown to guide the eye. Dark solid lines indicate the module boundaries and dashed black lines the boundaries between two half-modules within a module. The numbers in the center correspond to the module names in the format of (module half-module).

#### 3.1.1. Equilibrium Magnetic Diagnostics

Diamagnetic loops are used to measure the toroidal magnetic flux change due to a rise of the plasma pressure. They encircle the plasma poloidally and thus also measure changes in the vacuum magnetic field. In order to subtract this field component from the measured signal, *compensation loops* between the plasma cross section and the magnetic field coils are added to the setup. They do not encircle the plasma, but approximately measure the same variation of the vacuum magnetic field to allow accounting for eddy currents in the plasma vessel. This could introduce additional magnetic flux not originating from the

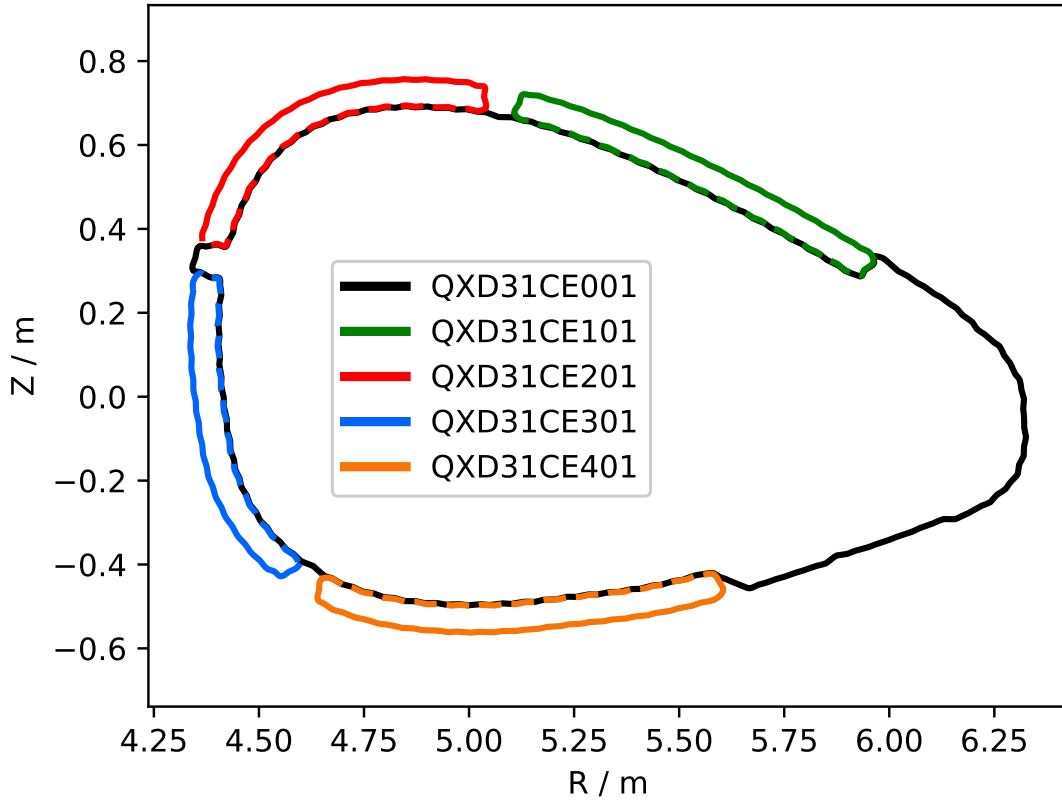


Fig. 13: Geometry of the diamagnetic loop in black and the four compensation loops in colors as projected into a single  $\varphi = 178^\circ$  plane. The labels denote the coil identifiers.

diamagnetic behavior of the plasma and thereby degrade the stored energy estimation (see below). The sum of their flux signals are subtracted from the signal of the diamagnetic loop either by wiring them in series with appropriate polarity or by digitizing their signals separately and performing the subtraction in software. The geometry of a diamagnetic loop and its compensation loops located in half-module 31 of W7-X is shown in Fig. 13. The loops are slightly tilted, so that the normal vector of their cross section is parallel to the magnetic axis at the center of the loop in toroidal location.

Saddle coils are designed to measure the magnetic flux changes due to Pfirsch-Schlüter (PS) currents. Since PS currents have opposite directions inboard and outboard in the poloidal cross section of the plasma (see Fig. 7), they generate a vertical magnetic field which penetrates through the cross section of the saddle coils.

Rogowski coils are used to measure toroidal plasma currents. They can encircle the whole plasma cross section along its poloidal circumference and then measure the net toroidal current or can be split up into segments along the poloidal path. These are called *segmented Rogowski coils* and allow to derive information about the current density distribution in the poloidal cross section. The engineering details of the magnetic diagnostics installed at Wendelstein 7-X can be found in the literature [22].

The diamagnetic energy  $W_{\text{dia}}$  of a plasma can be estimated from the flux measured by a diamagnetic loop. The magnetic flux change  $\Delta\Phi$  due to the plasma is then in the cylindrical Tokamak approximation given by:

$$\Delta\Phi = -\frac{\mu_0 W_{\text{dia}}}{3\pi B^\varphi R_0} + \frac{(\mu_0 I_{\text{tor}})^2}{8\pi B^\varphi} + \frac{\pi\mu_0 \iota_{\text{vac}}}{R_0} \int_0^a j^\varphi r^3 dr \quad , \quad (20)$$

where the first term accounts for plasma diamagnetism, i.e. the magnetic flux is lowered by the plasma and the two other terms are accounting for plasma *paramagnetism* [23].  $B^\varphi$  is the toroidal magnetic flux density on the magnetic axis,  $R_0$  is the radius of the magnetic axis,  $\mu_0$  is the vacuum permeability,  $I_{\text{tor}}$  is the net toroidal current,  $\iota_{\text{vac}}$  is the rotational transform of the vacuum magnetic field and  $j^\varphi$  is the toroidal current density component.

### 3.1.2. Data Acquisition

The data acquisition system for the equilibrium magnetic diagnostics at W7-X faced the engineering obstacle to allow experiment program lengths of up to 30 min [24]. Long pulse lengths on the order of 1000s demand for a design of the diagnostics that can withstand stray radiation from the heating systems (in particular stray microwave radiation from the electron cyclotron heating system in W7-X). Thermal radiation and strong X-ray emission are also challenging to handle in the design of the diagnostics [22]. Thermoelements form at the connectors, if different materials are used for the connector parts and the parts are at different temperatures, e.g. due to anisotropies in the stray radiation of the plasma or partial shielding by the wall tiles.

Thermal drifts also play a role in the measurement electronics, which are needed to precondition the induced voltages from the pickup coils for conversion to digital signals. Here, offset voltages are omnipresent in the involved amplifier and digitizer circuits. These offset levels show a variation with temperature. The data acquisition systems slowly heat up during operation due to ohmic and switching losses in the components. This leads to slow drifts in the offset voltages of the involved amplifiers, which can hardly be predicted to sufficient precision. Therefore, the chopped digitizer concept presented in Ref. [24] was chosen for installation at W7-X. The input signal is repeatedly reversed in polarity by electronic switches, thereby reversing the polarity of the signal of interest with a rate given by the *chopper frequency*. The offset voltages, which add to the input signal behind the chopper stage, do not reverse polarity and can be averaged out. An overview scheme of the digitizing electronics is shown in Fig. 14. Thermovoltages in the diagnostics coil setup and cabling up to the chopper stage still contribute to error voltages, which cannot be mitigated by the chopper amplifier. Temperature sensors installed inside some of the pickup coils can be used to sense the local temperature of the diagnostic coil and model thermovoltages, resistance shifts of the pickup coil due to the temperature dependence of the specific resistance of the wire and issue an experiment shutdown to prevent overtemperatures in the sensors, which otherwise might damage the diagnostic coils.

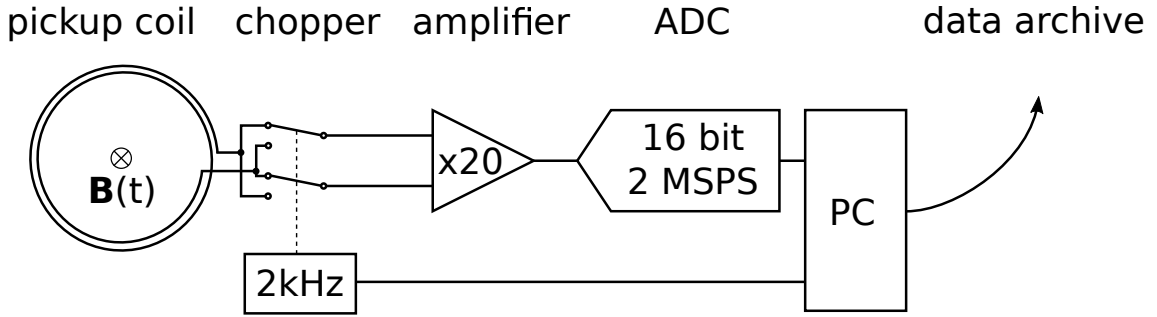


Fig. 14: Chopped data acquisition setup for the equilibrium magnetic diagnostics at W7-X. From left to right, a pickup coil, chopping switches, preamplifier, analog-digital-converter (ADC) and personal computer (PC) are shown. The chopping switches are operated at a rate of 2 kHz and the ADC has 16 bits of resolution at a sampling rate of 2 million samples per second (MSPS). Acquired raw data (ADC conversion results) are stored in the central data archive of W7-X.

### 3.1.3. Pre-evaluation

The physical quantity measured by a magnetic diagnostic coil of interest for equilibrium reconstruction purposes is the magnetic flux through the cross section of the coil. The data acquisition systems for the equilibrium magnetic diagnostics only saves the raw conversion results of the ADC as 16 bit integer values into the central data archive of W7-X [25]. Hence, for any data analysis of the magnetic diagnostics, the same operations have to be conducted on the raw data in order to obtain the magnetic flux values. It was decided to separate this pre-evaluation step from the analysis methods that build on top of the magnetic flux measurements and conduct these automatically for each experiment program and all available magnetic diagnostics of W7-X.

A sketch of the pre-evaluation steps necessary to obtain the magnetic flux timetraces is shown in Fig. 15. Small voltage spikes are introduced into the signal of the pickup coil at the polarity reversals due to an effect known as *charge injection* in the field-effect transistors [26] inside the selected electronic switches for the chopper part of the digitizer, as shown in Fig. 15a. These spikes are eliminated from the raw signal by replacing the last three samples before the switchover with the value before them and the first three samples after the switchover with the first sample after them. The sampling rate of the ADC is fixed at 2 MHz, resulting in a sampling interval of 500 ns. Six samples in total are modified by the named spike removal procedure, corresponding to a total time interval of 3  $\mu$ s. The high-frequency response of the magnetic diagnostics drops off in the kilohertz range, corresponding to timescales on the order of a millisecond. Variations on a faster timescale than the response time of the diagnostic are most likely due to noise pickup and therefore, the simple despiking procedure is not expected to introduce a significant error. If further analysis shows a requirement for more accurate interpolation, the algorithm developed in Ref. [27] can be applied. The overall eo offset of the preamplifier is removed by computing the mean value of the whole acquired timetrace and subtracting it from the signal. This results in the signal shape as shown in Fig. 15b.

The chopping of the input signal is reversed by flipping the polarity of the acquired signal in the intervals where the chopping switches connected the input signal in reverse polarity to the preamplifier. This is illustrated in Fig. 15c.

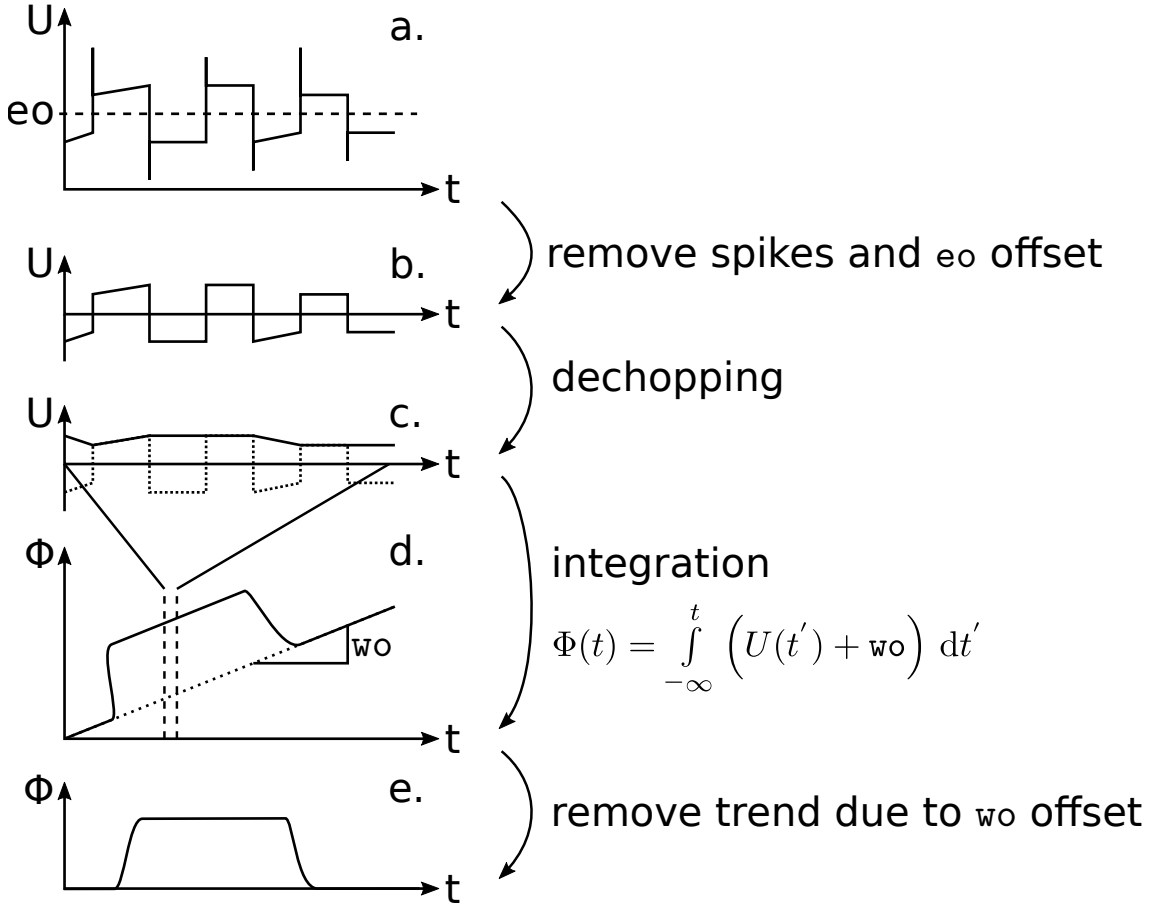


Fig. 15: Steps a-e of the pre-evaluation are conducted for each experiment program and each magnetic diagnostic at W7-X. Subfigures a-c show an extract of the time axis of d and e. Induced voltages as measured by the ADC are indicated by a vertical scale  $U$  and magnetic flux is indicated by  $\Phi$ .

The magnetic flux signal is computed by summing up the flux contributions from each timestamp. The discrete integration can be formulated as follows:

$$\Phi(t_i) = \sum_{j=0}^i U(t_j) \cdot \Delta t \quad (21)$$

for an evaluation timestamp  $t_i$  with  $i > 0$ , acquired voltages  $U(t_j)$  and a sampling time interval  $\Delta t$  (500 ns for a sampling rate of 2 MHz). The start of the acquisition period is  $t_0$  and if  $N$  samples were acquired,  $0 \leq i < N$ . If  $\Delta t$  is constant, it can be factored out of the summation:

$$\Phi(t_i) = \Delta t \cdot \sum_{j=0}^i U(t_j) \quad (22)$$

The resulting timetrace of the magnetic flux over one experiment program is sketched out in Fig. 15d.

Thermovoltages and contributions from other error voltage sources in front of the chopper switches are still contributing to the pickup coil voltage signal. Given that these error voltages remain constant over one experiment program, they result in a linear trend in

the background of the accumulated magnetic flux. This is mitigated by starting the data acquisition systems significantly earlier than the plasma startup in an experiment program, typically 5 s, and continuing data acquisition some more time after the end of plasma heating (resulting in a decay of the plasma), also typically 5 s. The error voltages are assumed to be present without any plasma as well, so the trend is still present in the phases before and after the plasma phase of the experiment program. Then, the trend can be removed by assuming a linear increase of the background signal throughout the whole experiment program and subtracting it from the flux signal. The offset of this trend is zero, since the induced voltage is accumulated with zero offset. The slope of the trend (`wo_slope`) is computed from the last magnetic flux sample  $\Phi(t_{N-1})$  and the length of the acquisition period of the magnetic diagnostics for the particular experiment program ( $t_{N-1} - t_0 = N\Delta t$ ):

$$\text{wo\_slope} = \frac{\Phi(t_{N-1})}{N\Delta t} \quad . \quad (23)$$

The resulting signal is sketched out in Fig. 15e. This is the signal that is subsequently uploaded to the central data archive of W7-X [25] and provided for further analysis by the whole W7-X scientific team.

The magnetic fluxes measured by the pickup coils are useful for equilibrium reconstructions, because they are the most direct quantity that can be modeled based on an equilibrium calculation, but are not a very comprehensive quantity to evaluate during an experiment day for estimating e.g. plasma performance. Therefore, two simple models are applied to the pre-evaluated magnetic fluxes as presented in the following.

The first one gives the net toroidal current in the plasma from the magnetic flux measured by a closed Rogowski coil. This is a linear relationship, which is characterized by a scaling factor. The scaling factor between the net plasma current and the magnetic flux signal of the Rogowski coil is obtained from a Biot-Savart calculation, where the plasma is modeled by a single elementary wire on the magnetic axis of the standard magnetic configuration of W7-X, which is energized by a unit current of 1 A. The prediction for the induced signal in the Rogowski coil is computed as a line integral over the magnetic flux density due to the unit current along the magnetic axis and is called  $\Phi_{1A}$  here. Then, the net toroidal current in Ampères in the plasma  $I(t)$  for a given measured Rogowski coil magnetic flux  $\Phi(t)$  is given by:

$$I(t) = \Phi(t)/\Phi_{1A} \quad . \quad (24)$$

The second one gives the stored energy in the plasma from measured magnetic fluxes of a diamagnetic loop and its four compensation coils. Here, a simplified version of the approximation in Eq. (20) is used to obtain the energy content of the plasma  $W_{\text{dia}}$  from the compensated diamagnetic flux signal:

$$W_{\text{dia}}(t) \approx -\frac{3\pi R_0 B^\varphi}{\mu_0} \left( \Phi_{\text{dia}}(t) - C \cdot \sum_i \Phi_{\text{comp},i}(t) \right) \quad (25)$$

with the radius of the magnetic axis  $R_0$  at the toroidal position  $\varphi = 178^\circ$  of the diamagnetic loop, the toroidal magnetic field strength  $B^\varphi$  on the magnetic axis, the vacuum permeability  $\mu_0$  and the magnetic flux of the diamagnetic loop  $\Phi_{\text{dia}}$  as well as the four magnetic fluxes measured by the compensation coils  $\Phi_{\text{comp},i}$  with  $i \in \{1, \dots, 4\}$ . The compensation factor  $C$ , which adjusts the sensitivities of the compensation loops to external magnetic field perturbations to the sensitivity of the diamagnetic loop, is determined from measurements during the main field coil current ramps [28].

### 3.1.4. Access to Pre-evaluated Data: Data Sources

A concept heavily applied in the Minerva framework [29], which is used throughout this work, are *data sources* for accessing experimentally obtained data from different diagnostics.

In most cases, raw data as acquired by the acquisition devices (ADCs, cameras, ...) within a diagnostic has to be preprocessed in order to be interpreted in a physics context. The details of this pre-evaluation for the magnetic diagnostics at W7-X are outlined in the previous section. The details of the necessary steps to obtain physically meaningful signals differ from diagnostic to diagnostic, and from machine to machine, as different systems are used. Even within one diagnostic at a single machine, upgrades over time may require the analysis routines to be adapted to changes in sensitivity factors, calibration values, alignments, and many more aspects. The analysis routines building on top of the acquired data might also change over time.

In this context, the idea of a data source is to introduce a standardized layer in between the diagnostic signal pre-evaluation routines and the data analysis tools using the measured data. This layer corresponds to the time-dependant magnetic fluxes as measured by the pickup coils in the case of the magnetic diagnostics. The key advantage of this approach is that the whole process of obtaining physically meaningful quantities, which might be different among diagnostics, machines and time, is contained inside the data source. Analysis code, e.g. prediction models and inversion routines, then can be modified internally as long as the exterior interface stays the same. For example, the MHD equilibrium solver could be upgraded to one taking less physical assumptions into account to allow expanded degrees of freedom in the computation. This allows application of the same physical models in a modeling-based analysis approach to different experiments, as long as a data source is available for each of the experiments in question. Similarly, introducing a new experiment or diagnostic into an already existing modeling toolchain is reduced to the development of a data source that complies with the agreed interfacing standard.

Debugging is also simplified in this approach, since test cases can be created for data sources as well as for the physical models and debugged separately.

## 3.2. Numerics

In this section, the numerical implementation of the methods necessary for performing equilibrium reconstructions is presented. First, the MHD equilibrium solver used for the purpose of this thesis, the Variational Moments Equilibrium Code (VMEC), is presented. Methods to compute the magnetic flux density and magnetic vector potential by filamentary wire segments are shown and a test against an analytical model for later verification the accuracy of the computation is described. These methods are combined in the last part of this section, which focuses on computation of predictions for the magnetic diagnostics given an equilibrium calculation from the VMEC code.

### 3.2.1. The Variational Moments Equilibrium Code (VMEC)

The Variational Moments Equilibrium Code [30] is used to solve the force balance equation (6) for a given magnetic field, pressure or mass density profile and toroidal current or rotational transform profile. It assumes the existence of nested flux surfaces inside the plasma volume and ignores internal magnetic islands. On rational flux surfaces, where the rotational transform profile  $\iota$  is close to a rational number  $n/m$ , this can lead to diverging

surface currents on the flux surfaces, which would keep the islands closed in a perfectly conducting plasma.

VMEC uses an inverse coordinate representation for the flux surface geometry, that is, for the  $R$  and  $Z$  components of locations on flux surfaces. Moreover, since VMEC is a spectral MHD equilibrium code, both the flux surface geometry and the magnetic field are represented as two-dimensional Fourier series. The covariant magnetic field representation  $B_i$  in the output file is used to derive the contravariant current density components  $j^i$ . In VMEC, the force balance equation is solved on a discrete set of radial locations, i.e. flux surfaces. The number of flux surfaces to take into account is specified in the input parameters of the code and determines the radial resolution of a VMEC calculation.

For toroidal geometry, the three coordinates that uniquely identify any location within the LCFS are  $(\Phi_{\text{tor}}, \theta, \varphi)$ .  $\Phi_{\text{tor}}$  is the enclosed toroidal magnetic flux of the flux surface running through the specified position.  $\theta$  is a poloidal angle-like coordinate (that is, it is running from 0 to  $2\pi$  around the poloidal circumference of the torus) and approximately measures the arc length along the circumference of the flux surface cross section.  $\varphi$  is the toroidal angle as in a cylindrical coordinate system. These coordinates are normalized to  $(s, u, v)$  within the VMEC code.

$s$  is the radial coordinate, called the flux surface label, with  $s = \Phi_{\text{tor}}/\Phi_{\text{edge}}$ , where  $\Phi_{\text{edge}}$  is the total enclosed toroidal magnetic flux enclosed by the LCFS. This implies  $0 \leq s \leq 1$ , where  $s = 0$  indicates the magnetic axis and  $s = 1$  indicates the LCFS.

The poloidal coordinate  $\theta$  is normalized to  $0 \leq u \leq 1$  and the toroidal coordinate  $\varphi$  is normalized to  $0 \leq v \leq 1$  as well. The VMEC coordinates  $(s, u, v)$  are not *magnetic coordinates* [31], i.e. the magnetic field lines are not straight when represented in this set of coordinates. To obtain magnetic coordinates, a local modification parameter  $\lambda$  has to be taken into account for the poloidal angle [30]. Table 1 shows an overview of the normalized coordinates. The normalized coordinates for a chosen toroidal cutplane are

physical quantity	physical range	normalization factor	normalized name	normalized range
$\Phi_{\text{tor}}$	$0 \leq \Phi_{\text{tor}} \leq \Phi_{\text{edge}}$	$\Phi_{\text{edge}}$	s	$0 \leq s \leq 1$
$\theta$	$0 \leq \theta \leq 2\pi$	$2\pi$	u	$0 \leq u \leq 1$
$\varphi$	$0 \leq \varphi \leq 2\pi$	$2\pi$	v	$0 \leq v \leq 1$

Tab. 1: Normalized coordinates used in VMEC and their physics counterparts.

illustrated in Fig. 16. The magnetic flux density  $\mathbf{B}$  is saved in the output file in a covariant representation:

$$\mathbf{B} = B_s \nabla s + B_u \nabla u + B_v \nabla v. \quad (26)$$

The covariant magnetic flux density components  $B_i$  for a location  $(s, u, v)$  are given as two-dimensional Fourier series:

$$B_s = \sum_{m,n} B_{s,mn}^{\text{cos}}(s) \cos(2\pi(mu - nn_{\text{fp}}v)) + B_{s,mn}^{\text{sin}}(s) \sin(2\pi(mu - nn_{\text{fp}}v)) \quad (27)$$

$$B_u = \sum_{m,n} B_{u,mn}^{\text{cos}}(s) \cos(2\pi(mu - nn_{\text{fp}}v)) + B_{u,mn}^{\text{sin}}(s) \sin(2\pi(mu - nn_{\text{fp}}v)) \quad (28)$$

$$B_v = \sum_{m,n} B_{v,mn}^{\text{cos}}(s) \cos(2\pi(mu - nn_{\text{fp}}v)) + B_{v,mn}^{\text{sin}}(s) \sin(2\pi(mu - nn_{\text{fp}}v)) \quad (29)$$

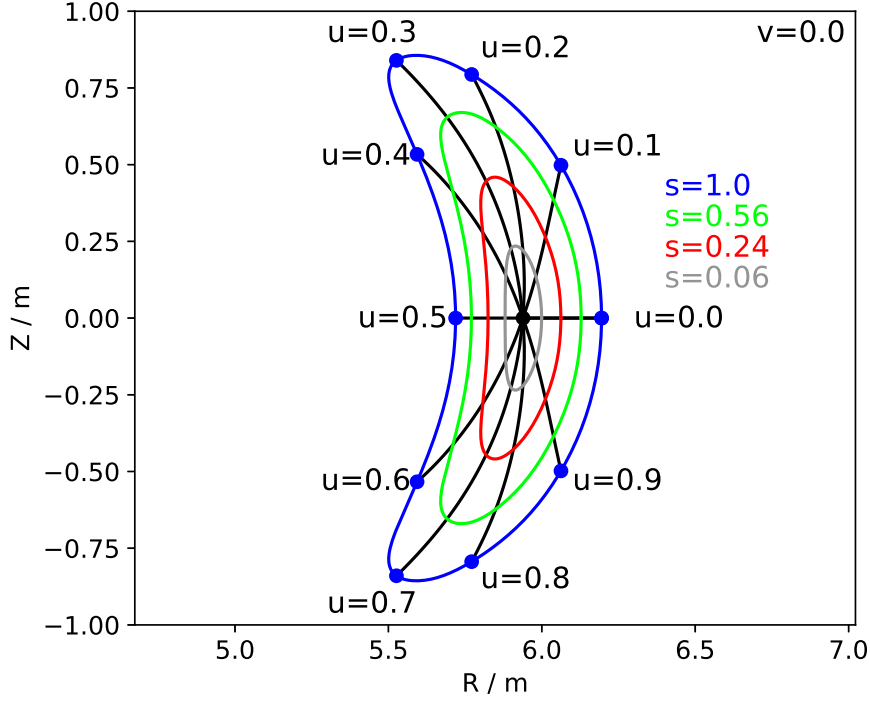


Fig. 16: This figure shows an example of the flux surface geometry for a W7-X MHD equilibrium and the normalized coordinates used to describe this geometry. The black dot in the center refers to the magnetic axis. The cross sections through the flux surfaces are shown in grey, red, green and blue and correspond to values of  $s$  as listed in the figure. Blue dots indicate positions on the LCFS corresponding to the values of the poloidal  $u$  coordinate written along the circumference of the LCFS.  $u = \text{const.}$  lines are shown in black. The toroidal position is identified by  $v = 0$  and corresponds to the bean-shaped plane in the center of module 1 (see Fig. 12 for an overview over the modules of W7-X).

The current density  $\mathbf{j}$  is computed from the magnetic flux density  $\mathbf{B}$  by Ampère's law and the contravariant components of the current density  $j^i$  for a location  $(s, u, v)$  are represented as two-dimensional Fourier series as well:

$$j^u = \sum_{m,n} j_{mn}^{u,\cos}(s) \cos(2\pi(mu - nn_{\text{fp}}v)) + j_{mn}^{u,\sin}(s) \sin(2\pi(mu - nn_{\text{fp}}v)) \quad (30)$$

$$j^v = \sum_{m,n} j_{mn}^{v,\cos}(s) \cos(2\pi(mu - nn_{\text{fp}}v)) + j_{mn}^{v,\sin}(s) \sin(2\pi(mu - nn_{\text{fp}}v)) \quad (31)$$

The individual Fourier harmonics of the current density can be computed independently from each other due to the orthogonality of the Fourier basis:

$$j_{mn}^{u,\cos}(s) = \frac{1}{\mu_0\sqrt{g}} \left( -n n_{\text{fp}} B_{s,mn}^{\sin}(s) - \frac{\partial B_{v,mn}^{\cos}}{\partial s} \right) \quad (32)$$

$$j_{mn}^{u,\sin}(s) = \frac{1}{\mu_0\sqrt{g}} \left( n n_{\text{fp}} B_{s,mn}^{\cos}(s) - \frac{\partial B_{v,mn}^{\sin}}{\partial s} \right) \quad (33)$$

$$j_{mn}^{v,\cos}(s) = \frac{1}{\mu_0\sqrt{g}} \left( \frac{\partial B_{u,mn}^{\cos}}{\partial s} - m B_{s,mn}^{\sin}(s) \right) \quad (34)$$

$$j_{mn}^{v,\sin}(s) = \frac{1}{\mu_0\sqrt{g}} \left( \frac{\partial B_{u,mn}^{\sin}}{\partial s} + m B_{s,mn}^{\cos}(s) \right) , \quad (35)$$

where  $\sqrt{g}$  is the Jacobian of the coordinate transform between VMEC and cylindrical coordinates. The cylindrical components of the current density are then computed from the contravariant representation:

$$j^R = j^u \frac{\partial R}{\partial u} + j^v \frac{\partial R}{\partial v} \quad (36)$$

$$j^Z = j^u \frac{\partial Z}{\partial u} + j^v \frac{\partial Z}{\partial v} . \quad (37)$$

For the details of the implementation, refer to Appendix A.

### 3.2.2. Magnetic Field and Vector Potential of Filamentary Wire Segments

The coil geometries are represented as strings of points along their respective geometric path. Space in between geometry definition points is approximated as straight wire segments.

Fig. 17 shows a single wire segment and the geometrical quantities used in the analytical expressions for computing the magnetic vector potential  $\mathbf{A}$  and magnetic flux density  $\mathbf{B}$  due to a current along this wire segment. For a current  $I$  along the wire segment, which goes from  $\mathbf{x}_i$  to  $\mathbf{x}_f$  in the sketch, the magnetic vector potential  $\mathbf{A}$  at a location  $\mathbf{r}$  is given by:

$$\mathbf{A}(\mathbf{r}) = \frac{\mu_0 I}{4\pi} \hat{\mathbf{e}} \ln \left( \frac{R_i + R_f + L}{R_i + R_f - L} \right) \quad (38)$$

where  $L$  is the length of the wire segment, i.e.  $L = |\mathbf{x}_i - \mathbf{x}_f|$  and  $R_{i,f} = |\mathbf{R}_{i,f}|$  with definitions as in the sketch [32]. The magnetic flux density vector  $\mathbf{B} = \nabla \times \mathbf{A}$  at location  $\mathbf{r}$  is given by:

$$\mathbf{B}(\mathbf{r}) = \frac{\mu_0 I}{4\pi} \hat{\mathbf{e}} \times \mathbf{R}_i \frac{2L(R_i + R_f)}{R_i R_f} \frac{1}{(R_i + R_f)^2 - L^2} . \quad (39)$$

These expressions are analytical and well-behaved for all locations around the wire segment, which are not located exactly on the wire segment.

Two critical cases exist in the computation of  $\mathbf{A}$ , where the convergence of a numerical implementation of these formulas had to be checked in detail. The first one is for evaluation points on the axis of the wire segment, i.e. for  $R_{\perp} = 0$ . The second one is for evaluation points located on the midplane of the wire segment, i.e.  $R_i = R_f \gg L$ . These cases have been examined in detail, as is shown in Sec. 4.1.1.

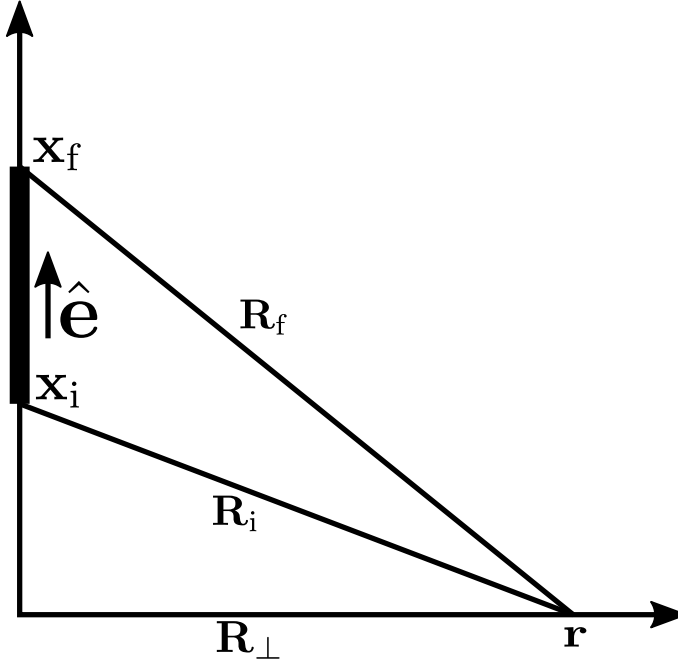


Fig. 17: Geometry of a filamentary wire segment. Start and end of the wire segment are denoted by  $\mathbf{x}_i$  and  $\mathbf{x}_f$ , respectively. The magnetic field and vector potential are to be evaluated at location  $\mathbf{x}$ . After Fig. 1 in Ref. [32].

A more sophisticated test is to compute the magnetic flux captured by a circular fluxloop in the magnetic field due to a current in a circular wire loop. This has been performed for the geometry as shown in Fig. 18 with vertical separation  $\Delta z = 0$ . The mutual inductance  $M$  indicates the flux through loop  $C_2$  if loop  $C_1$  is energized by a unit current of 1 A:

$$M = \mu_0 \sqrt{r_1 r_2} \left[ \left( \frac{2}{k} - k \right) K(k) - \frac{2}{k} E(k) \right] \quad \text{with} \quad (40)$$

$$k = \frac{2 \sqrt{r_1 r_2}}{\sqrt{(r_1 + r_2)^2 + \Delta z^2}}$$

with the radius  $r_1$  of loop  $C_1$ , the radius  $r_2$  of loop  $C_2$  and their distance along the common axis of symmetry  $\Delta z$  and complete elliptic integrals  $K(k)$  and  $E(k)$  of the first and second kind, respectively [33].

Then, for a scan of the fluxloop radius, the captured magnetic flux is computed as a line integral over the magnetic vector potential  $\mathbf{A}$  along the fluxloop geometry and compared to the analytical value given by Eq. (40).

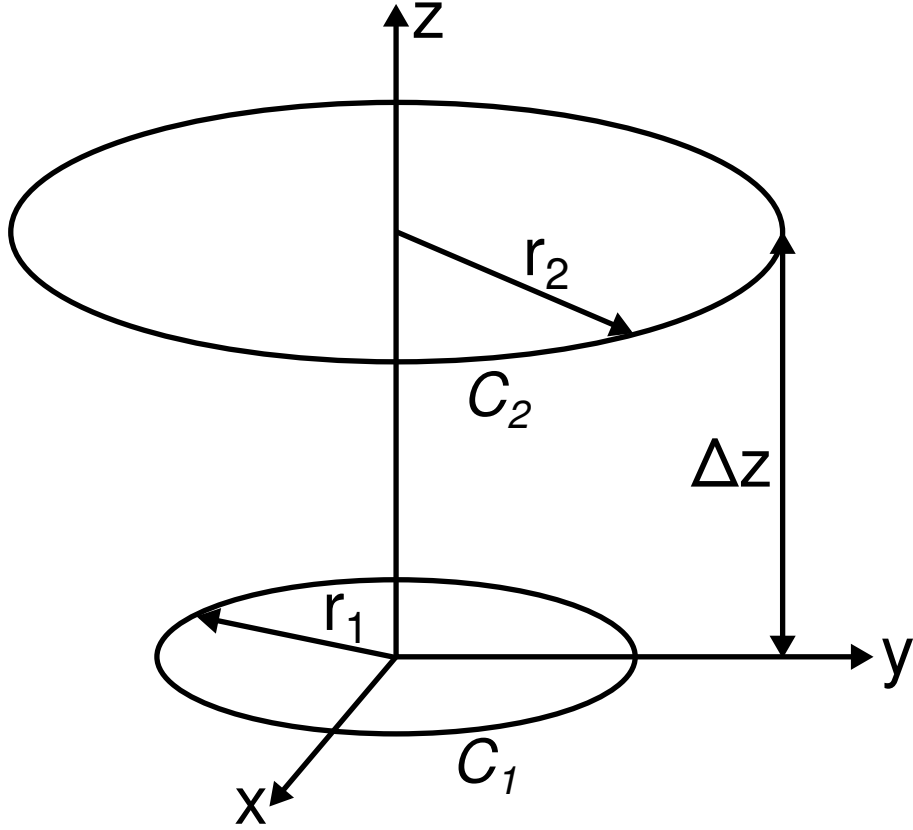


Fig. 18: Geometry of two concentric, parallel wire loops, for which the mutual inductance is given by Eq. (40).  $r_1$  and  $r_2$  are the radii of the two loops  $C_1$  and  $C_2$ . The distance between the loops along their common axis of symmetry is denoted by  $\Delta z$ .

### 3.2.3. Magnetics Response Prediction

Fluxloops are used to measure magnetic flux changes through their cross section. The magnetic flux  $\Phi$  passing through the cross section  $F$  of a fluxloop is given by

$$\Phi = \int_F \mathbf{B} \cdot d\mathbf{F} \quad . \quad (41)$$

With  $\mathbf{B} = \nabla \times \mathbf{A}$  and Stokes' theorem, the surface integral in Eq. (41) can be transformed into a line integral along the circumference  $\partial F$  of the fluxloop:

$$\Phi = \int_F (\nabla \times \mathbf{A}) \cdot d\mathbf{F} = \oint_{\partial F} \mathbf{A} \cdot d\mathbf{l} \quad . \quad (42)$$

If the current density in the plasma is known, the vector potential  $\mathbf{A}(\mathbf{r})$  at any point  $\mathbf{r}$  in space can be computed using the Biot-Savart law [33]:

$$\mathbf{A}(\mathbf{r}) = \frac{\mu_0}{4\pi} \int_V \frac{\mathbf{j}(\mathbf{r}')}{|\mathbf{r} - \mathbf{r}'|} d^3\mathbf{r}' \quad (43)$$

with the plasma volume  $V$ . Inserting this expression into the modeling equation for the fluxloop signal (42) and reversing the order of integrations leads to the following formula:

$$\Phi = \oint_{\partial F} \left( \frac{\mu_0}{4\pi} \int_V \frac{\mathbf{j}(\mathbf{r})}{|\mathbf{l} - \mathbf{r}|} d^3\mathbf{r} \right) \cdot d\mathbf{l} \quad (44)$$

$$\Leftrightarrow \Phi = \int_V \mathbf{j}(\mathbf{r}) \cdot \left( \frac{\mu_0}{4\pi} \oint_{\partial F} \frac{d\mathbf{l}}{|\mathbf{r} - \mathbf{l}|} \right) d^3\mathbf{r} \quad . \quad (45)$$

The inner integral now resembles the Biot-Savart expression (43) for a *unit current* along the geometric path  $\partial F$  of the *fluxloop*. The inner integral is therefore called the “response vector potential”  $\mathbf{a}(\mathbf{r})$  of the fluxloop:

$$\mathbf{a}(\mathbf{r}) = \frac{\mu_0}{4\pi} \oint_{\partial F} \frac{d\mathbf{l}}{|\mathbf{r} - \mathbf{l}|} \quad . \quad (46)$$

In the literature [34], this equivalence is referred to *magnetic reciprocity*. The use of a precalculated  $\mathbf{a}(\mathbf{r})$  from Eq. (46) reduces the computational effort when computing the prediction for a magnetic sensor signal  $\Phi$  multiple times from changing current densities, as in a reconstruction algorithm, since only a volume integral over the plasma volume has to be carried out:

$$\Phi = \int_V \mathbf{j}(\mathbf{r}) \cdot \mathbf{a}(\mathbf{r}) d^3\mathbf{r} \quad . \quad (47)$$

The current  $I$  enclosed by a closed Rogowski coil is computed by integrating the current density  $\mathbf{j}$  over the cross section  $F$  of the Rogowski coil:

$$I = \int_F \mathbf{j} \cdot d\mathbf{F} \quad . \quad (48)$$

Using Ampère’s law and Stokes’ theorem, Eq. (48) can be transformed into a line integral along the Rogowski coil circumference:

$$I = \frac{1}{\mu_0} \int_F (\nabla \times \mathbf{B}) \cdot d\mathbf{F} = \frac{1}{\mu_0} \oint_{\partial F} \mathbf{B} \cdot d\mathbf{l} \quad . \quad (49)$$

If the current density distribution in the plasma is known, the magnetic field  $\mathbf{B}$  at any point in space can be computed using the Biot-Savart law (43) and  $\mathbf{B} = \nabla \times \mathbf{A}$ :

$$\nabla \times \mathbf{A}(\mathbf{r}) = \mathbf{B}(\mathbf{r}) = \frac{\mu_0}{4\pi} \int_V \mathbf{j}(\mathbf{r}') \times \frac{\mathbf{r} - \mathbf{r}'}{|\mathbf{r} - \mathbf{r}'|} d^3\mathbf{r}' \quad . \quad (50)$$

Inserting this into the expression (49) results in the following equation for the current through the Rogowski coils:

$$I = \frac{1}{\mu_0} \oint_{\partial F} \left( \frac{\mu_0}{4\pi} \int_V \mathbf{j}(\mathbf{r}) \times \frac{\mathbf{l} - \mathbf{r}}{|\mathbf{l} - \mathbf{r}|} d^3\mathbf{r} \right) \cdot d\mathbf{l} \quad . \quad (51)$$

In order to reduce computational effort when repeatedly computing the signal prediction for the fixed geometry of a diagnostic coil, magnetic reciprocity can be found again:

$$I = \frac{1}{\mu_0} \int_V \mathbf{j}(\mathbf{r}) \cdot \left( \frac{\mu_0}{4\pi} \oint_{\partial F} d\mathbf{l} \times \frac{\mathbf{l} - \mathbf{r}}{|\mathbf{l} - \mathbf{r}|} \right) d^3\mathbf{r} \quad . \quad (52)$$

A response potential  $\mathbf{b}(\mathbf{r})$  for the Rogowski coil is given by

$$\mathbf{b}(\mathbf{r}) = \frac{\mu_0}{4\pi} \oint_{\partial F} d\mathbf{l} \times \frac{\mathbf{l} - \mathbf{r}}{|\mathbf{l} - \mathbf{r}|} \quad , \quad (53)$$

which is the magnetic field of a filamentary wire along the guiding path of the Rogowski coil. Then, Eq. (51) can be rewritten as:

$$I = \frac{1}{\mu_0} \int_V \mathbf{j}(\mathbf{r}) \cdot \mathbf{b}(\mathbf{r}) d^3\mathbf{r} \quad . \quad (54)$$

The geometries of Rogowski coils and fluxloops are specified as lists of points along the real geometric path of the pickup coils. Filamentary wire segments are used to model the sensor in between the definition points. The response vector potential and response magnetic field, respectively, are given as superposition of the individual contributions for a unit current from each of the wire segments along the path definition of a given pickup coil.

The current density is defined on the flux surface geometry of the equilibrium calculation, i.e. its value in between flux surfaces could only be computed by radial interpolation of the current density Fourier coefficients. Therefore, the current density is evaluated on a uniform grid in  $s$ ,  $u$  and  $v$ . The flux surface geometry is subsequently computed by evaluating the Fourier series for  $R$  and  $Z$  on the same  $(s, u, v)$  grid.

In computation of the volume integrals Eq. (47) and Eq. (54) over the plasma volume, current density and response potential have to be evaluated at the same locations. The flux surface geometry however changes with each equilibrium calculation, so the response potential would have to be recomputed for each iteration of the equilibrium reconstruction procedure. Only the grid in toroidal  $v$  direction does not change, which defines the toroidal cutplanes, on which the current density and flux surface geometry is evaluated.

The response potentials are precalculated on a rectangular grid in cylindrical coordinates  $(R, \varphi, Z)$  at the same toroidal locations as used in the VMEC calculation; leading to a necessity for recomputation of the response matrices only if the toroidal resolution of the equilibrium calculation is changed.

For computing the volume integral, the uniform flux coordinate grid is used. Given by the flux surface geometry, the response potential is interpolated from the rectangular grid in the toroidal cutplanes to the flux coordinate grid. Two-dimensional linear interpolation can be used if the response grid is chosen fine enough and the response potential is smooth. The two geometries (flux grid and rectangular grid for response matrices) in one exemplary toroidal cutplane are illustrated in Fig. 19. Bilinear interpolation as outlined in Ref. [34] is used. The interpolated value at the location of the black dot in the figure is given by the weighted average of the four values on neighboring grid locations, which are indicated by the crosspoints of the background grid and colored dots in the inset. The weighting coefficients correspond to the rectangular areas, as illustrated in the inset by the four colors, which are located diagonally opposite of the respective background grid location. Then, the response potential value at e.g. the blue dot is contributing to the interpolated value at the location of the black dot by a factor given by the fraction of the blue area to the total area spanned between the four colored dots.

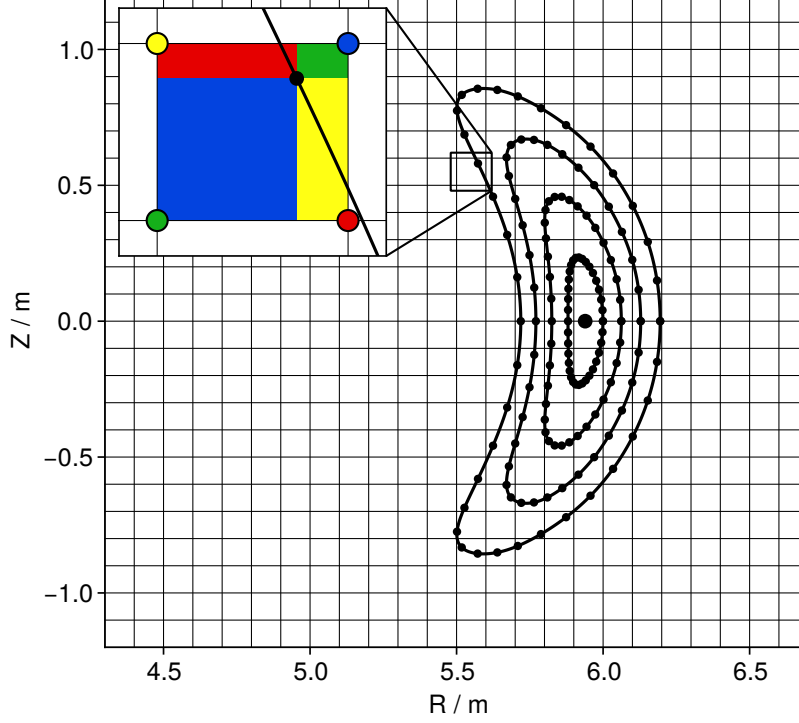


Fig. 19: Response matrices for the magnetic diagnostics are computed on crosspoints of the rectangular background grid in this figure. For a given flux surface geometry (thick solid lines), the response potential is evaluated at the positions indicated by the black dots, which corresponds to a uniform grid in  $u$  and  $s$ . Two-dimensional linear interpolation is used as illustrated in the inset, where contributions from neighboring grid locations (colored dots) are weighted by their diagonally opposite area sizes section (colored rectangles).

The resulting integration is done as follows for a fluxloop:

$$\Phi = \int_0^{2\pi} \int_{Z_0(\varphi)}^{Z_1(\varphi)} \int_{R_0(z,\varphi)}^{R_1(z,\varphi)} \mathbf{j}(r, \varphi, z) \cdot \mathbf{a}(r, \varphi, z) dr dz d\varphi \quad (55)$$

$$= \int_0^1 \int_0^1 \int_0^1 \mathbf{j}(s, u, v) \cdot \mathbf{a}(s, u, v) \sqrt{g} ds du dv \quad (56)$$

$$= \int_0^1 \int_0^1 \int_0^1 \left[ \left( j^u \frac{\partial R}{\partial u} + j^v \frac{\partial R}{\partial v} \right) a^R + R j^v a^\varphi + \left( j^u \frac{\partial Z}{\partial u} + j^v \frac{\partial Z}{\partial v} \right) a^Z \right] \sqrt{g} ds du dv \quad (57)$$

with

$$\mathbf{a}(s, u, v) = \mathbf{a}(R(s, u, v), 2\pi v, Z(s, u, v)) \quad (58)$$

by interpolation from a tabulated  $\mathbf{a}(r, \varphi, z)$  onto the flux grid locations  $(R(s, u, v), 2\pi v, Z(s, u, v))$ . Since the plasmas LCFS stays a significant distance apart from the diagnostics geometry (otherwise, it would burn the diagnostics coils), singularities due to the crossing of the diagnostic path through the cutplanes do not pose a limitation in this implementation and the response matrices are well-behaved in the interpolation region; thereby, linear interpolation does not impose a significant error given the response matrix precomputation grid is chosen fine enough. For the fluxloop prediction, a closed-loop line integral over the vector potential is computed. This does not need sophisticated handling of the endpoints of the integration line, since the loop closes on itself. However, the predictions for the segments of the Rogowski coils are computed one after another as separate line integrals along the guiding curves of the segments and summed up later on. Here, appropriate handling of the endpoints of the integration lines along the guide curves, e.g. by a trapezoidal rule, improves the accuracy of the prediction.

Since a stellarator is usually designed to consist of several modules along the toroidal direction, a rotational symmetry between the modules exist. Inside each of these modules, another symmetry, called stellarator symmetry can exist. This is a flip-rotate-symmetry about the midplane in the middle of the module and can be identified by the following properties of the flux surface geometry:

$$R(s, \theta, \varphi) = R(s, -\theta, -\varphi) \quad (59)$$

$$Z(s, \theta, \varphi) = -Z(s, -\theta, -\varphi) \quad (60)$$

If both toroidal and stellarator symmetry are assumed for a MHD equilibrium calculation, the computational effort reduces to  $1/(2 \cdot n_{\text{fp}})$  of the total computational effort for the case where no symmetries were assumed.

The response potential is computed on each toroidal cutplane throughout the whole machine, but stored only on the grid locations corresponding to one half-module. The contributions to the response potential from other half-modules than the one being stored are mirrored and rotated appropriately into the stored half-module and added up to give the compressed response matrix making use of the stellarator-symmetric grid properties. Also, response matrices for computing the magnetic diagnostics response need to be stored only for these positions to allow computing the current density volume integral over the whole plasma volume. Fig. 20 shows a reduced subset of the response matrix grid used for one half-module of W7-X and the corresponding stellarator-symmetric summation scheme.

After computation of the current density inside the plasma, the Biot-Savart volume integrals over the plasma volume have to be computed. In both the toroidal and the poloidal angle-like coordinates, the integration is carried out over a closed domain, i.e. from 0 to  $2\pi$ . If the toroidal and poloidal value ranges are discretized into a finite number of steps, an integration over an open domain would require sophisticated handling of the domain edges, e.g. using Simpson's rule. However, for closed domains, the edges close on themselves and direct summation of the individual contributions can be carried out. For the radial direction, an open domain is to be integrated, since  $0 \leq s \leq 1$ . This results in the requirement to weight the innermost and outermost flux surface contributions with a factor of 1/2 when directly summing up the resulting contributions in order to carry out a trapezoidal integration.

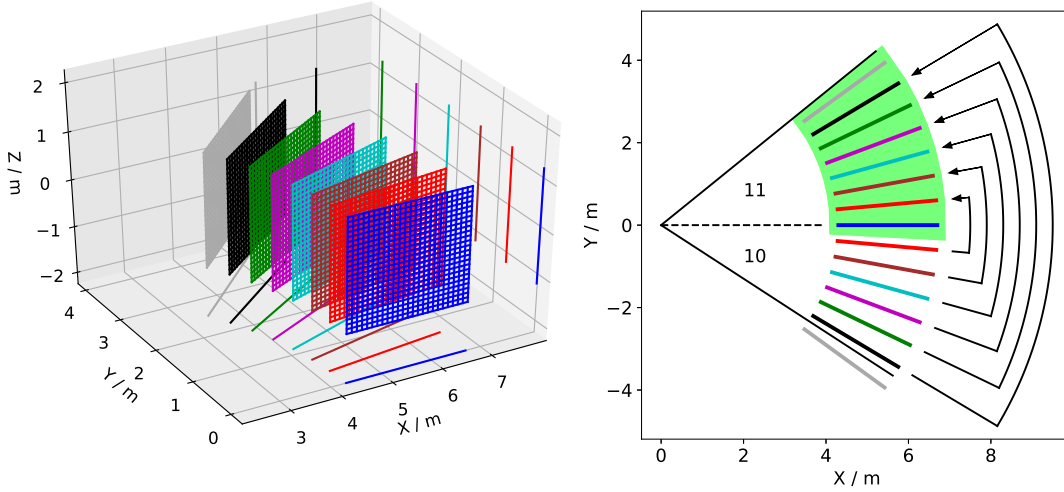


Fig. 20: The cylindrical grid in one half-module of W7-X is shown in the left panel for several toroidal cutplanes. Lines on the floor and on the walls of the bounding box are projections of the grid to guide the eye. In the right panel, the summation according to stellarator symmetry is illustrated. For one of the modules of W7-X, the magnetic responses are computed for e.g. twelve positions along the toroidal direction (radial solid colored lines in between the thinner black lines defining the module boundaries). Then, to make use of its stellarator symmetric properties, the reponse potentials from the second half-module are mirrored into the first half-module as indicated by the arrows. For the first and the last grid locations, no mirrorable counterpart exists in the second half-module and no arrows point at them. The grey radial line at the bottom is the counterpart to the grey line at the top, but belongs to module 51. The green shaded region contains the toroidal locations, which are subsequently saved.

For closed Rogowski coils, the formulation in Eq. (51) uses a closed loop line integral over the magnetic field to compute the predicted signal for the Rogowski coil. For segmented Rogowski coils, the method is similar, in that a line integral over the magnetic field has to be computed as well, but the motivating argument has to be more general, since a segmented Rogowski coil segment does not close on itself. This can be accomplished by using a multipole expansion of the integral (46) for the detailed Rogowski coil geometry as presented in Ref. [34].

In W7-X, the closed Rogowski coils are constructed similarly to the segmented Rogowski coils, with the only difference that for the closed Rogowski coils, all segments are already wired in series connection in the plasma vessel and only a single signal is acquired. When computing the predicted signal for a closed Rogowski coil, it is therefore important to compute the signal contributions as line integrals over the magnetic field along each segment of the closed Rogowski coil separately and add them up afterwards instead of computing the line integral along the joined path in the geometric definition of the closed Rogowski coil. Doing so would result in artificial contributions due to the line segments from the end of one segment to the beginning of the next segment, where in reality no Rogowski coil segment exists at that location.

### 3.3. Integrated Modeling Approach

In this section, the Minerva framework will be introduced, which was used to implement most of the numerical methods used throughout this thesis. An integrated modeling approach has been applied to analyze data from magnetic diagnostic calibration experiments and to perform plasma reconstructions. The details of these methods will be presented.

#### 3.3.1. Bayesian Data Analysis in the Minerva Framework

The Minerva framework [29] provides the user with a sophisticated infrastructure for scientific modeling. It features full non-linear Bayesian error propagation for any physics model and interfaces well to established computer codes as VMEC, Extender [35] and a field-line tracing code [15] by use of SOAP<sup>4</sup>-based webservice [36]. The latter provide access of the interfaced computer codes to on-site scientists, resulting in coherent usage of the same versions of codes by colleagues and convenient sharing of results. Standardized physics model specifications allow easy testing of the validity of different models given the measured data.

The Minerva framework is regularly used for automatized preprocessing and archiving of raw experimental data for various diagnostics at W7-X. Available inference models include profile diagnostics as Thomson scattering [19], the electron cyclotron emission diagnostic [37] and the X-ray imaging crystal spectrometer [38].

The main aim of the Minerva framework is to provide the user with infrastructure to handle the complexity of integrated modeling of modern fusion experiments, where models for single diagnostics regularly feature several hundred free parameters and usually data from many of these diagnostics has to be combined to model the complete experiment in an integrated modeling approach. Several inversion methods are implemented in the Minerva framework. Inversion algorithms can be universally applied to any model specified as a *Bayesian Graphical Model*, since the forward problem has to be specified in a standardized format. One outcome of this work is the forward model used for reconstruction of MHD equilibria from the measured signals of the magnetic diagnostics.

The inversion method applied to this problem is called Maximum Posterior (MAP) inversion. For each graphical model, the combined posterior probability function (PDF) can be computed using Bayes' formula [18]. Given the model, the inversion algorithm performs a pattern search according to the algorithm by Hooke and Jeeves [39] to find the maximum of the posterior probability distribution function, i.e. the most likely set of free parameters given the measured data and specified uncertainties. A schematic illustration of the pattern search algorithm is depicted in Fig. 21. For a given posterior probability distribution, the maximum of the PDF is searched for. The pattern search algorithm by Hooke and Jeeves is implemented in the Minerva framework to accomplish this. Normally, the PDF landscape is not known completely and has only been mapped out for the purpose of this figure. The algorithm starts at a given position, here at the center of the red cross. Then it performs several *explorative* steps, indicated by the red lines and dots where the PDF is sampled and compared to the value at the starting position. If the algorithm finds a higher value for the PDF in one of the explorative steps, it moves its center there in a *moving* step and starts over again. If no improvement was found in the vicinity of the current location for a given step size (distance from current position to the explorative positions), the step size is decreased (typically halved). This is performed in a

<sup>4</sup>Originally, Simple Object Access Protocol. Also: SOA = service oriented architecture

$n$ -dimensional hyperspace, where  $n$  is the number of free parameters. For the purpose of this figure, only the two free parameters central pressure  $p$  and toroidal current  $I_{\text{tor}}$  have been selected.

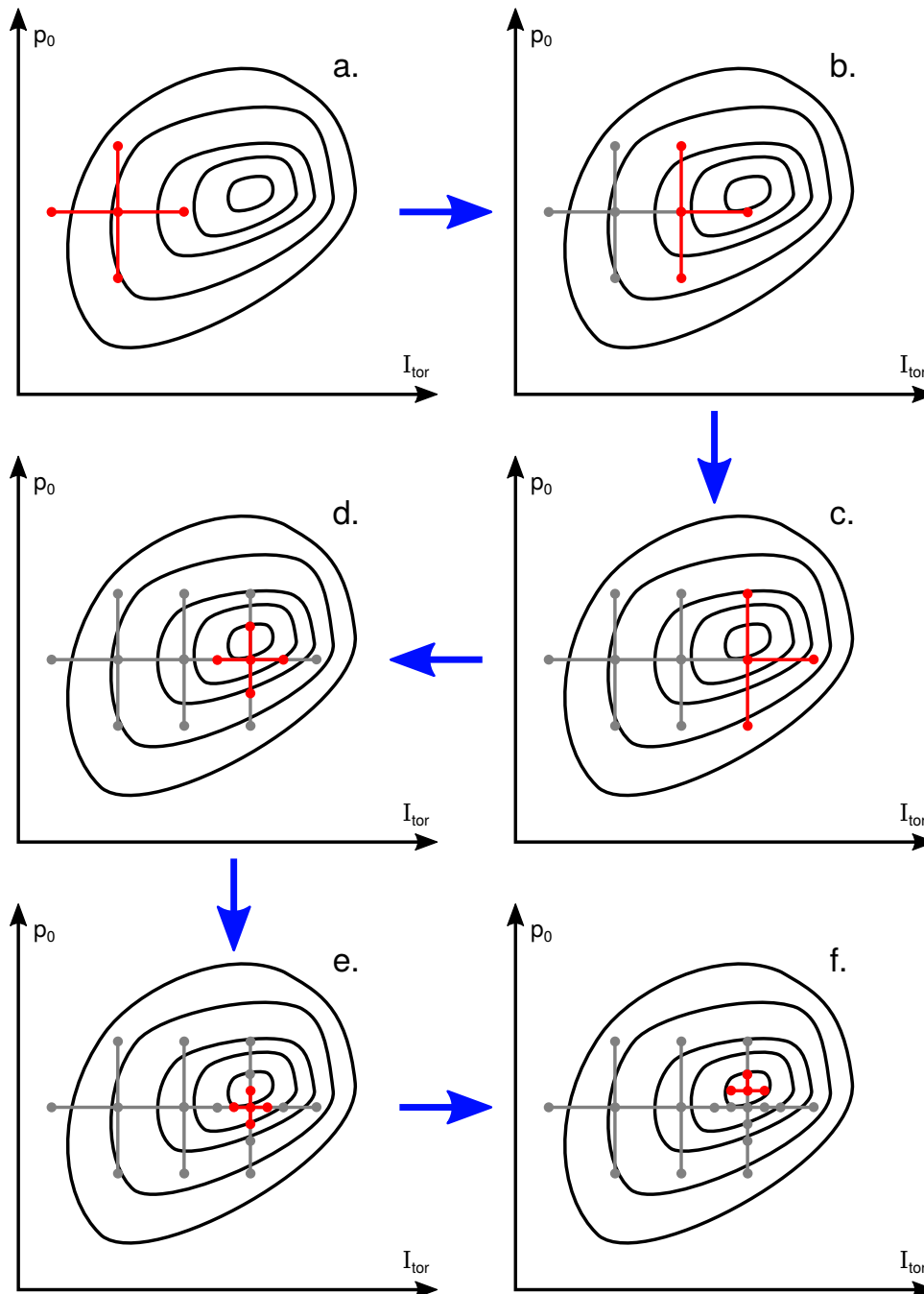


Fig. 21: Illustration of the Hooke and Jeeves Algorithm for an exemplary potential landscape (black solid lines in the background) for two free parameters  $I_{\text{tor}}$  and  $p_0$ . The labels a.-f. and blue arrows indicate the order of iterations. Red dots and lines mark explorative steps of the algorithm and grey lines and dots indicate explorative steps performed in previous iterations.

### 3.3.2. Magnetic Diagnostics Calibration Experiments

Before attempting to reconstruct the MHD equilibrium in a plasma based on the magnetic diagnostics measurements, many error sources in the reconstruction methods can be excluded by analyzing measured signals from experiments where no plasma is present, but the external coil currents are varied over time. This includes especially the coil current ramps at the beginning and end of an experiment day, when the superconducting coils are brought into operation and out of it. The evolving magnetic field induces voltages in the pickup coils by Faraday's law [33], which are measured and compared against modeling results based on Biot-Savart calculations.

Tests include current ramps in various coils in W7-X, consisting of the non-planar coils and the trim coils. The neutron counter calibration rail provides another source for calibration, when installed. All seven main field coil currents are ramped simultaneously to sustain constant coil current ratios and thereby constant ratios of the magnetic forces between the coils. This prevents unexpected load scenarios possibly leading to damages on the coils and their support structures. Comparisons of the measured magnetic diagnostic signals therefore have to be based on a superposed magnetic field from all main field coils. The trim coils can be energized independently and therefore, asymmetric magnetic fields, which do not possess toroidal symmetry, can be generated. Local comparisons, i.e. on the localization of the diagnostic coils, can thereby be conducted. The neutron counter calibration rail spans approximately along the magnetic axis and is used to mimic a net toroidal current, similar to the bootstrap current in plasma operation. This method is especially useful to calibrate the complete Rogowski coils, as these directly measure the net toroidal current.

By ramping the trim coil currents one after another, it can be checked whether the induced signals in the magnetic diagnostics in the vicinity of the trim coils are larger than the ones of diagnostics distributed over the rest of the machine. The trim coils and the magnetic diagnostics in operation during the latest experimental campaign OP1.2a of W7-X are shown in Fig. 22. The predicted signals for the magnetic diagnostics are computed from the currents in the trim coils using line integrals over the magnetic field and vector potential due to the trim coil currents. This is equivalent to computing the mutual inductances for the trim coil geometries and the magnetic diagnostic geometries and using these as the scaling factor between coil current ramp rate and induced voltage in the diagnostics.

In order to accurately calibrate the Rogowski coils, a conductor along the minor torus axis is favourable. This calibration was possible using the aluminum rail used to align a neutron source to calibrate the neutron counters in W7-X. The geometry of this rail and the magnetic axis of the standard magnetic configuration are shown in Fig. 23.

During coil current ramps and transient phases of the plasma, eddy currents are induced in all surrounding and enclosed conducting parts, especially the plasma vessel and the cryostat. All magnetic measurements are influenced by this and therefore, to analyze the magnetic field ramps, induced currents need to be taken into account. This can be done via finite element methods, e.g. as implemented in the SPARK code [40].

In a first approach, the plasma vessel is electrically approximated by a single wire loop with inductance  $L$  and resistance  $R$ . This is illustrated in Fig. 24a. The trim coil  $L_{tc}$  is energized by a time-dependent current  $I_{tc}(t)$ . The magnetic field due to the current in the trim coil induces a voltage  $U_{ind}(t)$  in the magnetic diagnostic pickup coil  $L_{diag}$ . Due to the changing magnetic field penetrating through the plasma vessel and the cryostat,

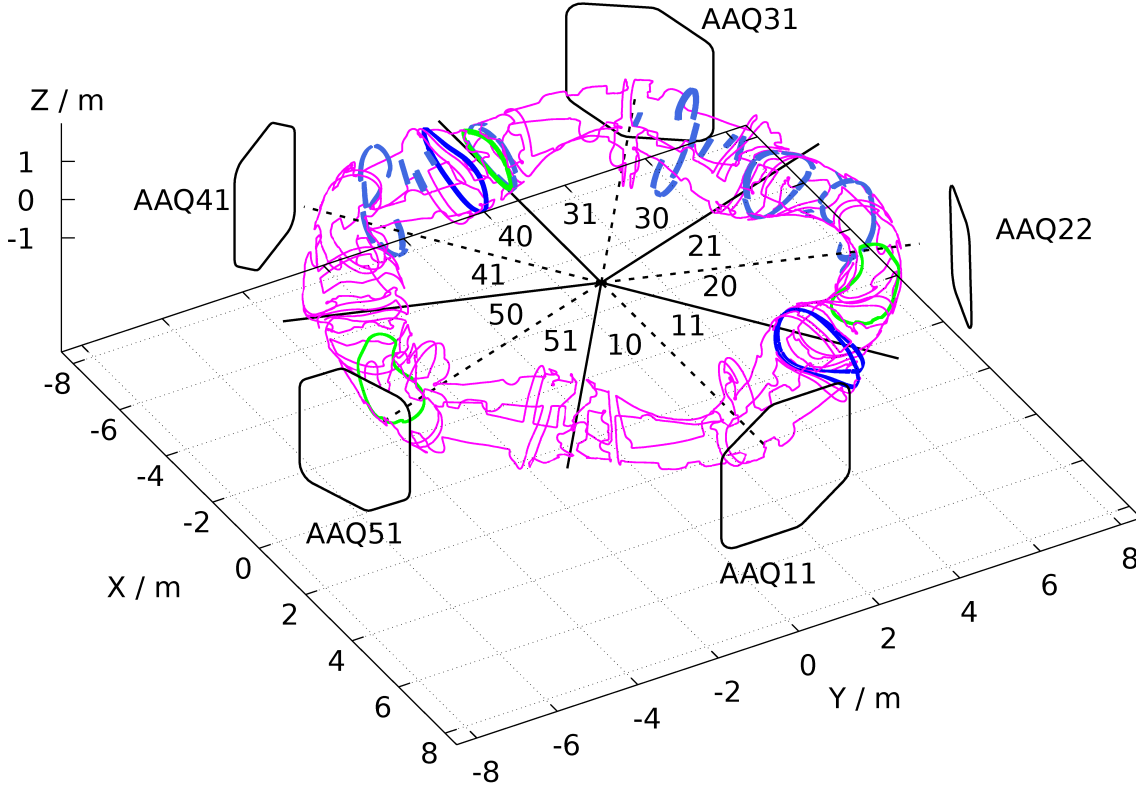


Fig. 22: The magnetic diagnostics (colored) and trim coils (black loops around the machine) are shown here.

eddy currents  $I_{\text{eddy}}(t)$  are induced. The induced currents generate their own magnetic field, which is superposed on the magnetic field of the coils and lowers its strength, thereby lowering the pickup coil induced voltage signal measured by the magnetic diagnostics.

If the eddy current paths in the vessel are approximated by a single wire loop, the temporal evolution of the eddy currents can be estimated. This model is illustrated in Fig. 24b. Eddy currents rise due to a change in the magnetic flux  $\Phi_m$  passing through the plasma vessel. For a single wire loop, this can be modeled as an induced voltage  $-\text{d}\Phi_m/\text{d}t$ . This induced voltage is then applied to a series circuit of the inductance  $L$  of the eddy current path and its resistance  $R$ , resulting in a current  $I_{\text{eddy}}(t)$ . The eddy current gives rise to a voltage  $U_L$  across the inductance  $L$  according to:

$$U_L = L \cdot \frac{\text{d}I_{\text{eddy}}}{\text{d}t} \quad (61)$$

and to a voltage  $U_R = R \cdot I_{\text{eddy}}$  across the resistance  $R$  of the eddy current path.

By Kirchhoff's law, the sum of all voltages in a closed circuit has to cancel:

$$\frac{\text{d}\Phi_m}{\text{d}t} = L \cdot \frac{\text{d}I_{\text{eddy}}}{\text{d}t} + R \cdot I_{\text{eddy}} \quad (62)$$

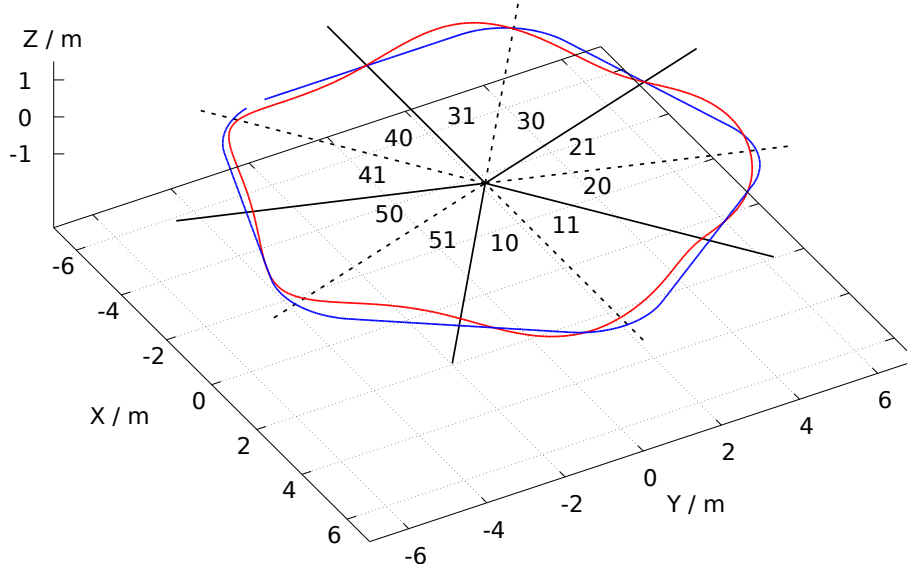


Fig. 23: The modules of W7-X are labeled as (module half-module). The rail for the neutron source (blue) was aligned to approximately follow the magnetic axis (red) of the standard magnetic configuration. A gap in the rail in module 40 is used for connection of a current source.

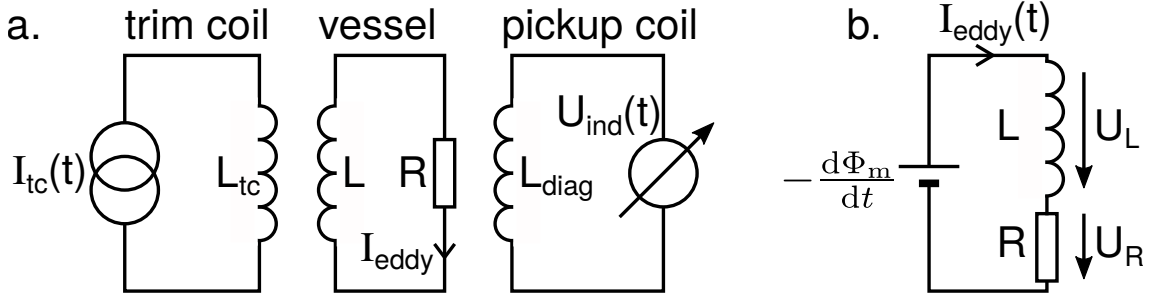


Fig. 24: Trim coil with eddy currents in the vessel modeled by a single inductance  $L$  and resistance  $R$  and a pickup coil of the equilibrium magnetic diagnostics.

This is a linear, inhomogenous, first-order differential equation for  $I_{eddy}(t)$ . The solution to the corresponding homogenous differential equation can be obtained by separation of variables:

$$\begin{aligned}
 0 &= L \cdot \frac{dI_{eddy}}{dt} + R \cdot I_{eddy} \\
 \Leftrightarrow dt &= -\frac{L}{R} \cdot \frac{dI_{eddy}}{I_{eddy}} \\
 \Leftrightarrow \int_{t_0}^t dt' &= -\frac{L}{R} \int_{I_0}^{I_{eddy}} \frac{dI'_{eddy}}{I'_{eddy}} \\
 \Leftrightarrow t - t_0 &= -\frac{L}{R} \ln(I_{eddy} - I_0) \\
 \Leftrightarrow I_{eddy}(t) &= I_0 \cdot \exp\left(-\frac{t - t_0}{\tau}\right) \quad \text{with } \tau = \frac{L}{R} . \quad (63)
 \end{aligned}$$

The inhomogenous differential equation is solved by variation of constants. According to Ref. [41], an inhomogenous differential equation of type

$$\frac{dy}{dt} = a(t)y(t) + b(t) \quad \text{with} \quad A(t) = \int_{t_0}^t a(t') dt' \quad (64)$$

is solved by

$$y(t) = e^{A(t)} \int_{t_0}^t b(t') e^{-A(t')} dt' \quad . \quad (65)$$

Here,  $y(t) = I_{\text{eddy}}(t)$ ,  $a(t) = -1/\tau$ ,  $b(t) = -1/L \cdot d\Phi_m/dt$  and  $A(t) = -(t - t_0)/\tau$ . For a constant ramp rate of the trim coil current, corresponding to  $b(t) = \text{const.}$ , the solution to Eq. (62) is given by:

$$I_{\text{eddy}}(t) = -\frac{1}{R} \frac{d\Phi_m}{dt} \left(1 - e^{-(t-t_0)/\tau}\right) \quad . \quad (66)$$

The first term corresponds to an ohmic current in the eddy current path due to a constant ramp rate of the trim coil current. At the beginning of the ramp, the eddy current is damped by the self-inductance  $L$  of the eddy current path. After a time  $t_5 - t_0 \approx 5\tau$ , the eddy current is expected to have evolved to within  $\exp(-(t_5 - t_0)/\tau) \approx 1\%$  of its final value. Note that this evolution of the eddy current is only valid for the onset of a coil current ramp. If the current is decided to be ramped down, before the eddy currents could equilibrate, the energy conservation principle has to be applied in order to model the decay of the eddy currents present in the vessel at the time of stopping the current ramp. However, this process is symmetric to the case of eddy current induction and therefore, the rise and fall time constants are equal. The time evolution of a decaying eddy current is given by Eq. (63) for the current  $I_0$  being present at beginning of the decay phase. In Fig. 25, the resulting time trace of an induced signal during a current ramp in a trim coil is illustrated.

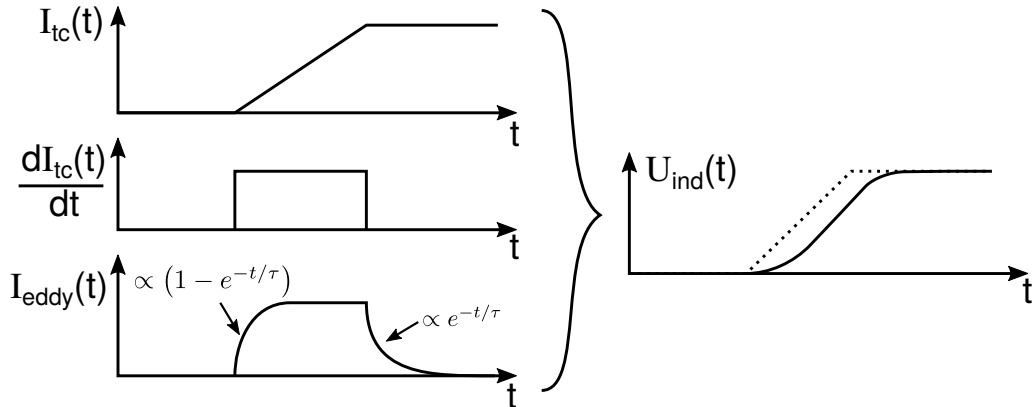


Fig. 25: A trim coil current ramp is shown in the top left panel. It features a constant ramp rate during the ramp (center left panel). The eddy currents in the plasma vessel evolve according to Eq. (66), as is shown in the lower left panel. On the right, the resulting magnetic flux signal as measured by a pickup coil is shown as a solid line. The dashed line indicates the predicted signal if eddy currents in the plasma vessel are not taken into account.

### 3.3.3. Prediction Model for VMEC and Magnetic Diagnostics

In this section, the Bayesian Graphical Model (“graph”) for computing a VMEC equilibrium and predicting the magnetic diagnostic measurements, which was implemented in the Minerva framework, is presented. The working model is the main result of this work. In Fig. 27, a sketch of this graph is presented and the graph as auto-generated by the Minerva framework is shown in Fig. 28.

*Free parameters* to be adjusted in the reconstruction are indicated in light blue, whereas *observations*, which are nodes to compare measurements against predictions, are indicated in light grey.

For W7-X, absolute timestamps indicate the nanoseconds since 1970-01-01, 00:00 in UTC time. Any experiment program and timestamps within this experiment (i.e. relative to its start) can be uniquely identified up to nanosecond accuracy by these absolute time stamps. The selected time stamp is used when loading the main field coil currents and the measurements by the magnetic diagnostics from the central W7-X data archive.

The main coil currents and the main coil geometry are used to compute the confinement magnetic field on a cylindrical grid, which is predefined in the model. This serves as the background magnetic field, which is used in the VMEC computation. Apart from the confining magnetic field, more input parameters are needed to compute a MHD equilibrium using VMEC. These include the enclosed toroidal magnetic flux,  $\Phi_{\text{edge}}$ , the pressure profile and the toroidal current profile. Here, prescribed functions internal to VMEC are used to specify the radial dependence of the profiles. For the pressure, a parameterized power function is used:

$$p(s) = am0 \cdot (1 - s^{am1})^{am2} \quad (67)$$

with the parameters  $am0$ ,  $am1$  and  $am2$ . For the enclosed toroidal current, an arctangent functions is used:

$$I(s) = ac0 + \frac{2}{\pi} \cdot ac1 \cdot \arctan \left( \frac{ac2 \cdot s^{ac3}}{(1 - s)^{ac4}} \right) \quad (68)$$

with the parameters  $ac0$ ,  $ac1$ ,  $ac2$ ,  $ac3$  and  $ac4$ .

Example profile shapes, as used for the reconstructions in this thesis, are shown in Fig. 26.

From the VMEC computation, the flux surface geometry and the covariant magnetic field is used to compute the current density components.

The geometry of the magnetic diagnostics is taken to tabulate response potentials in a response matrix on the given cylindrical grid. Using the flux surface geometry from the VMEC computation, the response factors are interpolated to the flux surface grid and the volume integrals over the scalar product of response vector and current density at each location within the plasma are carried out according to Eq. (47) and (54). This gives the predicted signal for the magnetic diagnostics. Finally, the measured signals and error estimates are taken from the W7-X data archive and compared to the predictions in the observation nodes.

It proved be useful to include additional constraints on the MHD equilibrium output on top of the predictions for the magnetic diagnostic signals alone. *Virtual observations* are observation nodes added to the graph, which get their target data to be matched in the reconstruction process from constant values, predefined by the user. Here, a virtual observation on the rotational transform at the LCFS, called  $\iota_{\text{edge}}$ , was introduced. As the boundary of a VMEC calculation has to feature a smooth transition to the vacuum

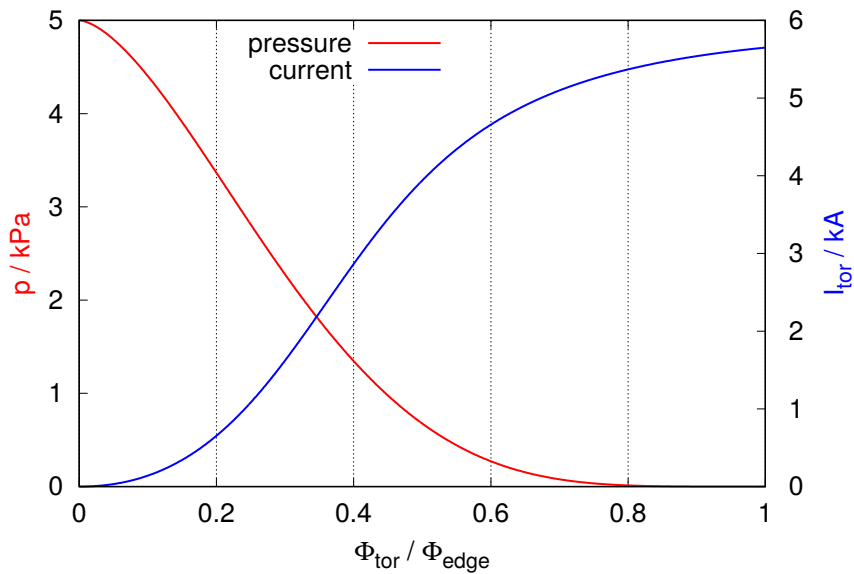


Fig. 26: Example profile shapes for pressure (red) and enclosed current (blue). The horizontal axis denotes the normalized toroidal magnetic flux, i.e. 0 is at the magnetic axis and 1 is at the LCFS. The values used to generate this plot are  $am\{0-2\} = \{5, 1.6, 5\}$  and  $ac\{0-4\} = \{0, 5.65, 4.05, 2.06, 1\}$ .

magnetic field, this fixes the position and shape of the LCFS for the reconstruction. The standard magnetic configuration of W7-X was chosen for the first reference equilibrium reconstructions and a value of  $\iota_{\text{edge}} = (0.97 \pm 0.001)$  was targeted in the reconstruction. This leaves some radial space up to the position of the magnetic island chain at  $\iota = 5/5$  used for island divertor operation. This additional observation node is included in the graph shown in Fig. 28.

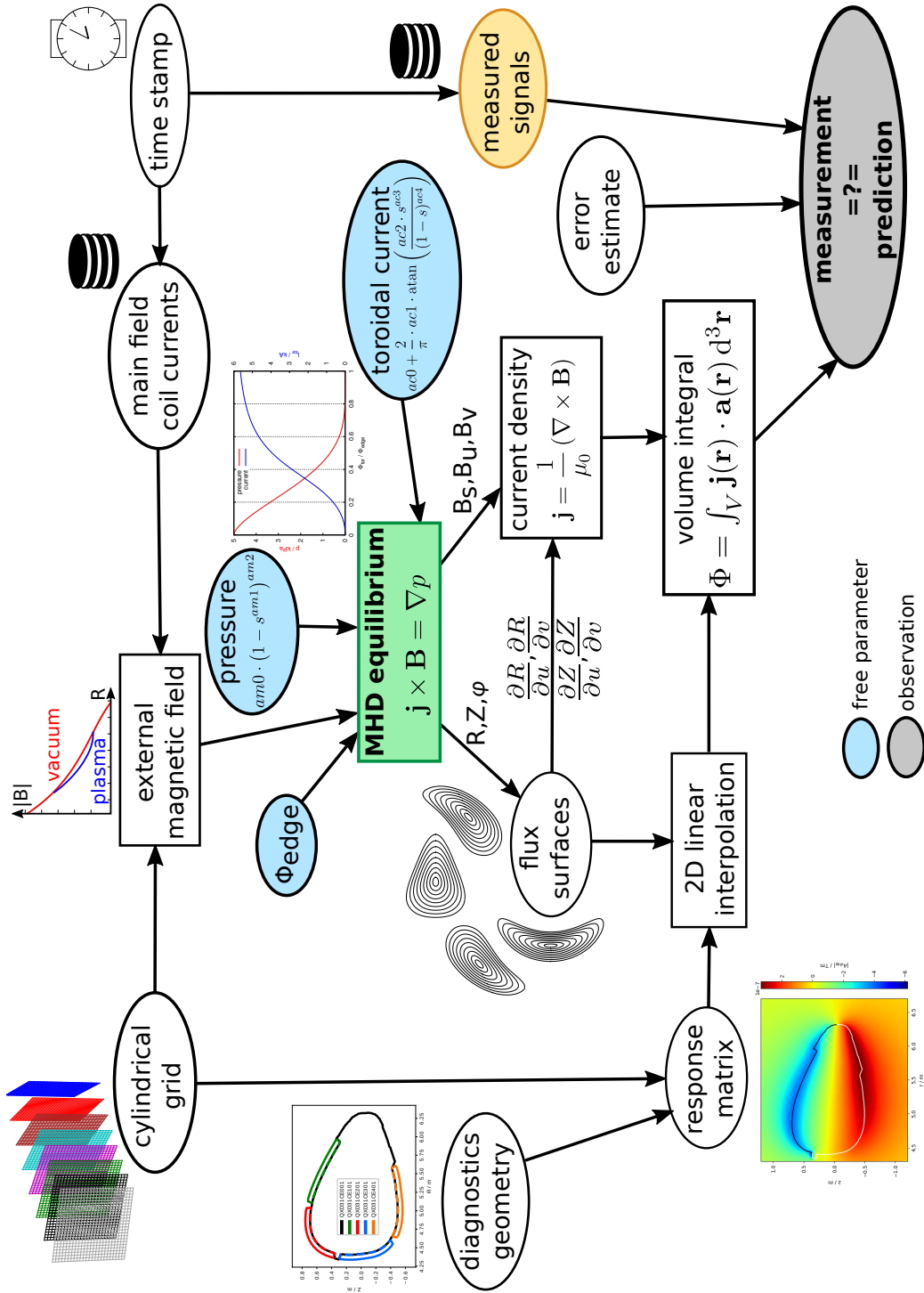


Fig. 27: Schematic overview over the involved quantities and computational steps used to predict the magnetic diagnostics signals for a given magnetic field, enclosed toroidal magnetic flux, pressure profile and toroidal current profile.

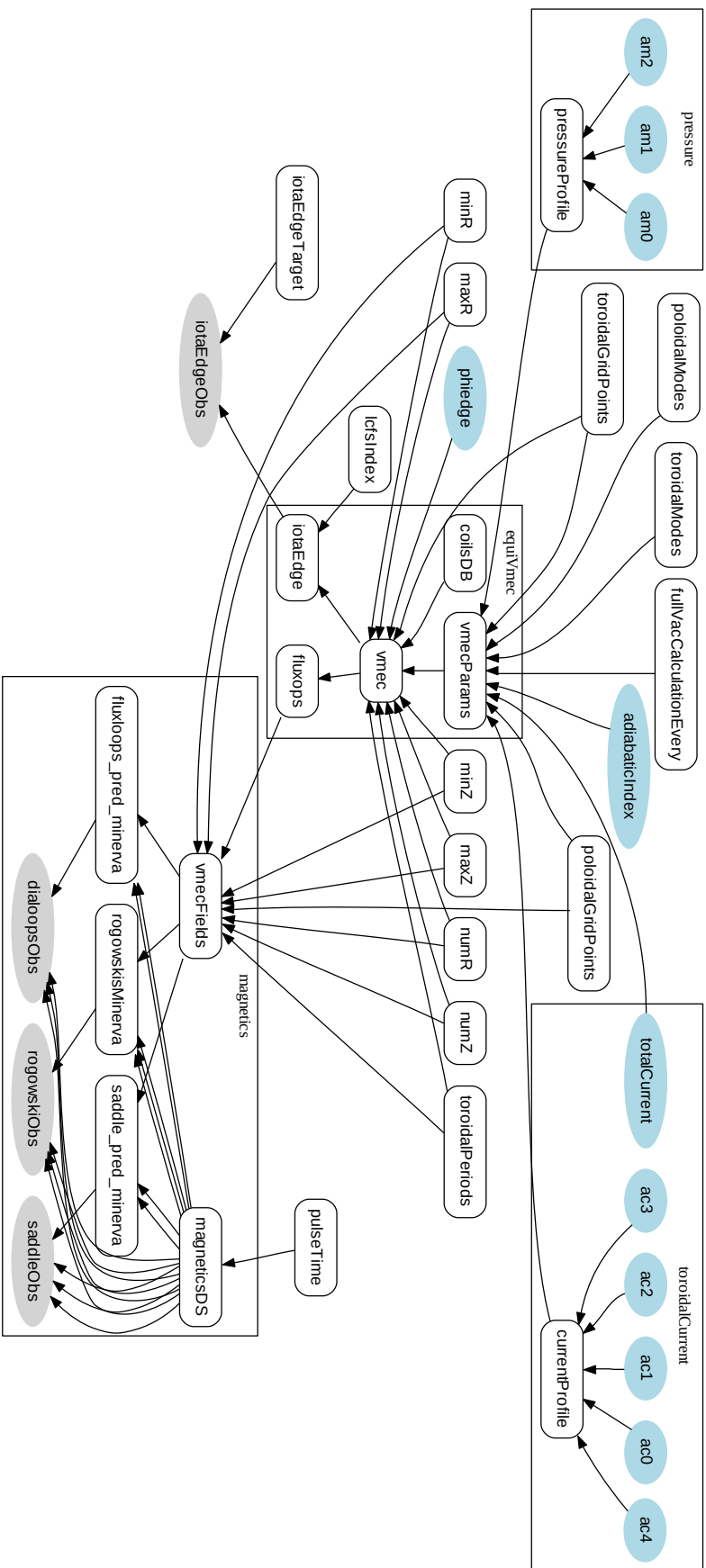


Fig. 28: Auto-generated graphical representation of the node structure used to describe the Bayesian Graphical Model for the problem sketched out in Fig. 27 within the Minerva framework. Note the additional virtual observation node for the rotational transform at the LCFS. A list of explanations for each artifact on this graph can be found in Appendix B.

## 4. Results

In this chapter, experimental and numerical results will be presented, which have been acquired during this work. Experimental results presented will be experiment program “20171108.40” from the experimental campaign OP1.2a of W7-X. Numerical results include the verification and validation as described in the previous chapter as well as the reconstruction results for the named experimental program.

## 4.1. Numerical Verification and Validation

Results from numerical verification and validation are presented in this section. This includes testing the self-consistency of modules implemented for computing the magnetic flux density and vector potential of filamentary wire segments, magnetic diagnostic calibration experiments and checking the intermediate results in computation of the response prediction for the magnetic diagnostics.

### 4.1.1. Magnetic Field and Vector Potential of Filamentary Wire Segments

First, the method to compute the magnetic field and vector potential for a single straight wire segment energized by a unit current is tested. The geometry for this test is shown in Fig. 17. For positions  $(x, y, z) = (\sqrt{5}, y, 0)$  with  $y \rightarrow 0$ , the vector potential is computed using the analytical expressions from Ref. [32] and compared to the results from the implementation available within the Minerva framework.

Two different implementations of the formula from the reference in terms of the order of evaluation of the involved terms in the code were used to test the implementation for stability against roundoff errors. The results from this comparison are shown in Fig. 29. As one can see, the new implementation solves the convergence problems of the old implementation available in the Minerva framework to machine precision for the range  $y \leq 1$  m. As the resulting error dependence on the  $y$  coordinate matches the deviation prediction in the reference, it can be concluded that the available implementation for computing the vector potential of filamentary wire segments suffers from the same convergence problems as described in the reference. The described analytical expression was therefore implemented in the Minerva framework and tested again for convergence. For  $y > 1$  m, the new implementation after the reference still did show finite differences to the analytical result. By reformulation of Eq. 38 into

$$\mathbf{A}(\mathbf{r}) = \frac{\mu_0 I}{4\pi} \hat{\mathbf{e}} [\ln(R_i + R_f + L) - \ln(R_i + R_f - L)] \quad , \quad (69)$$

good convergence was established for all values of  $y$ . These final results are marked “Impl. J.S.” in Fig. 29. The significance of this is underlined by the top panel in the figure, where a histogram of the values  $y$  occurring during the response potential computation for a diamagnetic loop in W7-X is shown. The largest part of the contributions comes from evaluations, where good convergence was already achieved in the old implementation. The upper limit of the histogram values corresponds approximately to the diameter of W7-X, referencing contributions to the diamagnetic loop signal from current density values at the other end of the machine. Points, where a match between the analytical and the numerical results was achieved to roundoff accuracy, normally would not show up on a logarithmic scale, because  $\log(0) = -\infty$ . Instead, these values are indicated by a solid line at the bottom of the plot.

The results of the analytical fluxloop test as outlined in Sec. 3.2.2 are presented in Fig. 30. A circular wire loop with a radius  $r_1 = 1$  m is energized by a unit current of 1 A. A fluxloop with variable radius  $r_2$  is located concentrically and in the same plane as the wire loop. Both loops are defined as polygons with a variable number of corners. The predicted value for the magnetic flux picked up by the fluxloop is computed by performing a line integral along the path of the fluxloop over the vector potential  $\mathbf{A}(\mathbf{r})$  due to the current in the wire loop and compared to the prediction by Eq. (40).

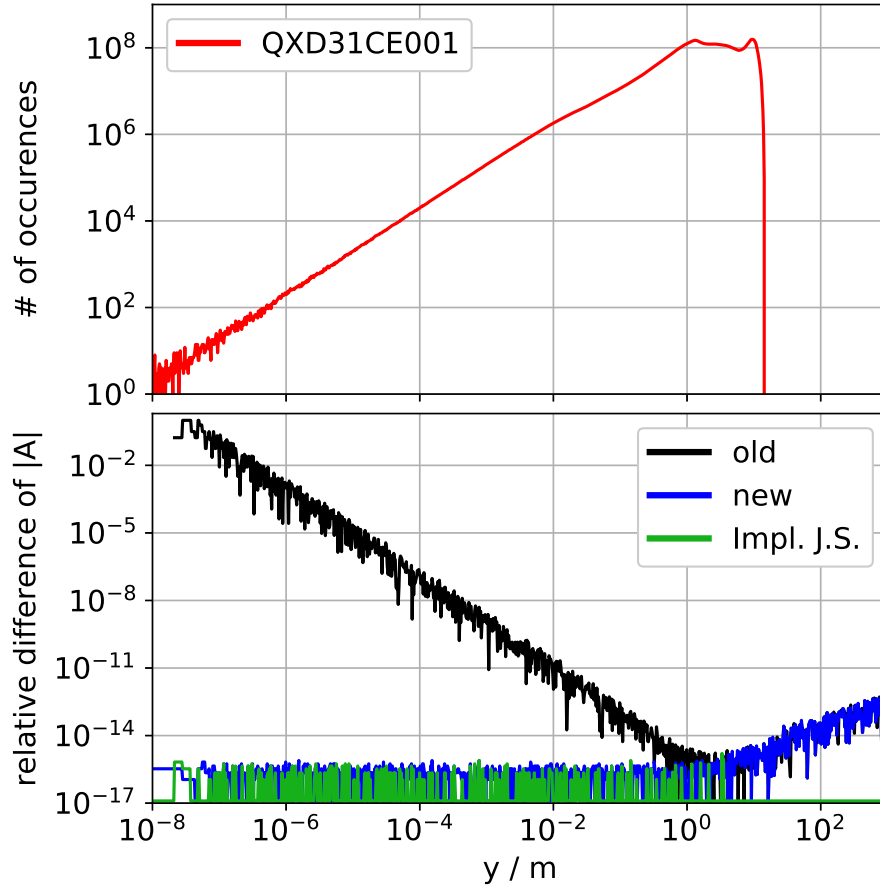


Fig. 29: The top plot in red is a histogram of the occurrence of values  $y$  during computation of the response potential calculation for a diamagnetic loop in W7-X. In the lower half of the plot, relative differences with respect to the analytical result of Eq. (38) are shown for the implementation in the Minerva framework available at the start of this thesis (black), the implementation as used in the V3FIT code (blue) and my implementation (green), reducing the deviation towards larger values of  $y$ .

Logarithmic convergence of the prediction when increasing the number of polygon corner points is observed, which is an indicator for a numerically robust computational scheme. As expected, for very small radii of the fluxloop, the captured flux vanishes as the cross section area vanishes as well. For radii close to the radius of the incidental wire loop, which is 1 m, the captured flux shows a peak and would diverge for an exact match due to the singularity in the vector potential computation routine when evaluated exactly on the wire segment. Therefore, this radius value is left out of the plot. For much larger fluxloops than the wire loop, the captured flux decays again.

To get a convergence estimate for the total problem, the errors were summed up for the shown fluxloop radii and plotted in the bottom panel of Fig. 30 for an increasing number of polygon segments of the wire loop and the fluxloop. Logarithmic convergence can be observed, although the residual summed errors are still several orders of magnitude larger than the numerical roundoff accuracy.

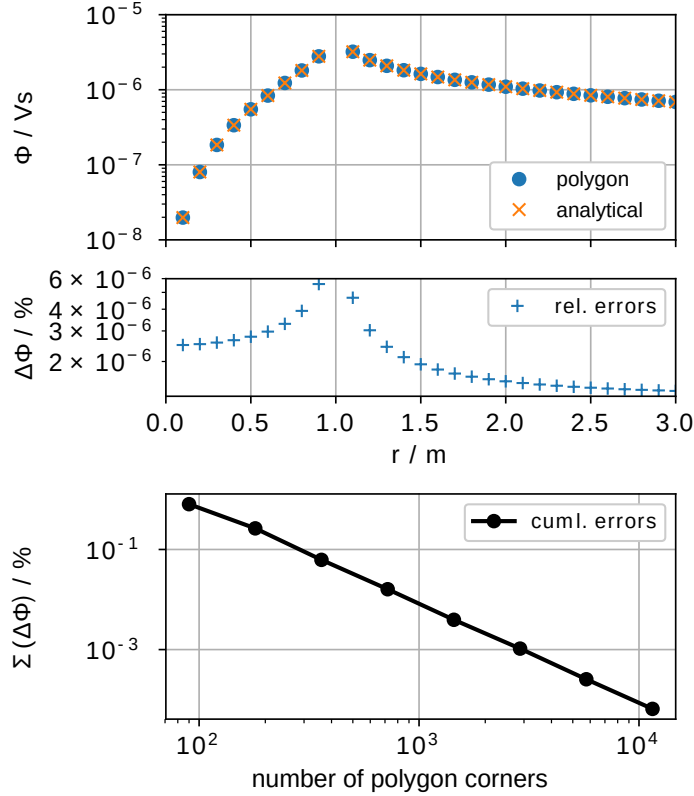


Fig. 30: Magnetic flux picked up by the fluxloop is shown in the top panel as computed by the analytical formula (40) and by the polygon filament approach. In the center panel, relative deviations between the two results are shown. The development of the sum of the deviations shown in the center panel, when the number of polygon corners is increased, is shown in the bottom panel. A similar convergence test was performed for the DIAGNO code [42].

#### 4.1.2. Magnetic Diagnostics Calibration Experiments

A typical trim coil current ramp shape can be found in Fig. 31, which is used to perform calibrations of the magnetic diagnostics.

A least-squares fit of Eq. (66) with  $t_0$ ,  $\tau$  and  $I_0$  as free parameters is performed on the difference signal between measurements and predictions for no eddy currents. Previous calculations [43] predicted time constants of  $\tau \approx 27.4$  ms for the plasma vessel. The trim coils are located outside of the cryostat, so a large metal barrier is added on top of the plasma vessel. This explains the much longer time constant inferred here, which is  $\tau = (0.16 \pm 0.01)$  s.

The validation results of the pickup coil signal predictions for all magnetic diagnostics of W7-X available during OP1.2a as computed by the routines listed above is shown in Fig. 32. The measured signals are better predicted for the diagnostics in the vicinity of the active trim coil, and errors increase on average with the distance to the active trim coil.

For the measurements during the coil current ramps in the neutron counter calibration rail, a situation similar to the trim coil ramps exists, i.e. the measurement period is short enough to fit inside an acquisition window of the magnetic diagnostics. However, no independent time-resolved current measurement exists for the rail current. Measurements

have been made using a current clamp and a digital multimeter as well as an oscilloscope, but no time traces of a rail current measurement were saved during this calibration to the W7-X data archive.

However, if one Rogowski coil is believed to provide accurate results, all other magnetic diagnostics can be checked against this Rogowski coil. One of the closed Rogowski coils has been chosen as the reference Rogowski coil, since it completely covers the plasma vessel poloidal cross section. The idea is then to “measure” the rail current by means of the selected closed Rogowski signal and compute the predictions for each of the other magnetic diagnostic coils based on this rail current measurement. The steady-state current during a flat-top phase of the rail current was specified, so this value can be compared for the reference Rogowski coil. For each of the experiments under investigation, the match between the reconstructed rail current and its specified value is within the expected error margins. A detailed comparison between each of the diagnostic predictions and the measured values is shown in Fig. 33.

The magnetic diagnostics do not measure during the whole procedure of ramping up the main magnetic field, conducting experiments and ramping the magnetic field down to zero. For the main coil current ramps, which occur at start and end of every experiment day, the magnetic diagnostics measured for a few seconds before the start of the ramp and for a few seconds in the middle of the ramp<sup>5</sup>. By design of the pre-evaluation routines, as described in Sec. 3.1.3, the first and the last datapoint of the integrated magnetic flux signal are forced to zero by means of the `wo` correction routine. This gives correct results in the case of a constant magnetic field, as in the periods in between experiment days as well as for the flat-top phases of the main magnetic field during an experiment day. However, measurements of parts of the main field coil ramps are inherently biased by the ramp slope. This, in the context of calibration experiments, valid signal would be destroyed by applying the usual pre-evaluation routines used in the normal experiment schedule.

The acquisition period before the start of the current ramp is used to estimate the momentary drift rate of the digital integrator, e.g. due to thermovoltages in the measurement setup, which cannot be corrected for by chopping the input signal. The idling drift rate of the digital integrator has proven to be stable enough that it is possible to use drift measurements acquired previously to actual measurements for the `wo` correction and still get good compensation of the drift errors. The idle measurement values are linearly interpolated to the timebase of the coil current ramp measurements to allow subtraction of the idle signal from the ramp signal and thus computation of the *drift-corrected signal*. This drift-corrected signal is then subsequently compared to the prediction. In case of the diamagnetic loop and its compensation loops, these measurements during the main coil current ramps are used to find the compensation factor used in the diamagnetic energy approximation [28].

---

<sup>5</sup>This is governed by the fact that the magnetic diagnostics can only save data in an intermediate buffer of about 30s acquisition time, before data has to be written to the internal harddisk of the acquisition device. Therefore, continuous acquisition over a whole experiment day, i.e. including the main field coil ramps, is currently not possible.

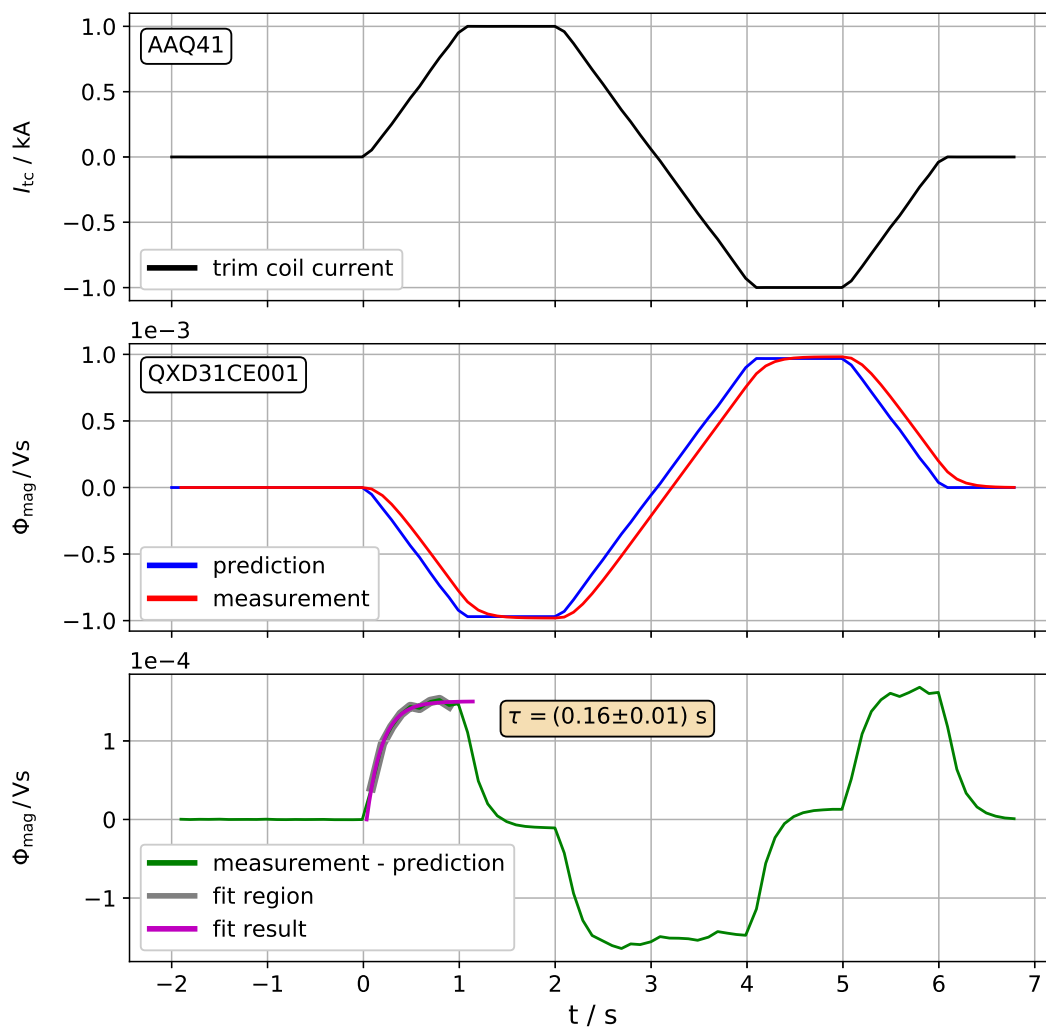


Fig. 31: A typical current ramp in trim coil AAQ41 as used for calibration of the magnetic diagnostics. The top panel shows the timetrace of the trim coil current (black). In the center panel, the measured magnetic flux of a diamagnetic loop (red) as well as the corresponding prediction (blue), if eddy currents are not taken into account, is shown. The deviation between prediction and measurement is plotted in the bottom panel in green. The model (66) is fitted to the grey shaded data region and the fit result is shown in magenta.

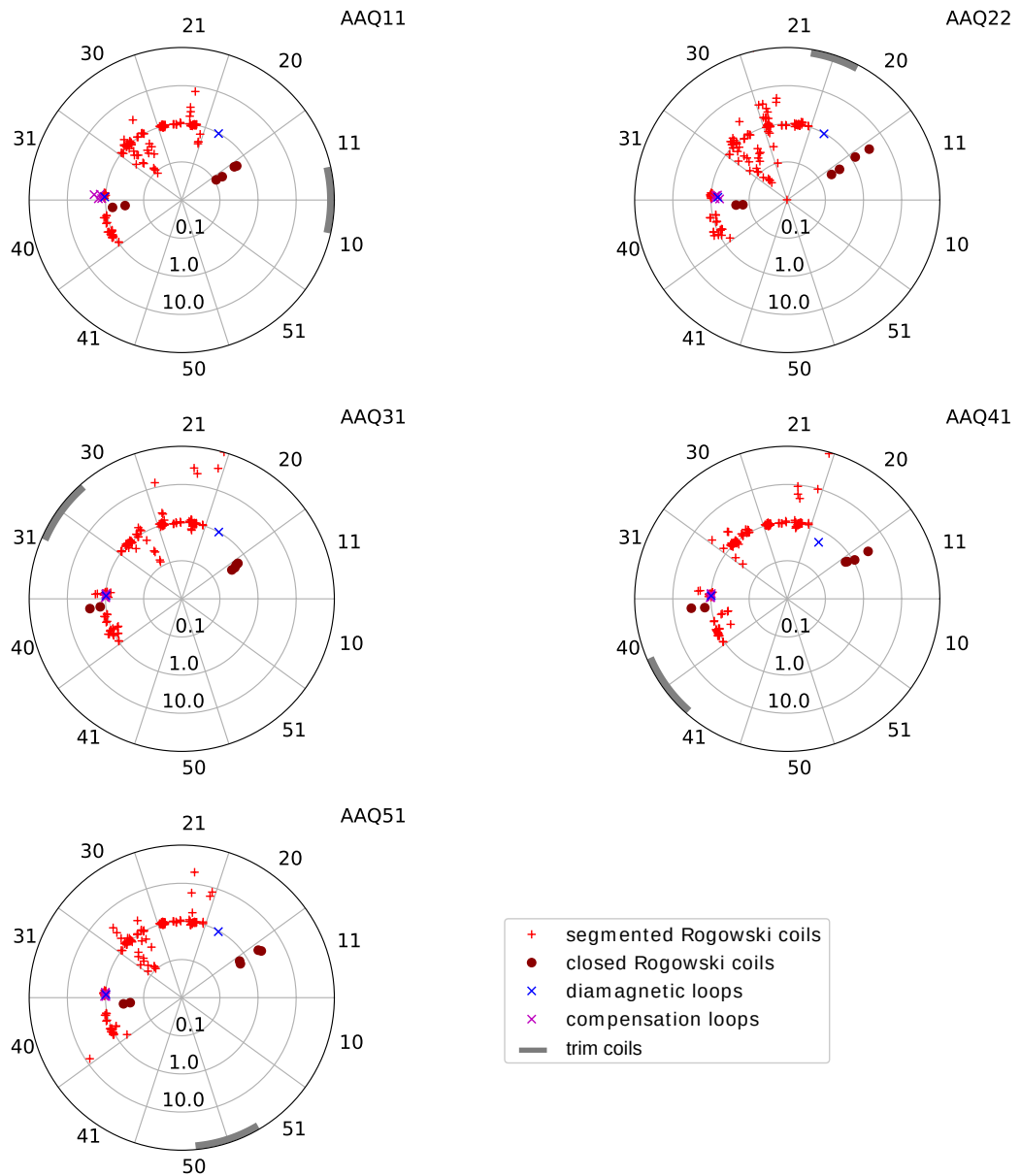


Fig. 32: Deviation of the predicted signals from the measured signals for a ramped current in each of the trim coils. The unit circle 1.0 denotes a perfect match between the predicted and the measured signal. Lower values (e.g. 0.1) indicate a too low prediction, whereas higher values (e.g. 10.0) indicate a too large prediction. The magnetic diagnostics signals are represented by blue crosses. The half-module identifiers are located around each plot. The toroidal location of the data indicators correspond to the center-of-mass of the corresponding diagnostic geometry. Grey lines at the boundaries indicate the trim coil extents. Saddle coils are left out for clarity.

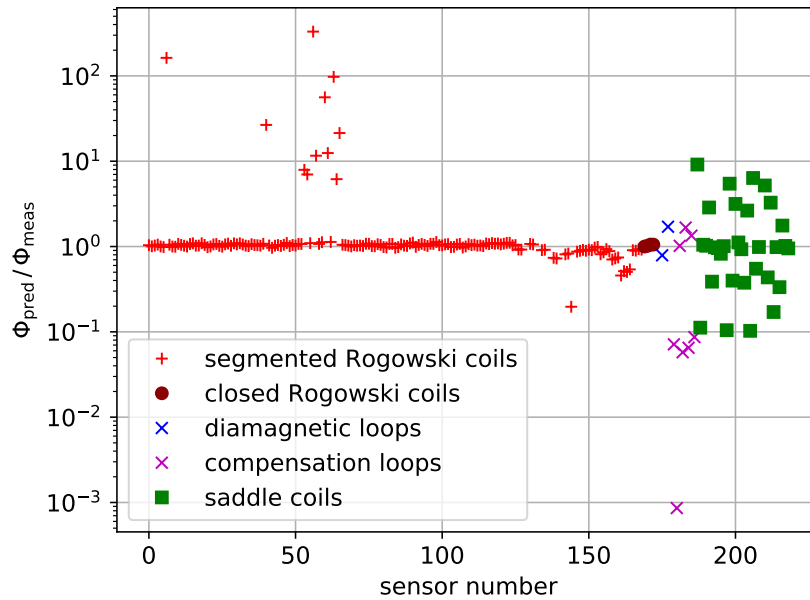


Fig. 33: Comparison between measured magnetic fluxes and predictions for the neutron counter calibration rail experiments. The Rogowski coil measurements (indices  $\leq 160$ ) mostly agree well with the predictions, diamagnetic loops as well (indices 161...170). The saddle coil signals (remaining indices) mostly disagree by a factor between 0.1 and 10.

### 4.1.3. Current Density from VMEC

The magnetic diagnostic measurement signals are the results from superposed signals that originate from two sources. One is the vacuum magnetic field, developed by the confining magnetic field coils and is described by the mutual inductances and coil currents as outlined in the previous section. The other contribution comes from currents inside the plasma [34]. The results from a computation of the current density from a VMEC MHD equilibrium are presented in here as well as a comparison to a reference implementation in the `BMW` code from Oak Ridge National Laboratory by M. Cianciosa [44]. The `BMW` code uses a two-step approach to compute a divergence-free magnetic field from the plasma current density. First, it computes the current density on the VMEC flux coordinate grid to allow computation of Biot-Savart volume integrals over the plasma volume. In a second step, the vector potential and the magnetic field are computed on a specified grid from the background magnetic field and the plasma current density. This is especially useful for verification of the current density computation in Minerva, since the methods implemented in the `BMW` code are the same as the ones needed for computation of the magnetic diagnostic predictions.

For the purposes of this work, the `BMW` code has been modified to also output the current density, which is normally only available inside the allocated memory for the code's runtime. A comparison of the current density computation as available from `BMW` and from my implementation in the Minerva framework is depicted in Fig. 34.

As indicated in the right column of the figure, excellent agreement is found between the current density calculation methods implemented in the `BMW` code and my implementation in the Minerva framework. However, in the core region of the plasma, numerical artifacts show up as strong dipolar structures. These introduce additional signals in the response calculation for the magnetic diagnostics. This is a known issue to the developers of both VMEC and `BMW`. The current solution is to subtract the current density from a “fingerprint” VMEC calculation. For a given VMEC calculation, the net toroidal current is set to zero and the pressure profile is set to a minimum value to ensure convergence of the code. Then, for all other parameters left unchanged, a VMEC equilibrium is computed. The resulting current density components are subtracted from the ones in the original VMEC calculation output prior to calculation of the magnetic diagnostic response predictions [45]. For the purposes of equilibrium reconstructions, this scheme showed sufficient accuracy so far.

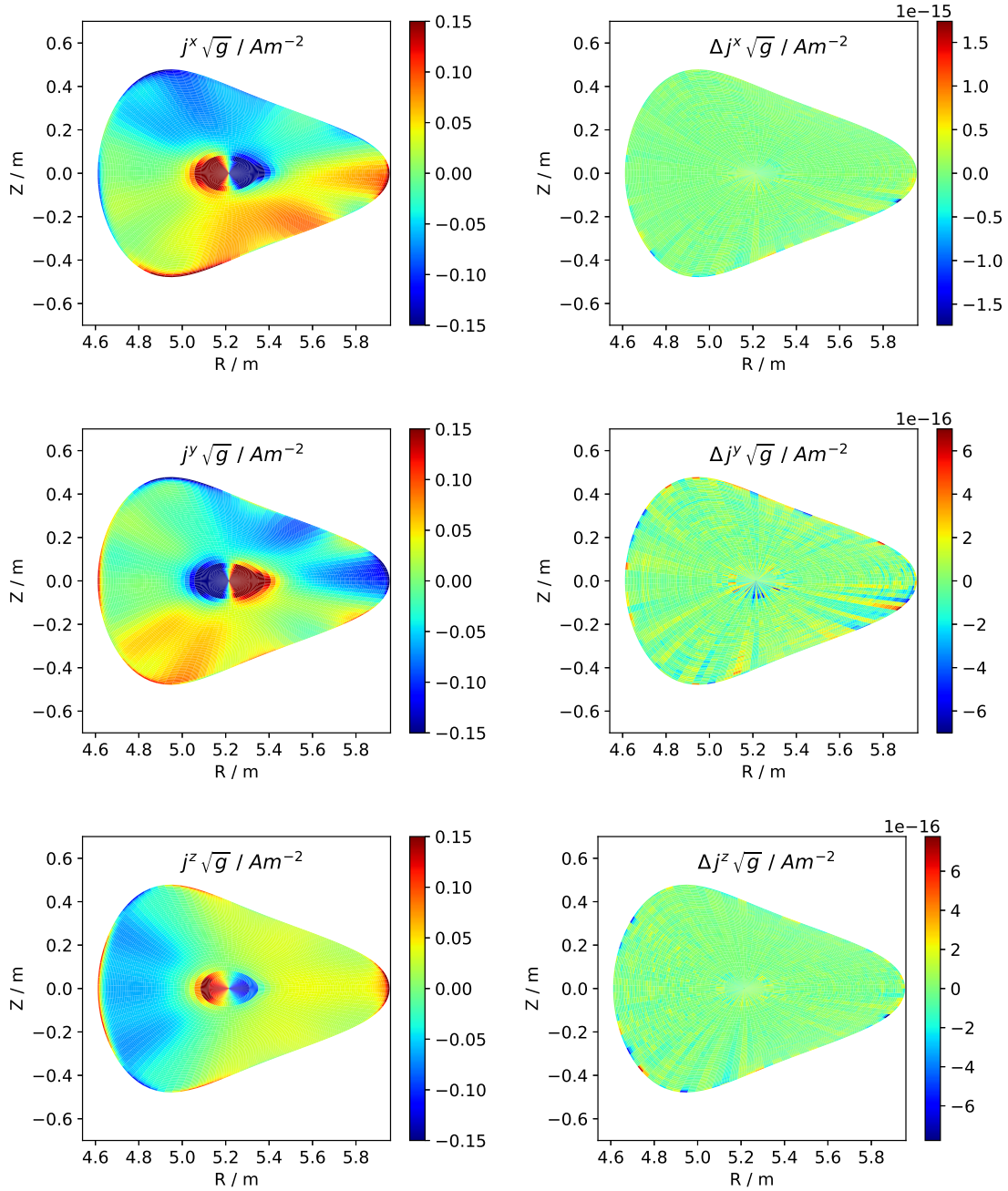


Fig. 34: From top to bottom,  $j^x \sqrt{g}$ ,  $j^y \sqrt{g}$  and  $j^z \sqrt{g}$  are plotted ( $\langle \beta \rangle = 5\%$  and  $I_{\text{tor}} = 5\text{kA}$ ). The left column shows the values computed by my implementation in the Minerva framework. On the right, absolute differences to the BMW code are plotted.

#### 4.1.4. Response Matrix Verification

For the geometry of a diamagnetic loop, the vector potential of a unit current density along the geometrical path of the diagnostic coil is computed on a cylindrical grid on the VMEC toroidal cutplanes. The toroidal component of the vector potential in the cutplane, where the diamagnetic loops crosses through, is shown in Fig. 35. The response potential

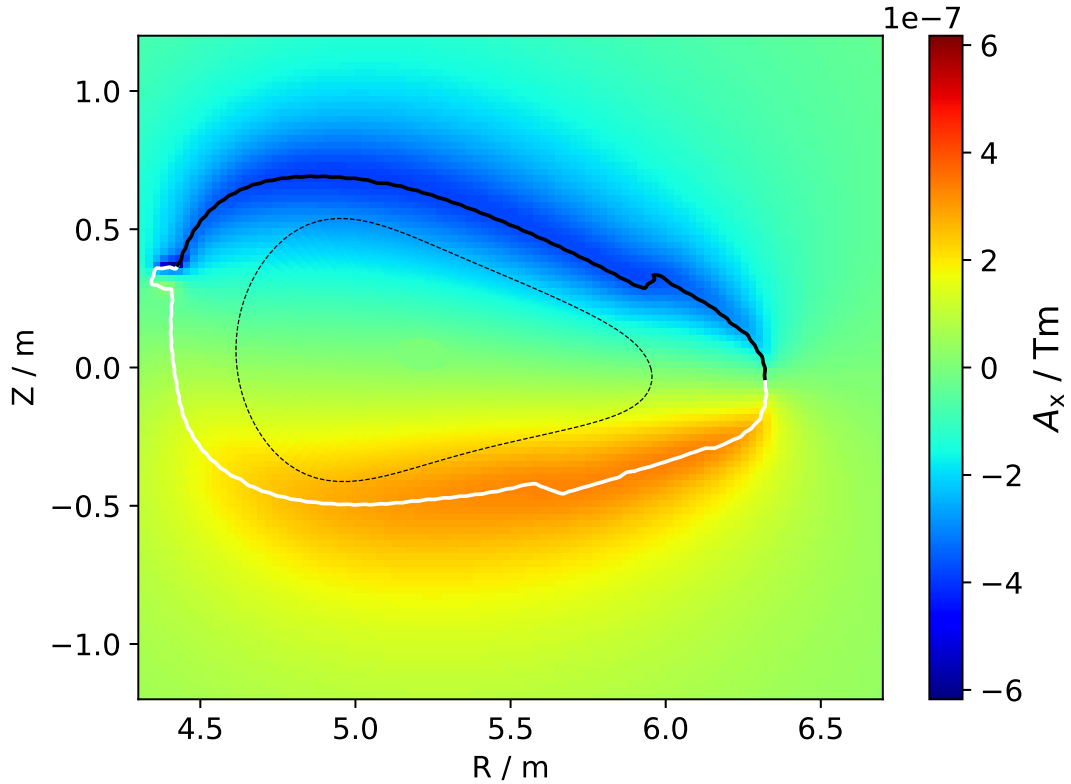


Fig. 35: The response factors for the diamagnetic loop in the triangular-shaped plane is shown here. The diamagnetic loop is tilted by a few degrees to follow the local magnetic field geometry. A change in the sign of the response factors is evident for the parts of the loop that are penetrating through the (vertically aligned) toroidal cutplane. Parts of the loop on the viewer's side of the cutplane are indicated in white, whereas black parts are located behind the cutplane.

changes its sign, as the loop crosses through the cutplane, since the loop is slightly tilted. The region inside the fine dashed line in the figure corresponds to the VMEC domain cross section. Values inside this region have been interpolated from the rectangular grid used to plot the values in the background onto the flux grid locations according to the procedure demonstrated in Fig. 19. No singularities of the response potential are present inside the VMEC flux surface geometry domain.

By taking toroidal and stellarator symmetry of the current density into account, the integrals (47) and (54) can be reduced in the toroidal direction to one half-module. The response potential have to be summed up respectively, so that all information on the whole machine circumference is stored on the corresponding grid locations in the first half-module.

The compressed response potential, as shown in Fig. 36, contains a maximum of the response value at the toroidal loop position, which is determined by the relative location of the diamagnetic loop with respect to the half-module that contains the loop. The local response from that half-module is mirrored and rotated into the only half-module (11), which is stored for further use in the reconstruction process.

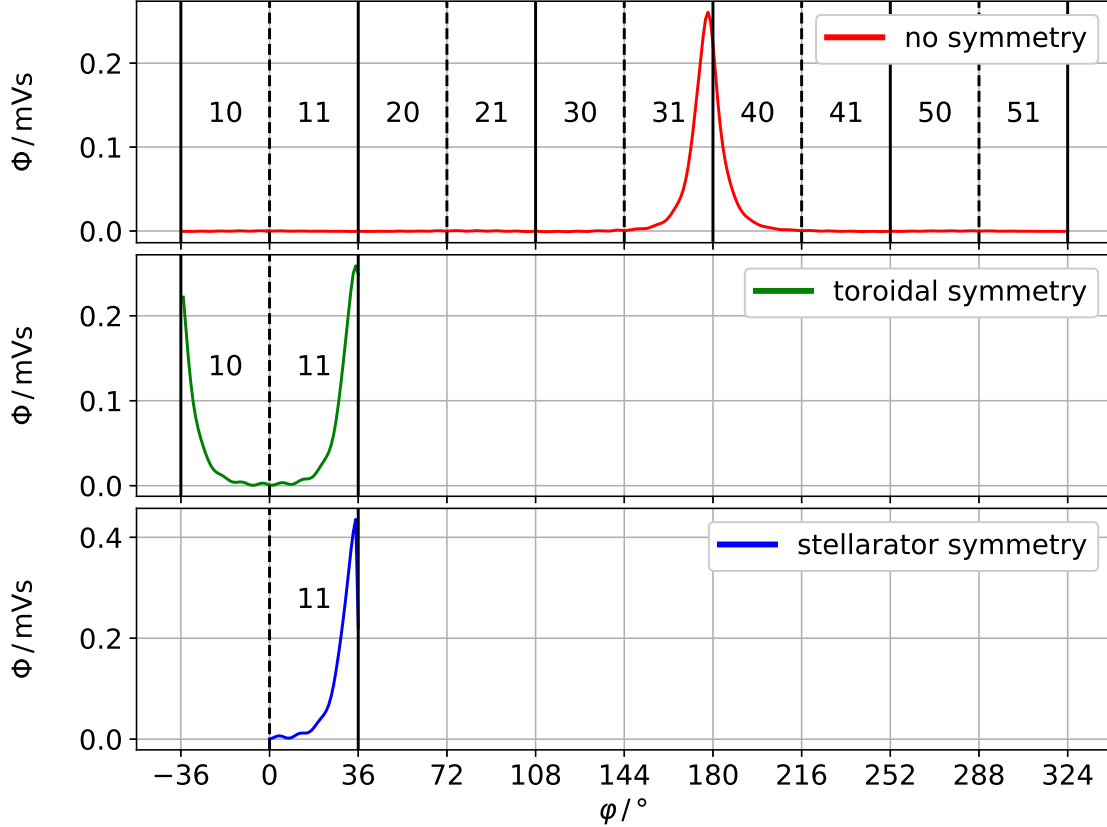


Fig. 36: The individual contributions from different toroidal positions to the predicted fluxloop signal for the diamagnetic loop QXD31CE001 are shown here. The contributions are largest for cutplanes closest to the toroidal position of the loop. Here, this is evident from the peak at  $\varphi = 178^\circ$  in the top panel. The center panel shows an intermedia result, when the response potential is summed up by taking toroidal symmetry into account. The end result, a complete response potential taking stellarator and toroidal symmetry into account, is shown in the bottom panel.

#### 4.1.5. Magnetic Diagnostics Prediction in Comparison With Other Codes

After verification against analytical magnetostatics problems, the newly implemented magnetic diagnostics prediction code in the Minerva framework had to be compared to existing codes. Among these, the DIAGNO code [42] is well tested and regularly used within the STELLOPT package [46]. Instead of computing a volume integral over the current density inside the plasma, a virtual casing principle [47] is applied by computing a surface integral over a surface current on the LCFS.

The V3FIT code [16] can be configured to run in several modes of operation, where one named V3POST is used to compute the predicted values for the diagnostics. The magnetic diagnostics prediction code in the Minerva framework uses the same principle of computation as the V3POST code. Therefore, the predicted signals computed in the Minerva framework were as well compared to the V3POST predicted signals for the magnetic diagnostics.

The predictions computed by the DIAGNO code are taken as reference values here, since it uses an adaptive integration technique to compute the Biot-Savart integrals over the surface current on the LCFS, leading to better convergence.

Fig. 37 shows the resulting predictions as computed using the volume integral and the virtual casing methods just mentioned for a  $\langle\beta\rangle \approx 1\%$ ,  $I_{\text{tor}} \approx 6$  kA VMEC calculation. Overall agreement between the two methods is reasonable. The results from the V3POST code are left out for clarity, as they show spot-on correspondence to the results obtained by my implementation in the Minerva framework.

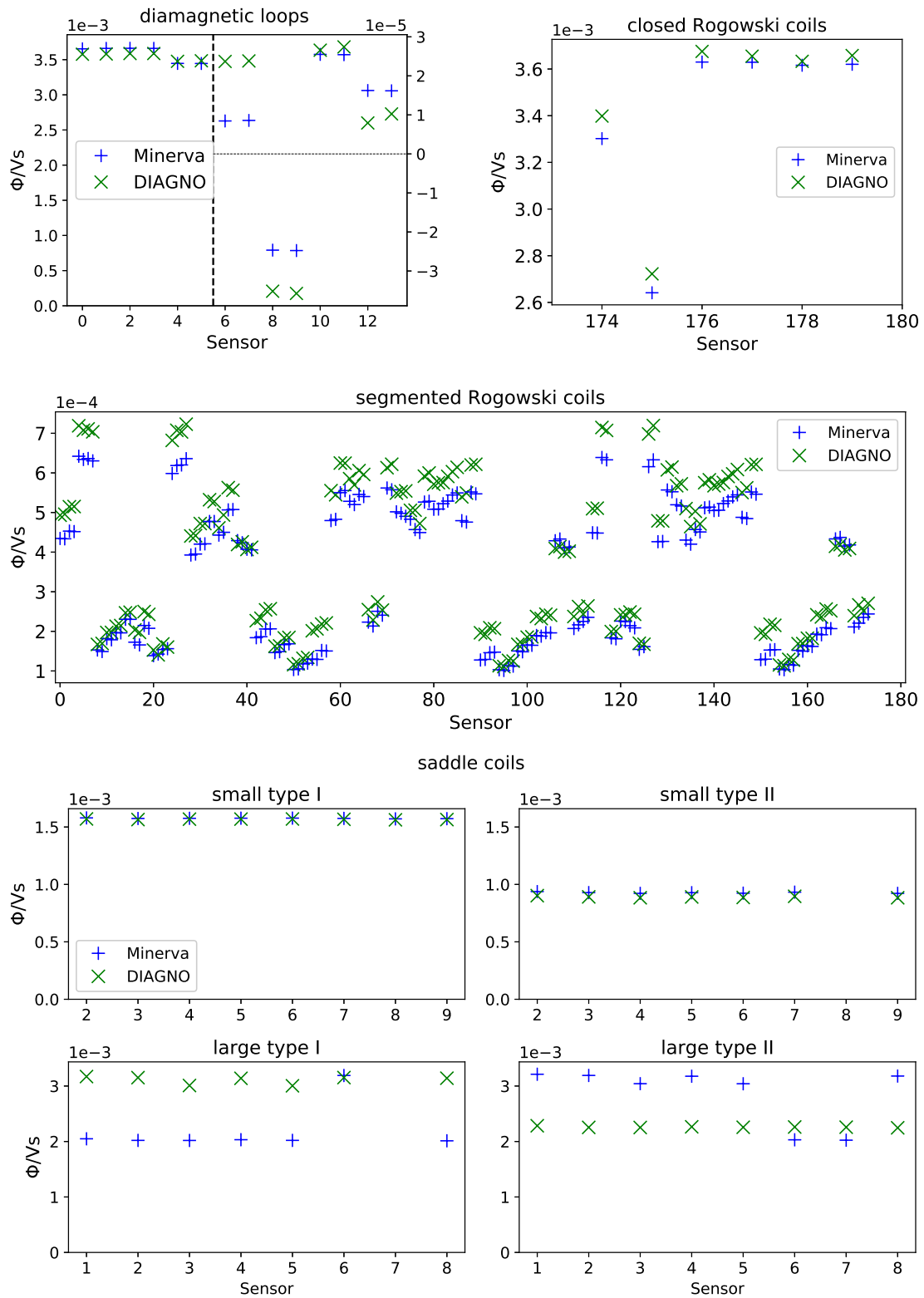


Fig. 37: Comparison of the prediction results for the magnetic diagnostics between my implementation in Minerva and the DIAGNO code for an equilibrium with  $\langle\beta\rangle \approx 1\%$  and  $I_{\text{tor}} \approx 6$  kA.

## 4.2. Plasma Reconstructions

For the experiment program 20171108.40 featuring a quiescent plasma, MHD equilibrium reconstructions are presented in this section. This experiment program is introduced briefly. Next, a scan over the free parameters available in the reconstruction model has been performed. The combination of free parameter values, which produced the best fit to the measured data, is selected as starting point for an automatized inversion routine. Addition of a constraint on the rotational transform at the LCFS significantly improved the first reconstruction results. Finally, the reconstruction output is presented in some details.

### 4.2.1. Reference Experiment Program

For a first reconstruction using the methods developed in this master thesis, an experiment program was chosen, where the plasma behaved relatively quiescent. Fast plasma dynamics often involve eddy currents in the plasma vessel due to fast changes in the plasma currents. Since eddy currents are currently not modeled in the reconstruction process, their influence on the magnetic diagnostic signals could not be accounted for and would lead to degraded results. An overview plot of quantities relevant for the reconstruction is shown in Fig. 38.

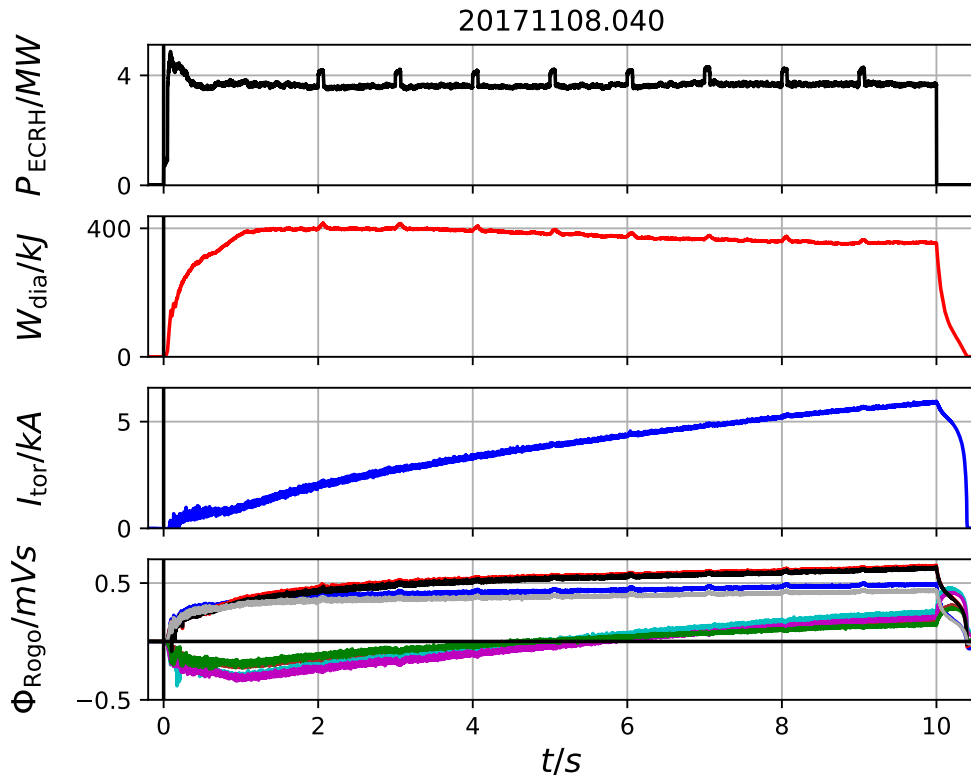


Fig. 38: Overview plot for the reference experiment program 20171108.40 used to test the reconstruction models. From top to bottom, heating power of the Electron Cyclotron Resonance Heating system, diamagnetic energy, toroidal current and magnetic fluxes of eight segmented Rogowski coils located in the triangular-shaped plane are shown.

The reconstruction is performed at  $t = 9.9$  s. There, the heating power is at  $P_{\text{ECRH}} \approx 3.9$  MW, resulting in a diamagnetic energy  $W_{\text{dia}} \approx 380$  kJ. The toroidal current  $I_{\text{tor}} \approx 6$  kA is still evolving. The timescale for the bootstrap current evolution is governed by the plasma inductance and its resistance. The inductance can be approximated by a circular wire loop of finite diameter [48]. Spitzer resistivity can be used to approximate the plasma resistance for a given temperature profile [7]. A typical value of the resulting timescales is on the order of several seconds for W7-X, consistent with the observation in the given experiment. Since this timescale is much slower than the timescale of eddy current evolution in the plasma vessel and the cryostat inferred in Sec. 4.1.1, this slow evolution of the toroidal current is neglected. The bottom plot in Fig. 38 shows the magnetic flux signals of eight segmented Rogowski coils in the triangular shaped plane. Four of the eight segmented Rogowski coils are located more on the inboard side of the plasma vessel (green, cyan, violet and brown traces), whereas the other four segmented Rogowski coils are located more on the outboard side (red, black, grey and blue traces). At the beginning ( $t \approx 1$  s), the dipolar-shaped Pfirsch-Schlüter currents dominate the magnetic diagnostic signal. This can be observed by negative magnetic flux signals of the inboard Rogowski coils, as compared to positive magnetic flux signals of the outboard Rogowski coils. As the bootstrap current evolves, a net toroidal current leads to a uniform shift in the positive direction of all of the segmented Rogowski coil signals.

#### 4.2.2. Scan of the Free Parameters

A reconstruction of the MHD equilibrium using the Minerva framework starts by scanning the values of a limited subset of the free parameters on the graph and recording the resulting posterior probability. An exemplary scan in the central pressure  $p_0$  and the net toroidal current  $I_{\text{tor}}$  is shown in Fig. 39. Each grid location stands for one VMEC computation and subsequent prediction of the magnetic diagnostics signals. The profile shapes of pressure and toroidal current were held fixed during this scan. The shapes of the profiles in use are shown in Fig. 26.

The ranges of the parameter scan values were chosen to approximately match the values that were encountered during the experiment program. Higher values for the posterior probability indicate a better match of the predictions to the measurements. As can be seen, a clear maximum exists in the scan. This corresponds to one set of values for the toroidal current and the central plasma pressure, which reproduces the magnetic diagnostic signals best. To further visualize the peak in the posterior probability distribution, slices through the maximum have been plotted next to the two-dimensional colormap to further illustrate the peak.

However, the scan raster is still too coarse to infer a reasonably accurate result for the reconstruction. Therefore, starting from the maximum found during the scan, automatized optimization by the Hooke and Jeeves algorithm is started to obtain an even better match of the predictions for the magnetic diagnostic signals to the measured values.

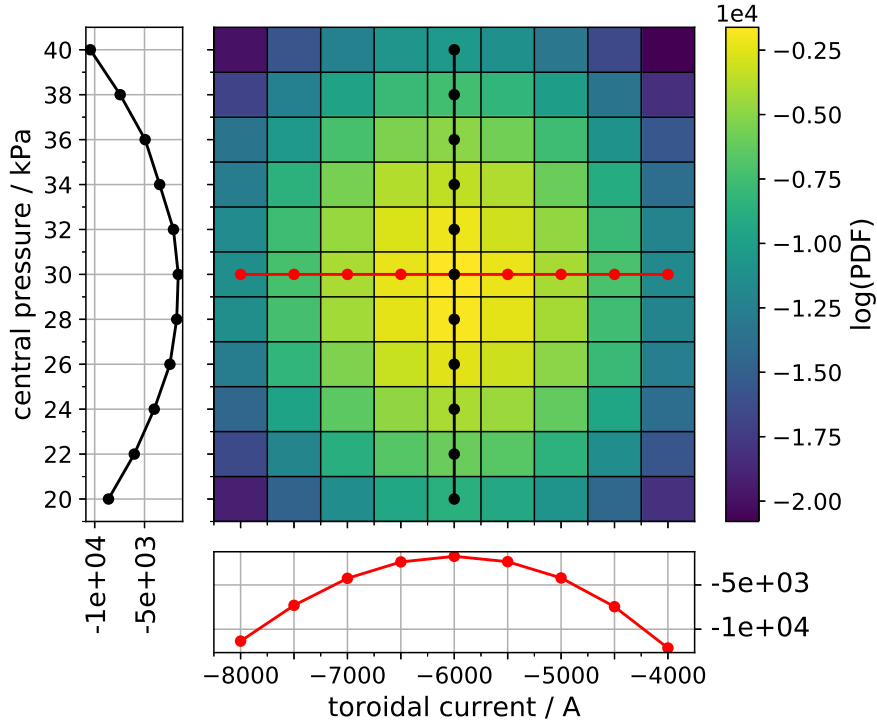


Fig. 39: Scan of central pressure  $p_0$  and toroidal current  $I_{\text{tor}}$  on the graph with all other parameters held fixed. Slices through the two-dimensional surface are shown in red and black. The colormap refers to the values of the logarithm of the posterior probability distribution. Higher values indicate a closer match between the measured signals and the predictions.

### 4.2.3. Maximum Posterior Inversion

An automated maximum search on the posterior probability distribution found in the scan of some free parameters, as shown in Fig. 39, is initiated in this step of the reconstruction. Here, another free parameter is activated and thus varied throughout the optimization. For the reconstructions presented in Fig. 40, this is the value of the enclosed toroidal magnetic flux  $\Phi_{\text{edge}}$ . The starting value of  $\Phi_{\text{edge}}$  was chosen manually to produce a good match to the signals measured by the segmented Rogowski coils for the first reconstruction. The goal is to find the set of free parameters on the graph, which leads to the best matching predictions for the measured values of the included diagnostics. It can be observed that the number of MAP iterations required to converge the model is significantly increased to about 100 iterations after addition of the constraint on the rotational transform value at the LCFS. The value of  $\Phi_{\text{edge}}$  started at about 1.5 V s and slowly increased to its final value of 1.8 V s. In parallel, the central pressure  $p_0$  and the toroidal current  $I_{\text{tor}}$  evolved as well. Here, approximately constant ratios between the values of these three free parameters can be seen.

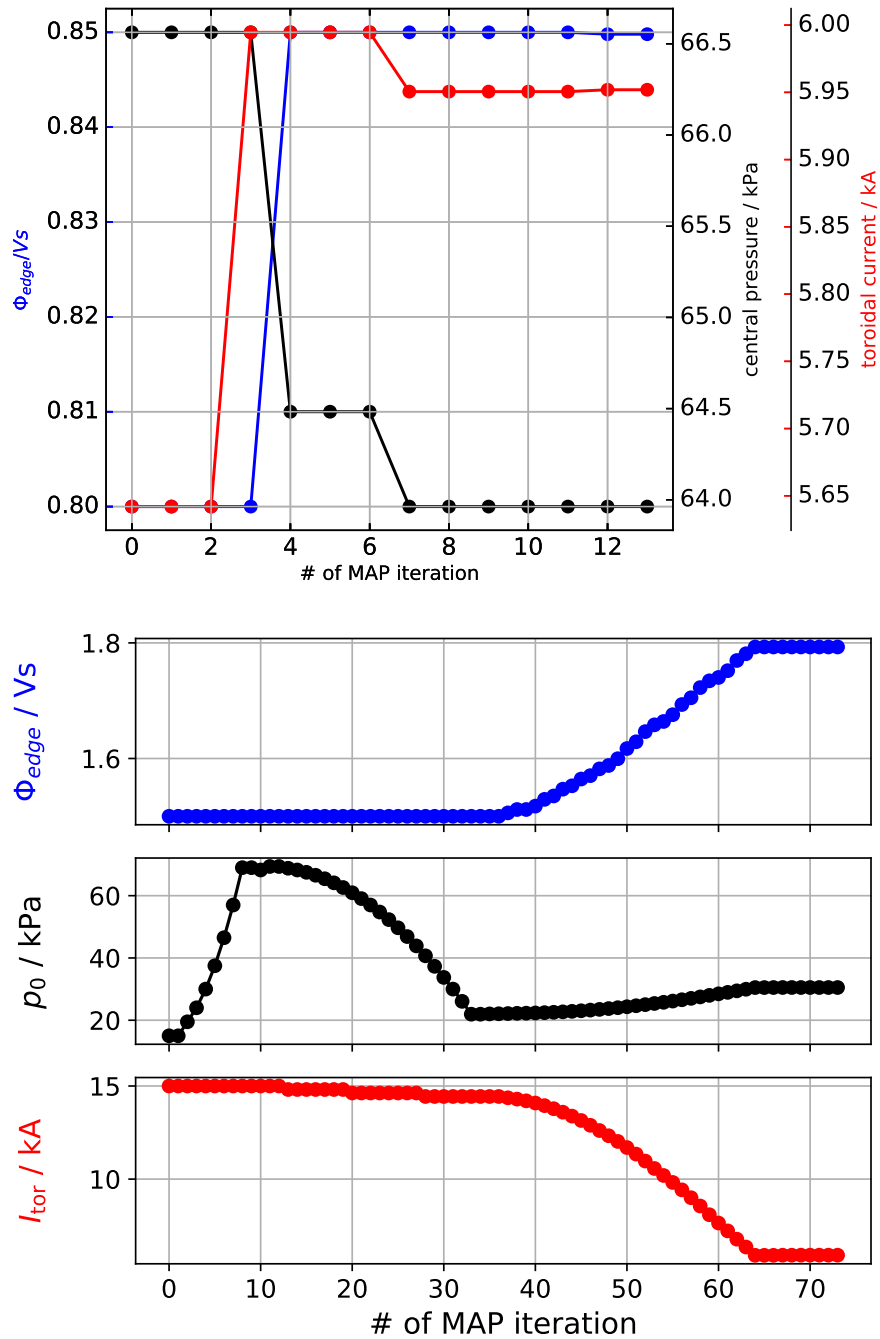


Fig. 40: MAP convergence for  $\Phi_{edge}$ , toroidal current  $I_{tor}$  and central pressure  $p_0$  as free parameters. The top panel illustrates the MAP convergence for the first reconstruction attempted. In the bottom panel, the MAP path after adding a virtual observation on the rotational transform at the LCFS is shown.

#### 4.2.4. Results of Reconstruction

In this section, results from the reconstruction runs shown in the previous section are presented. A first check on a reconstruction result is performed by a comparison between the flux surface geometry obtained in the reconstruction and the vacuum magnetic flux surfaces. For the first reconstruction, this is presented in Fig. 41. The reconstructed flux

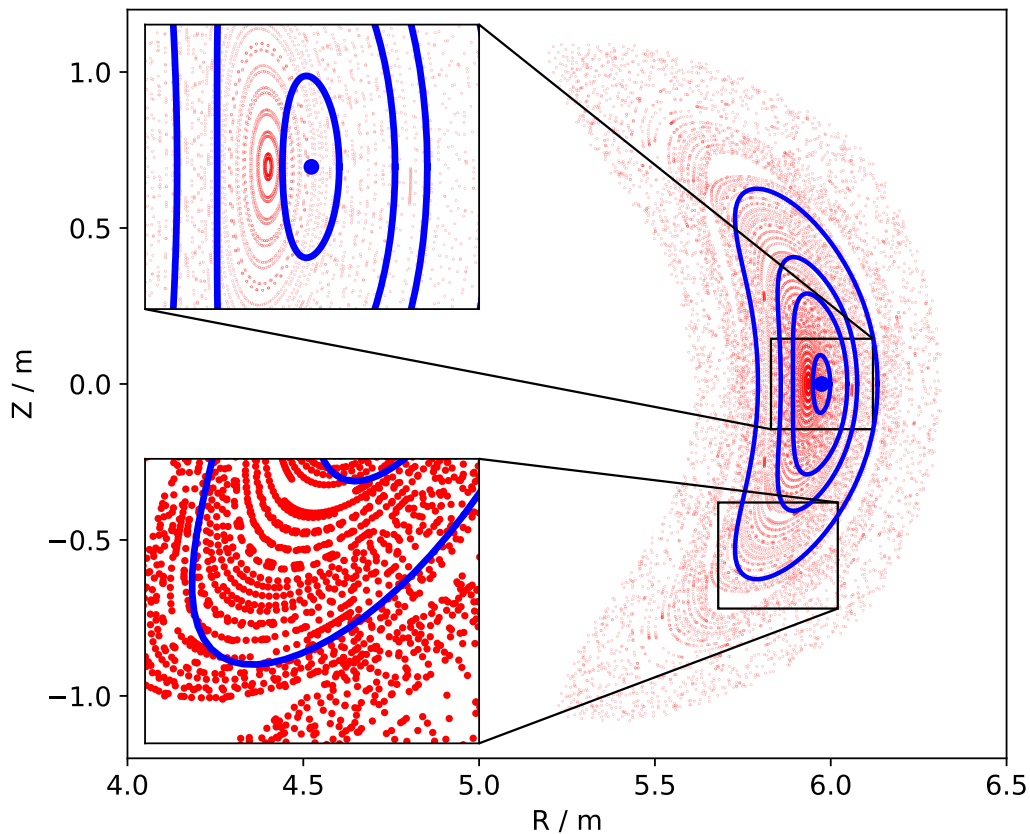


Fig. 41: Vacuum magnetic field line tracing Pointcaré map (red dots) and selected flux surfaces resulting from the first attempt of the reconstruction (blue). The vacuum magnetic island chain at  $\iota = 10/11$  is visible just outside of the reconstructed LCFS.

surfaces look similar to the vacuum magnetic field structure, but subtle differences are notable. In the top left inset, the plasma core region is examined in greater detail. Here, the Shafranov shift is directly visible as a radial outward directed shift of the magnetic axis with respect to the vacuum magnetic island. This result is expected, because the reconstruction revealed a normalized pressure  $\langle \beta \rangle \approx 1\%$ . However, the LCFS geometry does not fit well to the vacuum magnetic flux surface geometry. This is depicted in the lower left inset in Fig. 41. Additionally, the plasma volume is significantly too small. This is in contradiction to video camera observations of the island divertor target elements, where

heat loads due to contact to the magnetic islands were observed clearly. This would have not been the case, if the plasma size was equal to the reconstruction result shown here.

As mentioned above, addition of a constraint on  $\iota_{\text{edge}}$  improved the results. This is shown in Fig. 42. The LCFS now matches the vacuum magnetic flux surface geometry

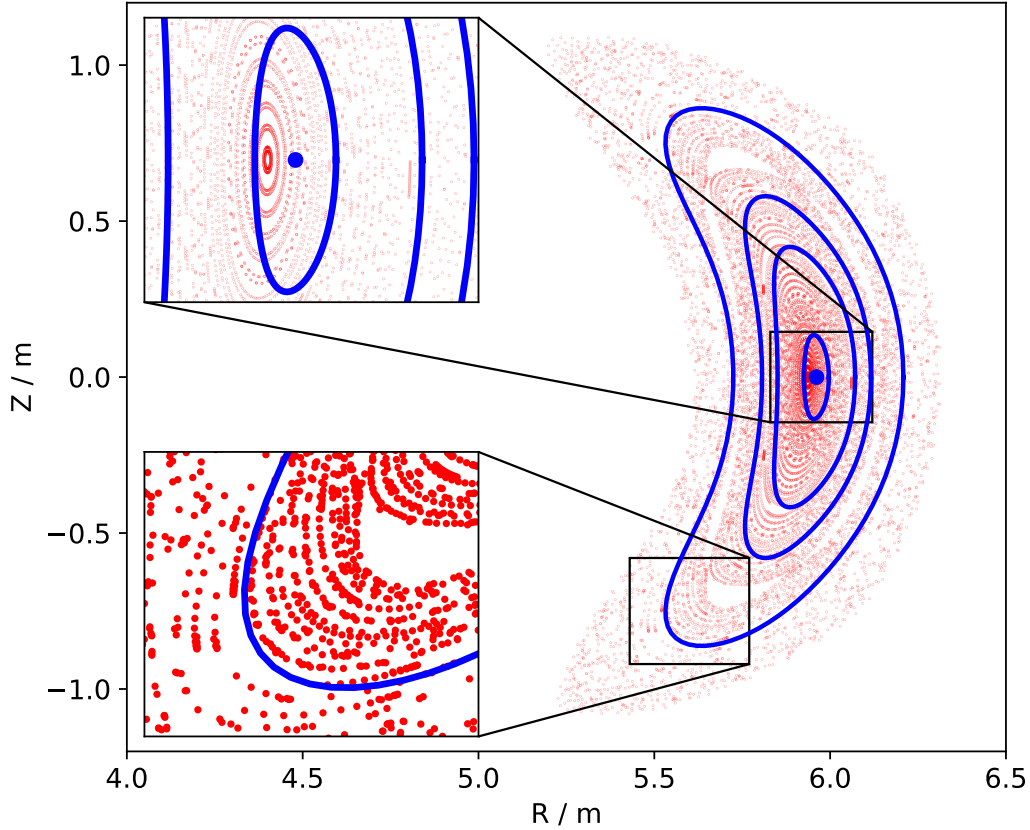


Fig. 42: Vacuum magnetic field line tracing Pointcaré map and flux surfaces of the improved reconstruction. The virtual observation on the  $\iota_{\text{edge}}$  value improved the fit of the LCFS shape to the vacuum magnetic field geometry significantly.

much better, as can be seen in the overview in the right hand side and especially in the lower left inset. Small deviations are still present. The Shafranov shift is equally well reproduced in the plasma core region as it was in the first attempt.

Given a reconstruction result, which matches the vacuum flux surface geometry to a satisfactory accuracy, further quantities in the reconstructed equilibrium can be investigated. A non-exhaustive subset of these is presented in Fig. 43. The pressure profile is shown in the top panel. A central pressure of  $p_0 \approx 27$  kPa is observed. The pressure profile shape was not optimized throughout the reconstruction process, but was adapted from reconstructions already performed using the STELLOPT suite [49]. The flux-surface averaged parallel current density is shown in the middle panel. No net current on the magnetic axis is present. As the direction of the current is anti-parallel to the confinement magnetic field, the values of the parallel current density are negative. The largest contributions originate

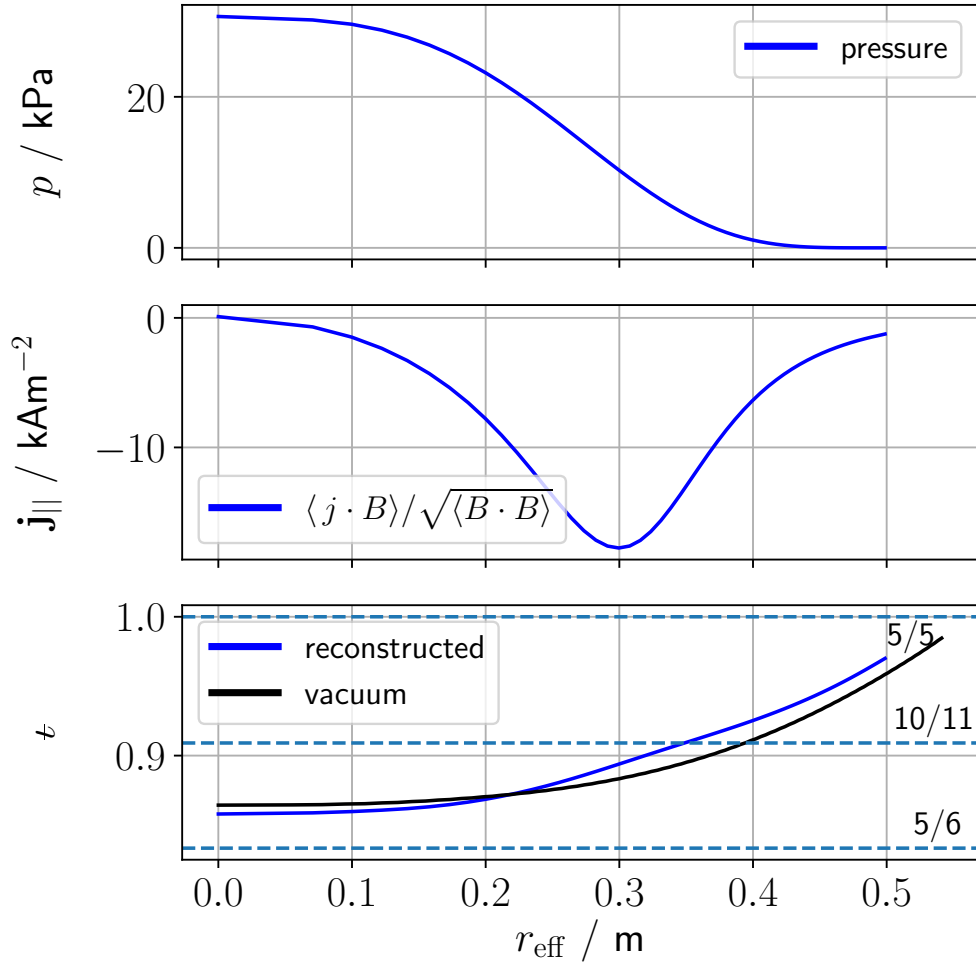


Fig. 43: Final reconstruction results. From top to bottom, the pressure profile, the flux surface averaged parallel current density and the rotational transform profile are shown. The  $\iota$  profile is compared against the vacuum rotational transform. Low-order rational values of  $\iota$  are indicated by blue dashed lines.

from radial locations at about half the minor radius. The radial profile of the rotational transform as reconstructed using the methods presented in this thesis is shown in the bottom panel and compared against the vacuum rotational transform profile, obtained using a vacuum VMEC calculation. Here, small deviations between the vacuum  $\iota$  profile and the plasma case are observed. These are expected due to the finite current density, which introduces small modifications of the local rotational transform. The value at the LCFS is not entirely matched, which is consistent with the small, but finite deviations already observed in the flux surface comparison plot 42.

Finally, the reconstructed magnetic diagnostic signals should be compared against the measured values. This is shown in Fig. 44. The first sensor is the diamagnetic loop in the triangular-shaped plane, followed by a closed Rogowski coil. These two sensors provide comparably “global” information about the plasma, namely the diamagnetic energy and the net toroidal current. Therefore, their error bars are comparably small and their values

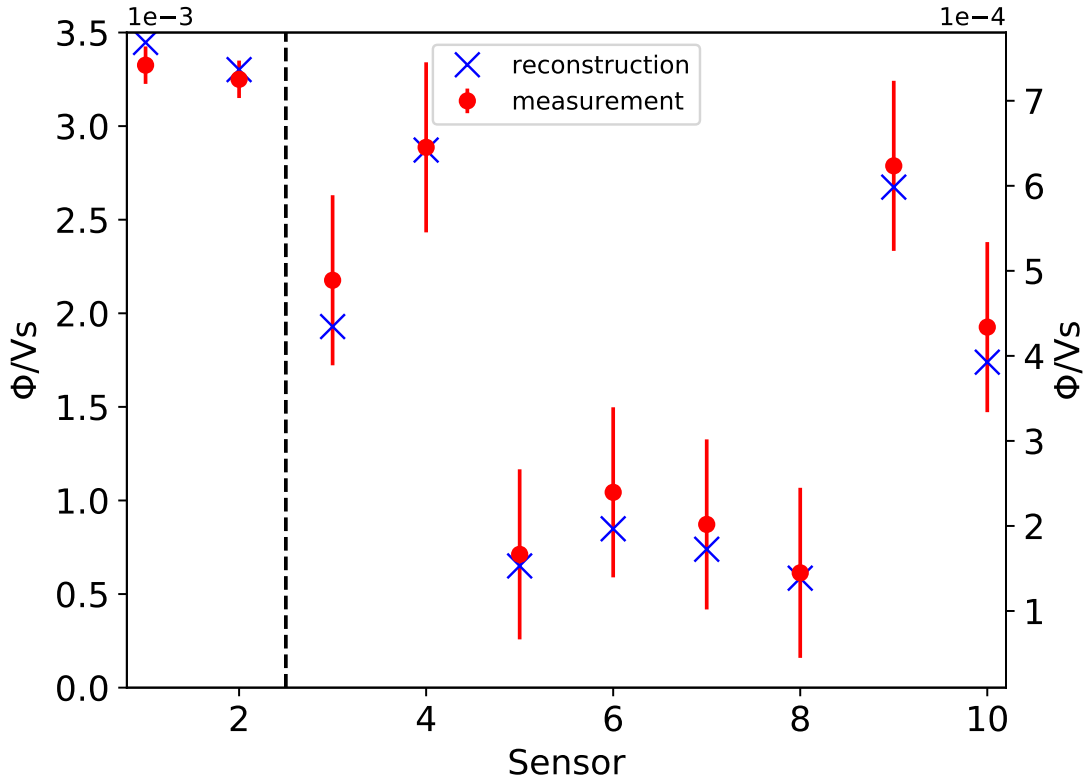


Fig. 44: Final set of reconstructed magnetic diagnostic signals in comparison with measured signals. From left to right, the signals of the diamagnetic loop, closed Rogowski coil and eight segmented Rogowski coils in the triangular-shaped plane are shown with measurements as red dots and prediction as blue crosses.

are easily matched in the reconstruction process by adjusting the central pressure and the toroidal current. The remaining signals correspond to eight segmented Rogowski coils in the triangular-shaped plane. Also in this plot, a dipolar-shaped pattern due to the Pfirsch-Schlüter currents can be observed, which is superposed on a net signal in all sensors due to the finite net toroidal current. The matching of these sensors is also well within the error estimates. This is not very surprising, since the reconstruction algorithm specifically optimized the MHD equilibrium to reproduce exactly these observed signals. However, former (unsuccessful) attempts of reconstructions developed convergence problems due to errors in the signal prediction, calibration factors, etc., which could not be covered by the VMEC equilibria. In short, not every pattern in the magnetic diagnostics signals can be reproduced by the reconstruction code. It is therefore rewarding to specifically investigate the matching quality of the predicted signals to the measurements for each sensor individually rather than (blindly) aim for maximized posterior probability values.

## 5. Discussion

In the last section of this thesis, I will discuss the methods and results from this thesis and locate them in a larger context. First, the datasource for the magnetic diagnostics of W7-X is given a second loop. Some comments on the VMEC equilibrium code follow. The numerical methods needed to compute the magnetic field and vector potential of filamentary wire segments are discussed next. This leads to the calculation of the prediction for the magnetic diagnostics responses. A treatment of the Minerva framework as the “working horse” in this thesis comes next. Experimental results are discussed in the following from both calibration experiments for the magnetic diagnostics as well as the first equilibrium reconstruction results using this new implementation.

### 5.1. Datasource for Magnetic Diagnostics

The datasource for access to the pre-evaluated data from the magnetic diagnostics proved to work reliable during OP1.2a of W7-X. The simple dechopping algorithm presented in Sec. 3.1.3 proved to be sufficient for the analysis tasks so far. If requirements for more precise results appear in the future, as might be the case especially for time-dependent analysis, the interpolation algorithm presented in Ref. [27] can be implemented.

Error estimations need further development, as the currently employed constant error margins are most likely too broad and can be narrowed by taking the accumulation properties of the integration results into account. For all 200 magnetic diagnostic channels, raw data is acquired with 16 bit resolution at a sampling rate of 2 MSPS, leading to a total data rate of 800 MB/s. First tests of the pre-evaluation program for OP1.2b revealed that the current implementation is able to reliably deal with data from experiment programs of up to 100s length, corresponding to 80 GB of raw data. The implementation of the dechopping and integration algorithm was the easy part in writing the magnetics pre-evaluation routines; to reliably deal with these large amounts of data in an environment of heavily loaded network connections during experiment days was much more difficult.

However, by intense communication with the maintainers of the access software developed for the central data archive, these difficulties have been overcome and resulted in integration of an optimized method in the database access routines to load data of multiple channels per request<sup>6</sup>, addressing the current limitation and enabling analysis of quasi-steady-state experiments of up to 1800s length in the planned operational phase OP2 of W7-X.

### 5.2. VMEC

The choice of VMEC as the main working horse to compute the magnetohydrodynamic equilibria needed in the equilibrium reconstruction process was mainly dictated by the fact, that this code has proven to converge reliably and provide accurate results on comparably short execution time scales. Further comparisons against reconstructions performed with a MHD equilibrium code, which is aware of magnetic islands, are needed to quantify the discrepancy between the VMEC solution and the actual plasma parameters. For the standard magnetic configuration of W7-X, in which the reference experiment used for the reconstruction presented in this work has been performed, the VMEC code was able to compute an equilibrium consistent with the measured data within the currently available error estimates. The 10/11 magnetic island chain inside the plasma does not introduce severe numerical artifacts in the computed current density, as shown in Fig. 34.

However, artifacts are still present in the plasma core region near the magnetic axis and close to the LCFS. This is a known issue to the developers of VMEC and the current solution of subtracting the current density output of a vacuum ( $I_{\text{tor}} = 0 \text{ A}$ ,  $p_0 = 1e - 6 \text{ Pa}$ ) VMEC computation solved this issue for the prediction of most of the magnetic diagnostics in W7-X. The prediction for the large saddle coils, shown in Fig. 37, shows some residual differences to results obtained by the DIAGNO magnetic diagnostics prediction code. Since DIAGNO uses a virtual casing principle, it is not dependant on an accurate computation of the current density in the plasma volume and can therefore provide more accurate results. As I increased the number of flux surfaces to take into account in a VMEC computation to more than 1000 flux surfaces, a very slow variation of the predicted signals for the large saddle coils towards the values calculated by the DIAGNO code was observed.

<sup>6</sup>MultiSignalReader in the SignalAccess library 1.6.1, published on 06/08/2018

The calculation of these equilibria however became so slow that it was decided to rather exclude the critical magnetic diagnostics from these first attempts of equilibrium reconstructions. Variations in the resolution of the response matrices and other convergence parameters did not have a significant effect on the deviation between the predicted signals for the large saddle coils when computed using a volume integral over the current density on the one hand and the virtual casing method on the other. Therefore, the residual discrepancy was attributed to numerical errors in calculating the finite radial differences for obtaining the current density in the plasma.

The current density is integrated in the step after its derivation from the magnetic field components during the response prediction for the magnetic diagnostics. Integration by parts can be carried out in the radial direction to circumvent the necessity for calculating finite differences of the magnetic field components. Instead, the radial differencing would have to be conducted on more well-behaved quantities, like the flux surface geometry coefficients. Ultimately, a rigorous derivation of the underlying mathematical principles is needed to develop a method for accurate current density calculation in a possible successor to VMEC. The implementation of the current density calculation routines in the Minerva framework is (to my current knowledge) the only independent implementation for this task outside the VMEC codebase. Since (again my knowledge) no publication is available, where the details of the numerical tricks applied in the derivation are accurately described, significant investigations were needed to understand the details of this routine. An in-depth understanding of these computational steps was necessary in order to identify sources for deviations among the results obtained from different implementations, as shown above. I would consider this as the part of this thesis, which involved the most detailed work and was most complicated to accomplish.

The remote execution procedures developed in the course of this work for execution of the parallelized PARVMEC version [50] on the Draco supercomputer provided a significant speedup to the reconstruction process. This was especially noticeable during maintenance periods of the cluster, when execution of VMEC had to be performed on the shared webservice cluster available at IPP Greifswald or even on a local computer.

### 5.3. Magnetic Field and Vector Potential of Filamentary Wire Segments

The checks of the available methods to compute the magnetic vector potential and magnetic field of filamentary wire segments in the Minerva framework were straightforward and quickly revealed the convergence difficulty in the computation of the magnetic vector potential mentioned in Ref. [32]. The implementation of the new method from the reference was straightforward as well. Brief investigations showed an improved matching between the response matrices for the magnetic diagnostics as calculated by my implementation in the Minerva framework and the results obtained using the V3RFUN code. Extension of the range of parameter values used for testing the convergence in the reference revealed a second range of parameter values, where convergence was only re-established after a slight reformulation of the formula given in the reference.

However, a more complicated test case involving a single wire loop energized by a unit current (1 A) and a concentric fluxloop showed convergence properties worse than expected. Further improvement is likely to be possible, because saturation of the obtained numerical accuracy was not observed yet for the resolution parameters used in the presented case. This was left for in the future, since the actual goal of computing accurate response matrices

for the magnetic diagnostics to be used in the equilibrium reconstruction process was already achieved to sufficient precision required for the use case.

#### 5.4. Magnetic Diagnostics Response Prediction

Implementation and testing of the numerical tools to compute the magnetic diagnostic responses based on the filamentary wire segments methods was straightforward and did not pose any significant difficulties, once access to the source code of V3POST and BMW was granted for adding additional output of intermediate quantities necessary for detailed comparisons with my implementation. Tests on the required grid resolutions for the response matrices quickly revealed excellent stability of the results, leading to the conclusion that accuracy improvements for the overall reconstruction process can more easily be achieved in other areas of the code, e.g. in the current density computation for a VMEC equilibrium, as outlined above.

So far, only fully toroidally and stellarator-symmetric response matrices and VMEC calculations have been analyzed. The currently used model for the geometry of both confinement and diagnostic coil geometries was obtained by laser-tracked measurements during the assembly phase. But, deformations of the confinement coils due to cooldown to cryogenic temperatures and electromagnetic forces as well as deformations due to pumpdown of the plasma vessel and cryostat have not been into account yet. Also, the available coil geometries are currently implemented as exact values without error estimates into the analysis toolchain. In-depth analysis regarding the impact of the estimated coil geometry deviations on predictions for the confinement magnetic field as well as the predictions for measured signals are ongoing.

If the outcome of these investigations demands to take the asymmetries into account, the available methods for predicting the magnetic diagnostic signals are already equipped with the necessary options to be activated. The geometry of the VMEC output currently demands for the cylindrical symmetry in the form of toroidal cutplanes, on which the response factors for the magnetic diagnostics are calculated. This geometry was chosen to be implemented in this work. Replacement of the VMEC code with another equilibrium code, which possibly does need not take the cylindrical symmetry into account, might require to also change the response matrix geometry. Here, hierarchical matrices [51] could provide a format for storing the response factors while simultaneously performing a significant compression of their size and still providing control over the errors due to the approximations.

Comparing the final response prediction results for a finite- $\langle\beta\rangle$  equilibrium, the predictions show a spot-on match to the results from the V3POST code. This is expected, since my implementation in the Minerva framework is based on the numerical principles employed in that code to a large extent. The overall agreement to the results obtained using the DIAGNO code is comparably well, although minor differences remain. This can most likely be attributed to the method of computing the current density inside the plasma from a VMEC calculation, as outlined above. It should be mentioned, that the DIAGNO code was not employed in the reconstruction process due to its prohibitively long execution times for computing the responses for all 200 magnetic diagnostics of W7-X on the order of 30 minutes, as compared to 3 seconds for the volume integral computation.

## 5.5. The Minerva Framework

The Minerva framework is the “central working horse” employed in this thesis. The requirement to implement scientific data analysis tools in the Java programming language might seem counterintuitive at first, but has proven to introduce a lot of structure into the workflow. The first step is always the hardest, and this applies as well for the Minerva framework, as introductory documentation is largely missing and well-maintained examples are rare. However, from my point of view, it is definitely worth the effort as will become clear in the following. The Minerva framework brings methods together, which are usually separated in the workflow of a physicist, e.g. large scale mathematical tools as the LAPACK and GSL numerical libraries and Web 2.0 concepts as SOAP webservices, combined with sophisticated Bayesian statistical methods and the Maven version control and package management system. It should be noted that apart from the VMEC code, all numerical analysis tools used throughout this thesis have been implemented in the Minerva framework. Even the data plots shown in this thesis have been largely created on the fly from within the framework by an interface<sup>7</sup> to the Matplotlib plotting library. The use of an integrated version control system for the source code in combination with a package management system, as available by the Maven program and currently in use for management of the Minerva source code, directly contributes to the call for traceability of results and reproducibility of analysis results [52] by the German Research Foundation (DFG).

In this context, the concept of datasources addresses the data-metadata problem, where the assignment between measured data and the metadata (calibration factors, geometric information, resolution settings for simulations, etc.) is automatically enforced by a correctly implemented datasource. As the datasource provides measured data as well as the metadata belonging to the measurements from within the same module in the framework, it is comparably simple to implement congruent supply methods herein. All other parts of the analysis toolchain do not need to know about the internals of the datasource and, if implemented coherently, just access the metadata provided by the datasource. The source code of datasource itself (including calibration factors etc.) is under source code version control and all changes in the metadata are directly propagated along the analysis toolchain and traceable in the version control system.

In the reconstructions presented in this thesis, parameterized profiles for the plasma pressure and the toroidal current have been used in the equilibrium model. A sub-model for obtaining the pressure profile self-consistently from various diagnostics at W7-X is currently under development and already has been applied to OP1.1 data [53]. To keep the number of unknowns low in the first reconstruction attempts using the newly-developed code, inclusion of the measured pressure profile was left for future work.

The current density profile in the plasma can not be measured by any of the available diagnostics at W7-X to this date; however, a Motional Stark Effect diagnostic [54] is planned and under construction. Up to its completion and successful commissioning, the shape of the toroidal current profile remains an optimization parameter. Preliminary analysis results obtained using the V3FIT equilibrium reconstruction code show, that the current profile is quite well constrained by the magnetic diagnostics [45]. The pressure and current profile shapes used for the first reconstructions in the Minerva framework were adapted from the results obtained using the V3FIT and STELLOPT reconstruction tools.

The substructuring of the reconstruction code implemented in the Minerva framework into dedicated parts proved to improve the transparency of the overall methodology and

---

<sup>7</sup>JyPlot; credits to S. Kwak

helped a lot in debugging the individual components. The automatized graph printout generation, which was used to obtain the basis for Fig. 28, adds to this, although minor adjustments on the layout suggestions by the code are needed to achieve publication quality graphs.

## 5.6. Magnetic Diagnostics Calibration Experiments

The analysis of the magnetic diagnostics calibration experiments was used to identify the correct polarity of the magnetic diagnostic signals prior to performing equilibrium reconstructions. Calibration experiments have been performed by the scientific staff of W7-X prior to and during OP1.2a using a conductor along the magnetic axis, the main magnetic field coils and the trim coils. Analysis of a subset of these experiments provided a clear picture for most of the magnetic diagnostic signal polarities, which was found to be a crucial step on the path to successful equilibrium reconstructions. There are multiple possibilities to swap signs in the input parameters of the MHD equilibrium calculation and magnetic diagnostics response calculation, which finally produce only slightly different predictions. However, only the right combination correctly converges in the analysis of actual experimental data. A stepwise approach with many cross-checks between the available computational tools was used and proved to ensure consistent results in the reconstruction step.

Improvements can be made whatsoever, e.g. the investigation of the measurements during trim coil current ramps revealed that the mean eddy currents have barely vanished at the end of the flat-top phases. This has two implications. It is well possible that parts of the eddy currents are still present or not yet fully developed at the timestamps used to calibrate the magnetic diagnostic predictions against the measurements. An increase in the length of the flat-top phases in the trim coil current ramps was therefore proposed in agreement with the maintainers of the magnetic diagnostics for the upcoming operational phase OP1.2b of W7-X.

## 5.7. Reconstruction Results

Regarding the presented reconstruction results, one can conclude that reconstructions of MHD equilibria of plasma experiments in W7-X are indeed possible to be conducted using the approach and numerical toolchain presented in this work. The results look quite reasonable, given the reduced subset of free parameters and the fact that on top of the magnetic diagnostics signals only a virtual observation on the rotational transform profile was used to constrain the inversion routines. Here, the maximum posterior inversion algorithm showed slow, but steady convergence towards the final set of parameters. Significant speedup is to be expected from implementation of the quasi-Newton inversion technique in combination with a singular value decomposition of the Jacobian matrix of the reconstruction model, as used in the V3FIT code [16]. Linear dependencies between several of the free parameters can already be observed in the reconstruction where the constraint on  $\iota_{\text{edge}}$  is enforced, as the free parameters varied by the MAP algorithm approximately stay within constant ratios to each other. As the Hooke and Jeeves optimizer inside the MAP inversion method is only allowed to vary one parameter at a time, it cannot identify the linear dependencies of the free parameters.

In the context of full non-linear error estimation for the free parameters, Markov-chain Monte Carlo (MCMC) inversion methods [18] can be readily applied to any self-contained model in the Minerva framework. These would provide error estimates on the physics

parameters used to model the MHD equilibrium and therefore indicate the ranges of the free parameters, which are compatible with the measurements up to their error estimates. Nothing comes for free, and the price for MCMC inversions is a significantly increased number of iterations needed to complete such an inversion, which is some orders of magnitude larger than the requirements of the MAP algorithm.

In the current reconstruction model, the calculation of the MHD equilibrium using the VMEC code is the main timing bottleneck. An execution cycle takes about one minute, and this cannot be decreased significantly by more computing power, as even the parallelized VMEC version employed for this work can only use up to one processor per two flux surfaces. In order to keep the computational effort low, a number of flux surfaces has been chosen, which is only slightly larger than the minimum number of flux surfaces needed to reliably produce convergent and consistent results.

Using neural networks might be a convenient approach to significant speedup. The neural network would have to be trained on a sufficiently large set of VMEC calculations, covering the expected free parameter space found during experiments. The general approach is not new and has already been implemented in the past as a function parametrization of the flux surface geometry [55]. However, selecting the right parameters and their ranges is a difficult task. If one would attempt to cover all possible variations of this highly-nonlinear problem, a prohibitively large number of VMEC runs (i.e. the training set for the neural network) would be required. This task is therefore left for future work.



## 6. Summary

This work focuses on the magnetohydrodynamic equilibrium in the optimized stellarator Wendelstein 7-X. The MHD equilibrium state is defined by a force balance between an inward-directed pressure gradient and the Lorentz force due to plasma currents. Solution of this force balance is a highly non-trivial task. Advanced numerical tools have to be applied in order to find equilibrium solutions for well-defined input parameters.

In order to obtain relevant predictions for future experiments, the equilibria used in their modeling need to resemble the experimental plasma conditions as close as possible. This is assessed using an approach known as equilibrium reconstruction. Here, predictions are computed for the included diagnostics and the input parameters of the MHD equilibrium solver are successively adapted, in order to reproduce the measured signals as close as possible. In this work, the magnetic diagnostics installed at Wendelstein 7-X have been used for this task in companion with the VMEC MHD equilibrium solver. A magnetic diagnostic prediction toolchain was implemented and validated in the Bayesian modeling framework Minerva. This toolchain is based on existing codes, which did not implement the strict model-based approach present in the Minerva framework.

The calculation of predictions for the magnetic diagnostic signals from the output of the VMEC code is a computationally expensive task. However, several intermediate quantities can be computed in advance. This led to a significant speedup of the overall performance of the reconstruction algorithm.

First reconstructions have been performed for a selected reference experiment program from the second experimental campaign of Wendelstein 7-X. The measured signals are well reproduced by the reconstruction and the resulting equilibria are reasonably consistent with further analysis performed on them so far.

## Zusammenfassung

Diese Arbeit konzentriert sich auf das magnetohydrodynamische Gleichgewicht im optimierten Stellarator Wendelstein 7-X. Das MHD-Gleichgewicht ist definiert als ein Kräftegleichgewicht zwischen einem nach innen gerichteten Druckgradienten und der Lorentzkraft, hervorgerufen durch Plasmaströme. Die Lösung dieser Gleichgewichtsbedingung ist eine in höchstem Maße nicht-triviale Aufgabe. Fortgeschrittene numerische Werkzeuge müssen angewendet werden, um einen Gleichgewichtszustand für wohldefinierte Eingangsgrößen zu berechnen.

Auf dem Weg zur Berechnung relevanter MHD-Gleichgewichte für die Planung zukünftiger Experimente müssen die modellierten Plasmabedingungen den experimentellen Zuständen möglichst genau entsprechen. Hierzu wird eine Methode, die als Gleichgewichtsrekonstruktion bekannt ist, angewendet. Dabei werden die Eingabeparameter der Gleichgewichtsberechnung sukzessive angepasst, bis die vorhergesagten Meßsignale für ausgewählte Diagnostiken möglichst gut zu deren Messwerten passen.

In dieser Arbeit wurden die magnetischen Gleichgewichtsdiagnostiken zusammen mit dem VMEC-Code zur Berechnung des MHD-Gleichgewichts eingesetzt. Ein Satz von Berechnungswerkzeugen zur Vorhersage der Meßsignale der magnetischen Diagnostiken wurde im Bayesschen Modellierungsframework Minerva implementiert und validiert. Diese Berechnungsmethodik basiert auf existierenden Codes, die allerdings den strikten modellbasierten Ansatz des Minerva-Frameworks nicht umsetzen.

Die Berechnung der Vorhersagen für die gemessenen Signale der magnetische Diagnostiken auf Basis einer Berechnung durch den VMEC-Code ist eine rechenintensive Aufgabe, jedoch können Zwischenergebnisse vorausberechnet und abgespeichert werden. Die Verwendung dieser vorausberechneten Größen führte zu einer deutlichen Beschleunigung des Rekonstruktionsalgorithmus.

Erste Rekonstruktionen wurden für ein ausgewähltes Referenzexperiment aus der zweiten Betriebsphase von Wendelstein 7-X durchgeführt. Die gemessenen Signale werden gut durch die Rekonstruktion reproduziert und die erhaltenen Gleichgewichte zeigen glaubwürdige Übereinstimmung mit weiterführenden Analysen, die bisher durchgeführt wurden.

## References

- [1] D. Clery, *The bizarre reactor that might save nuclear fusion*, (Oct. 2015) <http://www.sciencemag.org/news/2015/10/bizarre-reactor-might-save-nuclear-fusion> (visited on 06/16/2018).
- [2] W. Lotz, P. Merkel, J. Nührenberg, A. Schlüter, and R. Zille, *Optimization of Helias for W VII-X*, tech. rep., IAEA-TECDOC-558 (International At. Energy Agency (IAEA), 1990), pp. 485–491.
- [3] G. Grieger et al., “Physics optimization of stellarators”, *Phys. Fluids B: Plasma Phys.* **4**, 2081–2091 (1992).
- [4] H. Alfvén, *Cosmical Electrodynamics: Fundamental Principles*, The International series of monographs on physics (Oxford University Press, 1953).
- [5] P. Helander, “Theory of plasma confinement in non-axisymmetric magnetic fields”, *Rep. Prog. Phys.* **77**, 087001 (2014).
- [6] U. Schumacher, *Fusionsforschung* (Wiss. Buchges., 1993).
- [7] J. Wesson and D. Campbell, *Tokamaks*, The International series of monographs on physics (Oxford University Press, 2011).
- [8] K. Ida et al., “Radial electric field and transport near the rational surface and the magnetic island in LHD”, *Nucl. Fusion* **44**, 290 (2004).
- [9] H. Renner, J. Boscary, H. Greuner, H. Grote, F. W. Hoffmann, J. Kisslinger, E. Strumberger, and B. Mendelevitch, “Divertor concept for the W7-X stellarator and mode of operation”, *Plasma Phys. Controlled Fusion* **44**, 1005 (2002).
- [10] T. S. Pedersen et al., “Confirmation of the topology of the Wendelstein 7-X magnetic field to better than 1:100,000”, *Nat. Commun.* **7**, 13493 (2016).
- [11] H. Wobig and H. Renner, *Stellarator Research at the IPP in Garching*, tech. rep., IPP 2/343 (1999), pp. 1–6.
- [12] D. Pfirsch and A. Schlüter, tech. rep., MPI/PA/7/62 (Max-Planck-Institute for Plasma Physics, 1962).
- [13] P. Helander et al., “Stellarator and tokamak plasmas: a comparison”, *Plasma Phys. Controlled Fusion* **54**, 124009 (2012).
- [14] A. H. Boozer, “Establishment of magnetic coordinates for a given magnetic field”, *Phys. Fluids* **25**, 520–512 (1982).
- [15] S. Bozhnikov, J. Geiger, M. Grahl, J. Kießlinger, A. Werner, and R. Wolf, “Service oriented architecture for scientific analysis at W7-X. An example of a field line tracer”, *Fusion Eng. Des.* **88**, 2997–3006 (2013).
- [16] J. D. Hanson, S. P. Hirshman, S. F. Knowlton, L. L. Lao, E. A. Lazarus, and J. M. Shields, “V3FIT: a code for three-dimensional equilibrium reconstruction”, *Nucl. Fusion* **49**, 075031 (2009).
- [17] W. H. Press, S. A. Teukolsky, W. T. Vetterling, and B. P. Flannery, *Numerical Recipes 3rd Edition: The Art of Scientific Computing* (Cambridge University Press, New York, NY, USA, 2007).
- [18] D. S. Sivia and J. Skilling, *Data analysis: a Bayesian tutorial* (Oxford University Press, 2006).

- 
- [19] E. Pasch, M. N. A. Beurskens, S. A. Bozhenkov, G. Fuchert, J. Knauer, R. C. Wolf, and the W7-X Team, “The Thomson scattering system at Wendelstein 7-X”, *Rev. Sci. Instrum.* **87**, 11E729 (2016).
- [20] H. Damm, “Upgrade of the Wendelstein 7-X Thomson Scattering Diagnostic to Study Short Transient Plasma Effects”, Master thesis (2018).
- [21] C. Nührenberg, “Computational ideal MHD: Alfvén, sound and fast global modes in W7-AS”, *Plasma Phys. Controlled Fusion* **41**, 1055 (1999).
- [22] M. Endler et al., “Engineering design for the magnetic diagnostics of Wendelstein 7-X”, *Fusion Eng. Des.* **100**, 468–494 (2015).
- [23] S. Besshou, C. Thomas, T. Ohba, A. Iiyoshi, and K. Uo, “Diamagnetism and beta in beam heated currentless plasmas of Heliotron E”, *Nucl. Fusion* **26**, 1339–1348 (1986).
- [24] A. Werner, “W7-X magnetic diagnostics: Performance of the digital integrator”, *Rev. Sci. Instrum.* **77**, 10E307 (2006).
- [25] C. Hennig et al., “ArchiveDB – Scientific and technical data archive for Wendelstein 7-X”, *Fusion Eng. Des.* **112**, 984–990 (2016).
- [26] P. Horowitz and W. Hill, *The Art of Electronics*, 3rd ed. (Cambridge University Press, 2015).
- [27] E. Chlechowicz, “Plasma Current and Pressure Measurement at the WEGA Stellarator”, Diploma thesis (2010).
- [28] K. Rahbarnia et al., “Diamagnetic energy measurement during the first operational phase at the Wendelstein 7-X stellarator”, *Nucl. Fusion*, accepted (2018).
- [29] J. Svensson and A. Werner, “Large scale Bayesian data analysis for Nucl. Fusion experiments”, in 2007 IEEE International Symposium on Intelligent Signal Process., Conference Proceedings Book (2007), pp. 955–960.
- [30] S. P. Hirshman and J. C. Whitson, “Steepest-descent moment method for three-dimensional magnetohydrodynamic equilibria”, *Phys. Fluids* **26**, 3553–3568 (1983).
- [31] W. D. D’haeseleer, W. N. G. Hitchon, J. D. Callen, and J. L. Shohet, *Flux Coordinates and Magnetic Field Structure*, Springer Series in Computational Physics (Springer Berlin Heidelberg, 1991).
- [32] J. D. Hanson and S. P. Hirshman, “Compact expressions for the Biot-Savart fields of a filamentary segment”, *Phys. Plasmas* **9**, 4410–4412 (2002).
- [33] J. D. Jackson, *Classical Electrodynamics*, 5th ed. (Wiley, New York, NY, 2014).
- [34] S. P. Hirshman, E. A. Lazarus, J. D. Hanson, S. F. Knowlton, and L. L. Lao, “Magnetic diagnostic responses for compact stellarators”, *Phys. Plasmas* **11**, 595–603 (2004).
- [35] M. Drevlak, D. Monticello, and A. Reiman, “PIES free boundary stellarator equilibria with improved initial conditions”, *Nucl. Fusion* **45**, 731–740 (2005).
- [36] M. Grahl et al., “Archive WEB API: A web service for the experiment data archive of Wendelstein 7-X”, *Fusion Eng. Des.* **123**, Proceedings of the 29th Symposium on Fusion Technol. (SOFT-29) Prague, Czech Republic, September 5-9, 2016, 1015–1019 (2017).

- [37] S. Schmuck, H.-J. Hartfuss, M. Hirsch, and T. Stange, “Design of the ECE diagnostic at Wendelstein 7-X”, *Fusion Eng. Des.* **84**, Proceeding of the 25th Symposium on Fusion Technol., 1739–1743 (2009).
- [38] A. Langenberg, J. Svensson, H. Thomsen, O. Marchuk, N. A. Pablant, R. Burhenn, and R. C. Wolf, “Forward Modeling of X-Ray Imaging Crystal Spectrometers Within the Minerva Bayesian Analysis Framework”, *Fusion Sci. Technol.* **69**, 560–567 (2016).
- [39] R. Hooke and T. A. Jeeves, ““Direct Search” Solution of Numerical and Statistical Problems”, *J. ACM* **8**, 212–229 (1961).
- [40] D. Weissenburger, *SPARK Version 1.1 User’s Manual*, tech. rep., PPPL-2494 (Princeton Plasma Phys. Lab., 1988).
- [41] K. Weltner, *Mathematik für Physiker 1: Basiswissen für das Grundstudium der Experimentalphysik*, Springer-Lehrbuch (Springer Berlin Heidelberg, 2011).
- [42] S. A. Lazerson, S. Sakakibara, and Y. Suzuki, “A magnetic diagnostic code for 3D fusion equilibria”, *Plasma Phys. Controlled Fusion* **55**, 025014 (2013).
- [43] T. Windisch, *Stromtrieb Kalibration Magnetik*, tech. rep., 1-QX-T0026.0 (Max-Planck-Institute for Plasma Physics, 2015).
- [44] M. Cianciosa, personal communication, Sept. 5, 2017.
- [45] J. Schmitt, personal communication, Sept. 4, 2017.
- [46] A. Reiman et al., “Physics design of a high-beta quasi-axisymmetric stellarator”, *Plasma Phys. Controlled Fusion* **41**, B273 (1999).
- [47] S. A. Lazerson, “The virtual-casing principle for 3D toroidal systems”, *Plasma Phys. Controlled Fusion* **54**, 122002 (2012).
- [48] R. S. Elliot, *Electromagnetics*, IEEE Press Series on Electromagnetic Waves (Wiley-IEEE Press, UK, 1993).
- [49] S. Lazerson, personal communication, May 22, 2018.
- [50] S. K. Seal, S. P. Hirshman, A. Wingen, R. S. Wilcox, M. R. Cianciosa, and E. A. Unterberg, “PARVMC: An Efficient, Scalable Implementation of the Variational Moments Equilibrium Code”, in 45th International Conference on Parallel Processing (2016), pp. 618–627.
- [51] S. Börm, L. Grasedyck, and W. Hackbusch, “Introduction to hierarchical matrices with applications”, *Eng. Anal. Boundary Elem.* **27**, 405–422 (2003).
- [52] “Sicherung guter wissenschaftlicher Praxis”, in *Sicherung guter wissenschaftlicher praxis* (Wiley-Blackwell, 2013), pp. 1–109.
- [53] S. Kwak, personal communication, Aug. 1, 2017.
- [54] R. Reimer, A. Dinklage, J. Geiger, J. Hobirk, M. Reich, R. Wolf, and ASDEX Upgrade and Wendelstein 7-X Teams, “Motional Stark Effect Spectra Simulations for Wendelstein 7-X”, *Contributions to Plasma Phys.* **50**, 731–735.
- [55] A. Sengupta, J. Geiger, and P. J. McCarthy, “Statistical analysis of the equilibrium configurations of the W7-X stellarator”, *Plasma Phys. Controlled Fusion* **49**, 649 (2007).
- [56] S. E. Attenberger, W. A. Houlberg, and S. P. Hirshman, “Some Practical Considerations Involving Spectral Representations of 3D Plasma Equilibria”, *J. Comput. Phys.* **72**, 435–448 (1987).

- [57] E. Strumberger, S. Günter, P. Merkel, E. Schwarz, C. Tichmann, and H.-P. Zehrfeld, “Numerical computation of magnetic fields of two- and three-dimensional equilibria with net toroidal current”, *Nucl. Fusion* **42**, 827–832 (2002).

## A. Numerical Details

The MHD equilibrium is represented by the flux surface geometry and the magnetic field on the flux surfaces. In VMEC, both the flux surface geometry and the magnetic field are represented as twodimensional Fourier series in the normalized toroidal and poloidal coordinates  $u$  and  $v$ .

A Fourier representation of a given magnetic field can be found by performing a Fourier transform of recorded “timetraces” of magnetic field strength,  $R$  and  $Z$  coordinates when numerically following a magnetic field line. A spectrum of Fourier coefficients for the magnetic field may be computed analogously to extracting the frequency components of a measured electronics signal in a Spectrum Analyzer. In this picture, the “frequency” is given by the toroidal and poloidal mode numbers and the rotational transform [14].

The number of flux surfaces taken into account in a VMEC calculation is specified in the input file as parameter **ns** and thereby determines the radial resolution of a calculation. The radial coordinate  $s$  is then discretized into **ns** values as follows:

$$s_i = \frac{i}{\mathbf{ns} - 1}, \quad i = 0, 1, \dots, \mathbf{ns} - 1 \quad \Rightarrow \quad 0 \leq s_i \leq 1 \quad (70)$$

and all radially-dependent quantities in the output file **wout** are stored as discrete values at these radial locations.

VMEC uses a Fourier representation in the toroidal and poloidal angle-like coordinates with **mpol** poloidal modes  $m = 0, \dots, \mathbf{mpol}$  and  $2 * \mathbf{ntor} + 1$  toroidal modes  $n = -\mathbf{ntor}, \dots, 0, \dots, \mathbf{ntor}$ . For the  $m = 0$  case, only positive toroidal mode numbers are required. Thus, a total number of  $2 * \mathbf{mpol} * \mathbf{ntor}$  mode number combinations is used to enumerate the Fourier coefficients.

The combinations of toroidal and poloidal mode numbers are merged into one dimension of length  $2 * \mathbf{mpol} * \mathbf{ntor}$ . The two mode number vectors **xm** for the poloidal and **xn** for the toroidal mode numbers contain the  $(m, n_{\text{fp}}n)$  values used in the Fourier summation and are organized as listed in Tab. 2. The names of the output variables are shown in Tab. 3. Given a set of VMEC coordinates  $(s, u, v)$ , one can compute the corresponding real-space location using the Fourier series for the  $R$  and  $Z$  components of a cylindrical coordinate system as follows:

$$R(s, u, v) = \sum_{m,n} \left( R_{mn}^{\text{cos}}(s) \cos(2\pi(mu - nn_{\text{fp}}v)) + R_{mn}^{\text{sin}}(s) \sin(2\pi(mu - nn_{\text{fp}}v)) \right) \quad (71)$$

$$Z(s, u, v) = \sum_{m,n} \left( Z_{mn}^{\text{cos}}(s) \cos(2\pi(mu - nn_{\text{fp}}v)) + Z_{mn}^{\text{sin}}(s) \sin(2\pi(mu - nn_{\text{fp}}v)) \right) \quad (72)$$

The use of Fourier series for representing the toroidal and poloidal dependencies results in analytical expressions for derivatives with respect to these coordinates:

$$\frac{\partial R}{\partial u} = \sum_{m,n} \left( -m R_{mn}^{\text{cos}}(s) \sin(mu - nn_{\text{fp}}v) + m R_{mn}^{\text{sin}}(s) \cos(mu - nn_{\text{fp}}v) \right) \quad (73)$$

$$\frac{\partial R}{\partial v} = \sum_{m,n} \left( nn_{\text{fp}} R_{mn}^{\text{cos}}(s) \sin(mu - nn_{\text{fp}}v) - nn_{\text{fp}} R_{mn}^{\text{sin}}(s) \cos(mu - nn_{\text{fp}}v) \right) \quad (74)$$

$$\frac{\partial Z}{\partial u} = \sum_{m,n} \left( -m Z_{mn}^{\text{cos}}(s) \sin(mu - nn_{\text{fp}}v) + m Z_{mn}^{\text{sin}}(s) \cos(mu - nn_{\text{fp}}v) \right) \quad (75)$$

$$\frac{\partial Z}{\partial v} = \sum_{m,n} \left( nn_{\text{fp}} Z_{mn}^{\text{cos}}(s) \sin(mu - nn_{\text{fp}}v) - nn_{\text{fp}} Z_{mn}^{\text{sin}}(s) \cos(mu - nn_{\text{fp}}v) \right) \quad (76)$$

array index $mn$	$m = xm[mn]$	$n_{fp}n = xn[mn]$
0	0	0
...	0	...
$ntor-1$	0	$n_{fp} \cdot ntor$
$ntor$	1	$-n_{fp} \cdot ntor$
...	1	...
$2 \cdot ntor$	1	0
...	1	...
$3 \cdot ntor-1$	1	$n_{fp} \cdot ntor$
...	...	...
$2 \cdot ntor \cdot (mpol-1)$	$mpol-1$	$-n_{fp} \cdot ntor$
...	...	...
$mnmax - 1$	$mpol-1$	$n_{fp} \cdot ntor$

Tab. 2: Mode number combinations used for the truncated Fourier series representation of flux surface coordinates in VMEC. For  $m = 0$ , only positive  $n$  are needed to support a complete truncated Fourier basis. Note that the number of toroidal periods  $n_{fp}$  has already been included in the  $xn$  array.

quantity	component name		dimensions
	symmetric	non-symmetric	
$R_{mn}$	<b>rmnc</b>	<b>rmns</b>	$ns \times mnmax$
$Z_{mn}$	<b>zmns</b>	<b>zmnc</b>	$ns \times mnmax$
$B_{s,mn}$	<b>bsubsmns</b>	<b>bsubsmnc</b>	$ns \times mnmax\_nyq$
$B_{u,mn}$	<b>bsubumnc</b>	<b>bsubumns</b>	$ns \times mnmax\_nyq$
$B_{v,mn}$	<b>bsubvmnc</b>	<b>bsubvmns</b>	$ns \times mnmax\_nyq$

Tab. 3: Names of the Fourier coefficient arrays for the magnetic field representations in a VMEC output file. The letter **c** or **s** after the Fourier representation indicator **mn** denotes whether the corresponding array contains the amplitudes for the cosine basis or the sine basis, respectively. **ns** denotes the number of flux surfaces taken into account for a given VMEC computation and **mnmax** denotes the number of mode number combinations in use. Several arrays contain an extended set of modes **mnmax\_nyq** to circumvent errors due to violation of the Nyquist theorem.

In order to compute a flux coordinate representation of a given set of e.g. cartesian or cylindrical coordinates, an iterative scheme is needed [56].

The current density in the plasma is given by Ampère's law [33]:

$$\mathbf{j} = \frac{1}{\mu_0}(\nabla \times \mathbf{B}) \quad (77)$$

If the curl of a covariant representation of a field is computed, this results in a contravariant representation of the resulting field and vice versa [31]. Therefore, to compute the contravariant current density components  $j^i$ , the covariant magnetic field components  $B_i$  are needed. The covariant magnetic field components

$$\mathbf{B} = B_s \nabla s + B_u \nabla u + B_v \nabla v \quad (78)$$

are represented using two-dimensional Fourier series in the VMEC output:

$$B_s(s, u, v) = \sum_{m,n} B_{s,mn}^{\cos}(s) \cos(mu - nn_{\text{fp}}v) + B_{s,mn}^{\sin}(s) \sin(mu - nn_{\text{fp}}v) \quad (79)$$

$$B_u(s, u, v) = \sum_{m,n} B_{u,mn}^{\cos}(s) \cos(mu - nn_{\text{fp}}v) + B_{u,mn}^{\sin}(s) \sin(mu - nn_{\text{fp}}v) \quad (80)$$

$$B_v(s, u, v) = \sum_{m,n} B_{v,mn}^{\cos}(s) \cos(mu - nn_{\text{fp}}v) + B_{v,mn}^{\sin}(s) \sin(mu - nn_{\text{fp}}v) \quad (81)$$

Note that, in contrast to the contravariant magnetic field representation, the radial component  $B_s \neq 0$  in the covariant representation. Given the covariant magnetic field representation, the curl of it takes a particularly simple form [31]:

$$\nabla \times \mathbf{B} = \frac{1}{\sqrt{g}} \sum_k \left( \frac{\partial B_j}{\partial i} - \frac{\partial B_i}{\partial j} \right) \hat{\mathbf{e}}_k, \quad (i, j, k) \text{ cyc. } (s, u, v). \quad (82)$$

As indicated by the constraint on the current density vector  $\mathbf{j}$  to be tangential to flux surfaces in Eq. (13), the current density can only have non-zero components in the  $u$  and  $v$  directions.

$$j^s = 0 \quad (83)$$

$$j^u = \frac{1}{\mu_0 \sqrt{g}} \left( \frac{\partial B_s}{\partial v} - \frac{\partial B_v}{\partial s} \right) \quad (84)$$

$$j^v = \frac{1}{\mu_0 \sqrt{g}} \left( \frac{\partial B_u}{\partial s} - \frac{\partial B_s}{\partial u} \right) \quad (85)$$

with the Jacobian of the coordinate transform between flux coordinates and cylindrical coordinates. The current density components are expressed in Fourier series as well:

$$j^u(s, u, v) = \sum_{m,n} \left( j_{mn}^{u,\cos}(s) \cos(mu - nn_{\text{fp}}v) + j_{mn}^{u,\sin}(s) \sin(mu - nn_{\text{fp}}v) \right) \quad (86)$$

$$j^v(s, u, v) = \sum_{m,n} \left( j_{mn}^{v,\cos}(s) \cos(mu - nn_{\text{fp}}v) + j_{mn}^{v,\sin}(s) \sin(mu - nn_{\text{fp}}v) \right) \quad (87)$$

The derivatives with respect to  $u$  and  $v$  are analytical. Derivatives with respect to  $s$  are computed as finite differences on the discrete set of flux surfaces.

More details on the representation of the flux surface geometry and the magnetic field in the VMEC output can be found in the literature [57].



## B. Explanation of Graph Nodes

In this section, explanations for the node labels found in the graph 28 are listed.

### Free Parameters

- `am0` Uniform probabilistic node, denotes the central plasma pressure.
- `am1` Uniform probabilistic node, denotes the first pressure profile shaping parameter.
- `am2` Uniform probabilistic node, denotes the second pressure profile shaping parameter.
- `phiedge` Uniform probabilistic node, denotes the toroidal magnetic flux enclosed in the LCFS.
- `adiabaticIndex` Uniform probabilistic node, denotes the adiabatic index of the plasma used for the VMEC calculation.
- `totalCurrent` Uniform probabilistic node, denotes the adiabatic index of the plasma used for the VMEC calculation.
- `ac0` Uniform probabilistic node, denotes an offset in the enclosed current profile.
- `ac1` Uniform probabilistic node, denotes the scaling of the first arctangent enclosed current profile.
- `ac2` Uniform probabilistic node, denotes the first shaping parameter for the enclosed current profile.
- `ac3` Uniform probabilistic node, denotes the second shaping parameter for the enclosed current profile.
- `ac4` Uniform probabilistic node, denotes the third shaping parameter for the enclosed current profile.

### Observations

- `iotaEdgeObs` Normal distribution observation node used to constrain  $\iota_{\text{edge}}$ .
- `dialoopsObs` Multivariate normal distribution observation node for diamagnetic and compensation loop signals.
- `rogowskiObs` Multivariate normal distribution observation node for Rogowski coil signals.
- `saddleObs` Multivariate normal distribution observation node for saddle coil signals.

### Subgraphs

- `pressure` Subgraph containing the pressure profile used in the VMEC calculation.
- `toroidalCurrent` Subgraph containing the enclosed current profile used in the VMEC calculation.

- `equiVmec` Subgraph containing the nodes necessary to calculate the MHD equilibrium using VMEC.
- `magnetics` Subgraph containing the nodes associated to the magnetic diagnostics.

### Constants

- `poloidalModes` Number of poloidal modes `mpol` to take into account in the VMEC calculation.
- `toroidalModes` Number of toroidal modes `ntor` to take into account in the VMEC calculation.
- `poloidalGridPoints` Number of `ntheta` poloidal grid points used in the VMEC equilibrium calculation and evaluation of the current density.
- `toroidalGridPoints` Number of `nzeta` toroidal grid points used in the VMEC equilibrium calculation and evaluation of the current density.
- `fullVacCalculationEvery` Number of VMEC internal iterations, after which a full vacuum magnetic field calculation is reperformed.
- `minR` Radial minimal grid extent for background magnetic field `mgrid` and response matrices.
- `maxR` Radial maximal grid extent for background magnetic field `mgrid` and response matrices.
- `minZ` Vertical minimal grid extent for background magnetic field `mgrid` and response matrices.
- `minZ` Vertical maximal grid extent for background magnetic field `mgrid` and response matrices.
- `numR` Number of radial grid points for the background magnetic field `mgrid` and response matrices.
- `numZ` Number of vertical grid points for the background magnetic field `mgrid` and response matrices.
- `toroidalPeriods` Number of field periods of the machine. For W7-X, 5.
- `lcfsIndex` Index of last closed flux surface in the radial matrix dimension. For VMEC, this is equal to `ns-1`.
- `iotaEdgeTarget` Target value for  $\iota_{\text{edge}}$  to reconstruct.
- `pulseTime` Absolute nanosecond value identifying the single timestamp for which the reconstruction will be performed.

## Computational Nodes

- **pressureProfile** Assembles a pressure profile in the predefined format compatible with the VMEC input file format.
- **currentProfile** Assembles an enclosed current profile in the predefined format compatible with the VMEC input file format.
- **coilsDB** Interface to the coil geometry database at W7-X.
- **vmeParams** Node to assemble all input parameters needed to perform a VMEC calculation.
- **vmeC** MHD equilibrium solver.
- **iotaEdge** Extracts the value of iota at the radial index given by **lcfsIndex**.
- **fluxops** Assortment of computational methods useful for computing physical quantities from the VMEC output files.
- **vmeFields** Three-dimensional Biot-Savart calculations involving the current density from a VMEC calculation.
- **magneticsDS** Datasource for the magnetic diagnostics.
- **fluxloop\_pred\_minerva** Fluxloop prediction node used to compute predictions for the diamagnetic and compensation loops.
- **rogowskisMinerva** Rogowski coil prediction node used to compute predictions for the Rogowski coils.
- **saddle\_pred\_minerva** Fluxloop prediction node used to compute predictions for the saddle coils.